Battery Pack Thermal Behaviour Modelling for General Aviation Electric Aircraft

A Case Study

Tristan Sidney Bakker

TU Delft

Battery Pack Thermal Behaviour Modelling for General Aviation Electric Aircraft

A Case Study

by

Tristan Sidney Bakker

to obtain the degree of Master of Science
at the Delft University of Technology,
to be defended publicly on Thursday June 20, 2024 at 11:00

Student number: 4801482
Project duration: 1 November, 2023 – 20 June, 2024
Thesis commitee : Dr. F Oliviero – Superivisor
Drs. W. Lammen – Company Supervisor (NLR)
Prof. L.L.M. Veldhuis – Chair
Dr. A. Bombelli – Examiner

An electronic version of this thesis is available at http://repository.tudelft.nl/.
Cover image retrieved from https://www.nlr.nl/aandachtsgebieden/strategische-themas-2022-2025/thema-duurzame-luchtvaart/pipistrel/

TU Delft

Abstract

To reduce greenhouse gas emissions in aviation, innovative propulsion systems such as battery-powered electric aviation are essential. These systems are carbon neutral when powered by 100% green electricity. However, widespread adoption requires overcoming challenges including improving energy density, lowering costs, and maintaining safe thermal operation (incl. thermal stability). This thesis addresses the challenge of maintaining battery thermal stability during flight by developing a combined electronic circuit and thermal network model for the NLR-owned Pipistrel Velis Electro aircraft. Using flight test data from this aircraft as a validation source, the model evaluates three battery thermal management strategies: two liquid cooling methods (ribbon and cold plate) and one gas cooling method (air cooling).

The electronic equivalent circuit model, used to simulate voltage characteristics and heat production in a single lithium ion battery cell, requires pulse current characterization tests for accurate parameter estimation. Extensive testing has been conducted to gather these data. The model achieves accurate voltage modeling accuracy with a low root mean square error Adding more than one RC branch to the circuit did not significantly improve the accuracy of the model.

The electronic equivalent circuit and lumped parameter thermal network models were validated with two flight data sets. Both ribbon and cold plate cooling solutions effectively matched the validation temperatures, performing similarly. In contrast, the air cooling solution was less effective. In case of ribbon cooling, the maximum cell temperature was highly sensitive to its geometric parameters, specifically the angle and height of the ribbon. The sensitivity of the cold plate solution in terms of maximum battery temperature was influenced by the diameter of the cooling channel and the thickness of the plate. The air cooling showed sensitivity in terms of maximum battery temperature relative to the inter-cell gap width. For the ribbon model, varying the number of thermal nodes led to a convergence in the maximum battery temperature as the node count increased.

Using the validated ribbon cooling model, two operational scenarios were analyzed. The first scenario involved charging operations, where simulations closely matched temperature validation data, showing only a minor temperature rise in the battery pack. The second scenario tested cold weather operations with ambient temperatures reduced to approximately 0 $^{\circ}C$. Here, two simulations were conducted: one with the battery preheated to 20 $^{\circ}C$ and another without preheating. Without preheating, the battery pack's temperature neared the operational lower limit of 0 $^{\circ}C$. Preheating prevented reaching this lower limit. It is recommended to preheat the battery pack using an external charger, as using the battery's own energy for preheating is inefficient.

The thesis was concluded by using the developed modeling approach to size and model a battery pack for the Eviation Alice, a larger aircraft. The approach was successfully scaled to this large use case with a known power profile. Furthermore, due to significant ambient temperature effects and higher operational altitudes compared to the Pipistrel Velis Electro, thermal insulation will be necessary for the battery pack to maintain temperatures above the lower operational limit of 0 $^{\circ}C$ during typical missions.

Acknowledgements

With the submission of this master thesis my academic career at Delft University of Technology comes to an end. Throughout the past six years, I have had the opportunity to meet inspiring colleagues working on challenging projects, participate in internships, and, in the end, conduct this master thesis. These experiences and opportunities have shaped and transformed me into the person I am today. That is something for which I am extremely grateful.
I have worked on this master thesis for the last 9 months. Overall, it has been a very educational experience and I have enjoyed it a lot. However, it was not always easy and obstacles and challenges did arise. Nevertheless, with a great amount of perseverance and support from my two supervisors, I am now able to present my master thesis called "Batterypack Thermal Modeling for Electric Aircraft". First of all, I would like to express my sincere gratitude to Drs. W. Lammen. Your support and extensive knowledge on physical modeling have proven to be invaluable in performing this research. Second, I would like to thank Dr. F. Oliviero for his unwavering support, guidance, and expertise. The involvement of both Drs. W. Lammen and Dr. F. Oliviero have been essential in completing my master thesis, but have also greatly contributed to my knowledge on physical modeling of batteries and developed my professional skills. It was a pleasure working with you.
A special and sincere thanks goes out to my family, (study-)friends and lost but not least my girlfriend. Your unconditional lover, support, and understanding have helped me complete this master thesis even in the face of hardship. In addition, I would like to thank my colleagues at the NLR, who made my time at the NLR really enjoyable.
To conclude, I feel disappointed that my time as a student is over, but in the meantime I am looking forward to what the future will bring me. Undoubtedly, the experience and knowledge that I have gathered during this journey will contribute to my future endeavors.

T.S. Bakker
Amsterdam, June 2024

Contents

List of Figures

List of Tables

Nomenclature

Acronyms

BEP	Battery Electric Powered
BIT	Break-In Test
BMS	Battery Management System
BTMS	Battery Thermal Management System
CDCT	Continuous Disharge/Charge Current Test
DoD	Depth of Discharge
EASA	European union Aviation Safety Agency
ECT	Entropic Coefficient Test
EECM	Electronic Equivalent Circuit Model
EV	Electric Vehicle
eVTOL	electric Vertical Take-off and Landing
GED	Gravimetric Energy Density
GIC	Graphite Intercalation Compound
HEP	Hybrid Electric Powered
HPPC	Hybrid Pulse Power Characterization
HSE	Hybrid Solid-State Electrolyte
LAP	Layered Approach Procedure
LE	Liquid Electrolyte
LFP	Lithium Iron Phosphate
LIB	Lithium-Ion Battery
LiPo	Lithium Polymer
LMO	Lithium Manganese Oxide
LPTN	Lumped Parameter Thermal Network
NCA	Lithium Nickel Cobalt Aluminum Oxide
NMC	Lithium Nickel Manganese Cobalt Oxide
OCV	Open Circuit Voltage
PCCT	Pulsed Current Characterization Test
PCDT	Pulsed Current Discharge Test
RC	Resistor Capacitor

RMSE	Root Mean Square Error
SE	Solid Electrolyte
SEI	Solid Electrolyte Interface
SG	Specific Gravity
SIE	Solid Inorganic Electrolyte
SoC	State of Charge
SoH	State of Health
SPE	Solid Polymer Electrolyte
SSE	Solid State Electrolyte
UAM	Urban Air Mobility
UAS	Unmanned Aircraft System
UAV	Unmanned Aerial Vehicles
UDDS	Urban Dynamometer Driving Schedule
VED	Volumetric Energy Density

Greek Symbols

ϵ	Dielectric constant	-
μ	Curve fitting constant	-
σ	Boltzman consant	$\frac{J}{sm^2K^4}$

Roman Symbols

ΔS	Change of entropy	J
$\dot{Q}$	Heat production	$\frac{J}{s}$
A	Exponential zone amplitude	V
B	Exponential time constant	$\frac{1}{Ah}$
F	Faradays constant	–
Gr	Grasshof number	–
h	Convective heat transfer coefficient	$\frac{W}{m^2k}$
I	Current	A
K	Polarization constant	$\frac{V}{Ah}$
k	Conductivity	$\frac{W}{mk}$
k	Thermal conductivity	W/(mK)
Nu	Nusselt number	–
Pr	Prandtl number	–
Q	Battery capacity	Ah
R	Internal resistance	Ω

Re	Reynolds number	–
T	Temperature	K
V	Voltage	V

Superscripts

E^0	Standard electrode potential	V

Subscripts

ΔH_i	Variation in enthalpy	J
C_0	Battery capacity begin of life	Ah
C_a	Battery capacity current cycle	Ah
C_p	Specific Heat	J/(kgK)
C_p	Specific heat capacity	$\frac{\text{J}}{\text{kgK}}$
E_o	Battery's constant voltage	V
V_{OC}	Open Circuit Voltage	V

1 Introduction

Powered flight has been possible since 1903, and in the following century, aero-space innovations and development have occurred at a rapid pace. Aviation has become an integral part of our society and a fast way of transporting human and goods. However, in all these years, one thing has remained the same: the use of fossil fuels for propulsion. Although engines today are highly efficient, aircraft emissions have increased due to an overall increase in the volume of flights [23].

For a long time, battery-powered electric flight was not considered as a realistic alternative to kerosine-powered jet engines and was placed in the realm of science fiction. With the low gravimetric energy density of batteries, electric aircraft required extremely heavy battery packs to even begin having a viable mission range. However, due to the emergence of electric cars and the need to be able to store excess green electricity produced by solar and wind, the development of lithium ion batteries has been put in a higher gear ([85], [8]). Since 2010 the gravimetric energy density of lithium ion battery cells has more than doubled from 120 Wh / kg to 300 Wh / kg [41], and in 2023 CATL even announced a 500 Wh / kg battery cell specifically designed for use in aviation [10]. With this increase in energy density, electric propulsion systems have garnered considerable attention, particularly within the realm of general aviation. Electric propulsion systems have the potential to revolutionize traditional aircraft design and operation. Central to the successful implementation of electric propulsion is the development of efficient and reliable battery systems capable of powering these aircraft.

Among the myriad challenges facing electric aircraft, thermal management of battery packs is a critical area of concern. The thermal performance of battery packs not only affects their longevity and reliability, but also influences the overall safety and efficiency of the aircraft ([48], [83]). As such, accurate modeling and simulation techniques are indispensable tools for understanding and optimizing the thermal behavior of battery packs in the context of electric aviation.

This master thesis addresses the need for a better understanding of battery thermal behavior in the context of electric aircraft. A general aviation aircraft will be applied as a case study and for model validation. The study will investigate the intricacies of the thermal behavior of lithium ion battery packs.

This approach followed in this thesis involves developing a combined electronic equivalent circuit and a lumped parameter thermal network model to evaluate the performance and thermal behavior of a lithium ion battery pack during a typical mission of a general aviation electric aircraft considering different battery thermal management systems. First, an investigation will be conducted on the applicability of electronic equivalent circuit models to model the performance and thermal losses of lithium ion battery cells. This was followed by an extensive experimental campaign to obtain the necessary data to properly configure the electronic equivalent circuit model. With the configured electronic equivalent circuit model, the heat load of individual battery cells could be calculated. With this heat production in individual battery cells, a lumped parameter thermal network models can be constructed and evaluated. These lumped-parameter thermal network models are constructed for three different types of battery thermal management systems; ribbon cooling, cold plate cooling, and air cooling. The developed models are then validated using experimental battery cell data and flight data from the NLRs Pipistrel Velis Electro aircraft. The thesis concluded with an investigation of how the developed model could be scaled to model the battery pack in a larger aircraft, e.g. in the form of the Eviation Alice[76].

This thesis report is divided into the following chapters. First, some background information on lithium-ion batteries and the Pipistrel Velis Electro aircraft is provided in chapter 2. Second, the research proposal de-

rived during the literature study [3] is presented in chapter 3. The modeling approach on how the electronic equivalent circuit and the thermal network model with lumped parameters are combined and used to model the thermal behavior of the battery pack is presented in chapter 4. chapter 5 will describe the experimental campaign and methodology used to obtain the experimental data required to configure the electronic equivalent circuit model together with the proposed verification and validation method using the test flight data. chapter 6 will show the results obtained when using the combined thermal electrical model and provide a discussion on these results. Finally, the thesis will be concluded with a number of conclusions and recommendations for future work in chapter 7 and chapter 8, respectively.

2

Background Information

As stated in chapter 1 lithium ion batteries (LIB) are considered a promising solution to enable electric propulsion and thus decarbonize aviation. Understanding the fundamental principles underlying lithium-ion batteries is essential to grasp their significance in aviation. From electrochemical reactions that occur with battery cells to the arrangement of battery cells to combine into battery packs, a nuanced understanding of battery operation is imperative to optimize performance, improve safety, and extend service life. This chapter will explain the scientific principles that govern lithium-ion battery operation, elucidating key concepts such as charge/discharge mechanisms, cell chemistry, and battery components. This information will be contained in section 2.1. This will be followed by a summary of different model types to model the performance and thermal losses of lithium-ion battery cells in section 2.2. In addition to information on the scientific principles of LIBs, a development roadmap for possible future developments of LIB technology and a description of the aircraft considered as the use case in this thesis will be provided. This information will be presented in subsection 2.1.4 and section 2.3.

2.1. Lithium-Ion Batteries

Lithium ion batteries have been identified as a possible future energy source for future zero-emission aircrafts due to their high energy density [42] and decreasing production costs. This section aims to provide the necessary background information on the workings of lithium ion batteries to comprehend the remainder of this report. First, a number of definitions and concepts will be provided wich are needed to describe lithium ion batteries. This will be provided in subsection 2.1.1. A short overview of the electrochemical working principles of LIBs (subsection 2.1.2) is provided, followed by a discussion of the various components of LIBs (subsection 2.1.3) and a roadmap for future possible developments in LIB technology (subsection 2.1.4).

2.1.1. Definitions

In this report, a number of concepts and definitions are used to quantify battery performance or indicate the state of the battery. In this subsection, an overview of these definitions will be provided so that they are used consistently in the report.

Voltage: The electric potential difference between the positive and negative terminals of a battery, usually expressed in volts (V).

Current: The rate at which electric charge is drawn from the battery, usually expressed in amps (A). In this report, the current is considered positive going into the battery (charge) and negative going out of the battery (discharge).

Capacity (Q): The amount of electrical charge that can be stored inside the battery and delivered electric current, usually expressed in Ah.

State of Charge (SoC): The amount of charge stored relative to the total charge storage capacity of the battery; see Equation 2.1.

$$SoC = \frac{Q}{Q_{tot}} \tag{2.1}$$

Depth of Discharge (DoD): The amount of charge discharged from the battery relative to the total capacity, that is, the opposite of SoC; see Equation 2.2.

$$DoD = 1 - SoC \tag{2.2}$$

State of Health (SoH): The ratio of the maximum battery charge to its rated capacity; see Equation 2.3

$$SoH = \frac{Q_{max}}{Q_r} \tag{2.3}$$

C-rate (C): The amount of current drawn from the battery relative to the total battery capacity in Ah; see Equation 2.4.

$$C = \frac{I}{Q_{tot}} \tag{2.4}$$

Specific Energy (SE): The amount of energy that can be stored in a battery for every kilogram of battery mass, usually expressed in Wh/kg.
Energy Density (ED): The amount of energy that can be stored in a battery per cubic meter, usually expressed in Wh/m3.
Cycle life: The amount of charge / discharge cycles that a battery can experience before reaching a predetermined capacity or other performance criteria.
Open Circuit Voltage (OCV): The output voltage of the battery cell without an external load connecting the two terminals.

2.1.2. Electrochemical

There are many different types of lithium ion batteries, but the main working principle for all types of batteries is the same. During discharge, a lithium atom detaches from the negative electrode (anode) and splits into a lithium ion and an electron. The lithium ion will flow through the electrolyte and integrate into the positive electrode (cathode). In the electrolyte, there is a separator material that prevents the electron from flowing through the electrolyte. Instead, the electron has to travel out of the battery cell and onto a wire or electrical device. When the battery is being charged, this process occurs in reverse. A schematic of the working electrochemical principle of a LIB can be found in Figure 2.1. The process can also be described using half-cell reactions. The reaction occurring at the anode is represented in Equation 2.5, and the reaction occurring at the cathode is represented in Equation 2.6. The two half-cell reactions can be summed to create the full-cell electrochemical reaction, as seen in Equation 2.7[13]. Note that the half-cell reaction provided is for a LIB with $LiCoO_2$ cathode chemistry and a liquid electrolyte. This will be explained in more detail in subsection 2.1.3.

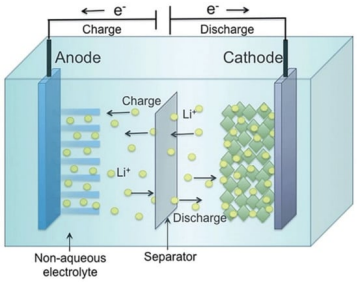

Figure 2.1: A schematic of the workings of a Lithium-Ion battery cell adapted from [28]

$$LiC_6 \underset{\text{Charge}}{\overset{\text{Discharge}}{\rightleftharpoons}} C_6 + Li_+ + e^- \tag{2.5}$$

$$CoO_2 + Li^+ + e^- \underset{\text{Charge}}{\overset{\text{Discharge}}{\rightleftharpoons}} LiCoO_2 \tag{2.6}$$

$$CoO_2 + LiC_6 \underset{\text{Charge}}{\overset{\text{Discharge}}{\rightleftharpoons}} LiCoO_2 + C_6 \tag{2.7}$$

2.1.3. Components

subsection 2.1.2 explained the electrochemical working principle of lithium ion batteries. From this explanation, a number of battery components could be identified. These components are the cathode, the anode, the electrolyte, and the separator. This subsection will elaborate on the function of these components and elaborate on the different options available for each component.

Electrolyte

In a LIB the electrolyte allows for the movement of lithium ions between the anode and the cathode. Therefore, it is important that the electrolyte has chemical properties that allow for good ion transport, such as high ionic conductivity, high dielectric constant, large electrochemical stability window, and thermal stability. In addition to properties that are good for ion transportation, the electrolyte also has to have good mechanical properties and be inert to the other components inside the battery cell. Currently, there are two main options for the electrolyte of a LIB.

The first option is a liquid electrolyte (LE). An LE is an electrolytic solution in the liquid phase comprising at least one salt dissolved in at least one nonaqueous liquid polar solvent [34]. Within the category of LEs, different types of LEs exist, such as organic and inorganic electrolytes. For a detailed explanation of the difference between these electrolyte categories, please refer to [3]. Most LIBs currently commercially available use a LE because of its lower cost and ease of manufacturing compared to the next electrolyte option, the solid electrolyte (SE). However, compared to SEs, LEs have a number of downsides, such as high flammability, insufficient thermal stability, possible electrolyte leakage in the event of enclosure rupture, and an overall lower energy density [64].

The second option is a solid electrolyte (SE). A SE is an electrolyte that is in the solid phase. This type of electrolyte attempts to address several of the downsides of LE. SEs have better thermal stability, are generally not flammable, and overall have improved safety compared to LE all while having high ionic conductivity, high moduli, and high electrochemical and thermal stability [90]. SEs also have the potential to make use of high-capacity Li metal anodes, which can greatly improve energy and power density along with the cycle life of current batteries [30]. More details on Li metal anodes can be found in subsubsection 2.1.3.3 and in [3]. However, SEs do have a number of practical issues that have currently kept them from widespread commercial adoption. SEs suffer from manufacturing difficulties (such as fragility in larger areas), poor interfacial charge transport coming from inferior contact with the electrodes compared to LE, the risk of metal dendrite growth, high cost, and poor environmental stability [90].

Cathode

The function of the cathode in a lithium-ion battery cell is to allow the integration of the lithium ion during discharge and the deintegration during charge. The main difference between various types of cathode is the material of which the cathode is made. Currently, there are four main cathode chemistry types: lithium iron phospate (LFP), lithium manganese oxide (LMO), lithium nickel cobalt aluminum oxide (NCA), and lithium nickel manganese cobalt oxide (NMC). Using a different cathode chemistry can give the lithium-ion cell very different properties. The differences will be explained shortly for each type of cathode cell chemistry. For a more detailed explanation, see [3].

LFP batteries use $LiFePO_4$ as cathode materials. LFP batteries have very good thermal stability compared to the other chemistries. LFP batteries are the only battery capable of passing a nail penetration test, a crush test, and a short circuit without thermal runaway [54]. Thermal runaway occurs when a self-sustaining reaction within the battery generates excessive heat, leading to a rapid increase in temperature. This can cause the battery to ignite or explode due to the release of gases and the breakdown of internal components. Another upside of this cathode chemistry is that it does not use any rare-earth metals such as cobalt, which is both expensive and mined under questionable humanitarian conditions. The main downside of LFP battery chemistry is that the gravimetric energy density (GED) of these types of battery cells is very low, around 150 Wh/kg [79]. This level of energy density makes this cell chemistry not suitable for use in aviation applications [15],

LMO batteries have a cathode material made of $LiMn_2O_4$. The main benefit of the LMO cathode chemistry is that it does not use cobalt, it is quick to charge, and it is power dense. Chemistry also has several downsides, such as the dissolution of manganese in the electrolyte leading to a loss of capacity [54]. In addition, the GED of the chemistry is between 100-150 Wh / kg [7], which makes them not suitable for use in aviation.

NCA batteries have a cathode material made up of a mixture of nickel, cobalt, and aluminum. The main benefit of the chemistry of the NCA battery is the very high GED of 250-300 Wh/kg [25]. This high GED makes

this type of chemistry very attractive for use in aviation; however, it comes with a number of serious safety concerns. NCA batteries are thermally unsafe when not properly managed. In the NCA battery, the cathode undergoes an exothermic reaction with a very high enthalpy (941 J / g) between 200 and 250 degrees Celsius [54]. This can trigger thermal runaway, which in turn could decompose the electrolyte into a gas, which can build up pressure and possibly rupture the cell casing. A ruptured cell will almost always result in a battery fire and in a worst-case scenario an explosion. Due to the thermal instability and propensity of battery fire, the NCA cathode has not been identified as a possible future battery cell to be used for in electric aviation [15].
NMC batteries have a cathode material made up of a mixture of nickel, manganese, and cobalt. NMC chemistry is an iteration of NCA chemistry and attempts to address its main issue of thermal instability. This is done by adding magnanese to the crystal lattice, providing thermal stability during charging and discharging [54]. When manganese is introduced, the GED can remain the same or even higher than that of NCA, but the chemistry is much safer to use. Currently, there is a trend that will increase the amount of active nickel in the material mix to achieve a GED even higher than before. A more detailed explanation of how this is done can be found in [3]. Due to its high GED and improved thermal stability, the NMC chemistry has been identified in [42] as the most promising cathode chemistry for use in aviation.

Anode

The function of the anode is to release a lithium-ion during discharge and collect one during charge. This is called the intercalation and deintercalation of lithium ions. Currently, most of the anodes used in LIBs are made of graphite with a market share of 95% [19]. Graphite anodes have been very popular due to their low cost, abundance, high power density, and long life cycle [90]. Currently, the energy density is attempted to be improved with the introduction of silicon into the anode.
Silicon has the benefit that one silicon atom is able to capture 4 lithium-ions whereas a carbon atom (graphite) needs 6 atoms to fully capture 1 lithium-ion. Furthermore, silicon is very abundant and affordable ([61], [1]). The introduction of silicon into anodes is typically done by introducing a small amount of silicon into graphite anodes (8 wt%). Eventually the goal is to have anodes made with a very high silicon content; however, silicon has the issue of very large volume expansions. Volume fluctuations of a fully intercalated and deintercalated silicon anode can exceed 300% [61]. The high-volume fluctuations in anodes made from silicon materials introduce problems such as irregular and unsteady electrical contact (delamination), particle cracking, and ineffective electron transfer. All of these problems reduce the actual capacity of Si anodes from the high theoretical value to a much lower value achieved in commercial applications of the technology.
A third anode option is to use a lithium-metal anode. This is an anode made of pure lithium. This type of anode can have a very high theoretical capacity and a very low electrochemical potential [73]. However, these types of anodes still face a number of challenges, such as the formation of lithium dendrites onto the anode, which can cause short circuiting of the battery, leading to battery fire. A more detailed explanation of how dendrite growth can cause battery fires is provided in [3].

2.1.4. Development Roadmap

subsection 2.1.3 described several battery components and possible options for these components. Some of these options and possible developments will be suitable for use in aviation, and others not. Kühnelt et al. identified which development options are suitable and order these technology development options on their technology readiness level (TLR).
Using the method of Kühnelt et al., a prediction of possible generations of batteries was created with the required battery technology in mind. An overview of these battery generations can be found in Table 2.1. The division between generations is based on four major development steps.

1. Utilize better existing active materials (NMC, graphite).
2. Increase the energy density of the anode.
3. The development of higher-performance and more stable electrolytes includes a variety of approaches.
4. Increase the energy density of the cathode by progressing to Li-rich active materials.

A schematic of this development road map can be seen in Figure 2.2. In [42] a minimal GED threshold of 500 Wh / kg was identified to allow long-term electric flight. However, this threshold was identified for short-range passenger airplanes. As stated chapter 1, the use case for which the model will be developed is a small

general aviation aircraft in the form of Pipistrel Velis Electro. A more detailed description of this aircraft will be provided in section 2.3. The energy requirements for general aviation aircrafts are much lower than those of short-range passenger aircrafts, and therefore this threshold of 500 Wh/kg does not apply to these types of aircraft. Since the investigated use case is the Velis Electro, only batteries of the first and second generation, with a graphite anode and liquid electrolyte, will be applicable.

Table 2.1: Different battery generations and their possible air transport applications

GEN	[Cathode | Electrolyte | Anode]	CGED [Wh/kg]	TLR	Air Transport Applications (EiS 2035)
1	LFP or NCA | LE | C	160	9	—
2a	NMC111 | LE | C	230-250	9	—
2b	NMC523-NMC622 | LE | C (SotA)	230-250	9	—
3a	NMC622 to NMC811 | LE | C+Si (5-10 wt%)	350-400	8-9	minor applications
3b	HE-NMC, LNMO | LE | Si/C	350-400	5-6	small aircraft propulsion
4a	HE-NMC | SE | hihg Si/C, Si	400-500+	2-3	hybrid propulsion
4b	All-solid-state electrolyte | Li-M	400-500+	2-3	hybrid/all-electric propulsion
5	Li-O2, Li-S solid	500+	1-2	long term electric flight

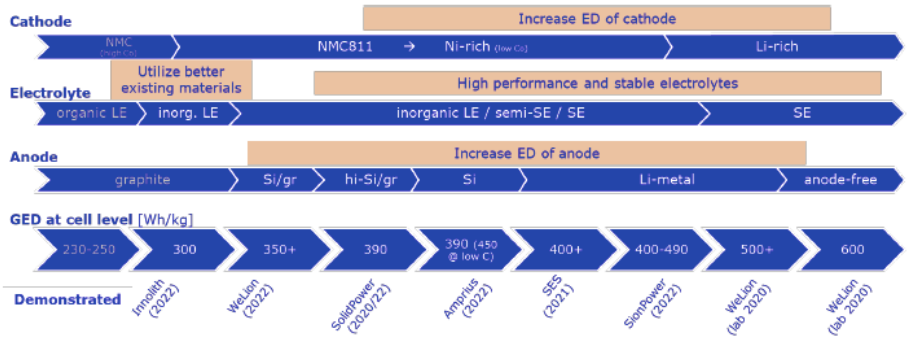

Figure 2.2: A schematic of the possible development steps between different generations of cells[42]

2.2. Lithium-ion Battery Cell Models

This section will elaborate and explain the four main types of LIB cell models. In general, the performance of LIB cells in terms of SoC, current, and voltage can be modeled with four different types of model. These models are physical models, data driven models, empirical models and equivalent circuit or electrical-basedd models. Each of these models has their own approach to modeling the battery cell, along with pros and cons of that method. Each type of model and the pros and cons of that model will be discussed in subsection 2.2.1, subsection 2.2.2, subsection 2.2.3 and subsection 2.2.4, respectively.

2.2.1. Physical Model

Physical models are models that try to represent a battery on its true physical basis. This could be, for example, modeling the internal battery chemistry and its electrochemical features. This type of model is very complex and requires many input parameters and detailed knowledge of the chemical composition, layout, and components of the battery. This makes these types of model very computationally expensive and rather slow. However, these models do achieve very high accuracy levels, making these types of models a perfect candidate for use in battery-cell development laboratories. An example of such a model is the lithium polymer insertion cell model [17], Single Particle Models (SPMs) and Psuedo 2-D Models (P2-D). The lithium polymer insertion cell model is very accurate, but requires knowledge of more than 50 parameters to be configured and has very high computational complexity [65]. In Figure 2.3 a linear trend between the increasing computational power with the model's accuracy can be observed, showing that the physical models are much more accurate but much more expensive to use than the empirical models. For this reason, the model is again very well suited for battery cell design in a laboratory but not for applications such as battery management systems or to be used as a subsystem design tool in a multidisciplinary aerospace design procedure. In such a procedure, many iterations are made upon the design which cause changes in the subsystems. Being able to quickly iterate on these subsystems means that the models that model these subsystems need to be reasonably accurate but mostly quick at modeling. For the use case considered in this thesis, such detailed information on so many cell parameters is unavailable. For this reason, these physical model types are not suited for use in this thesis.

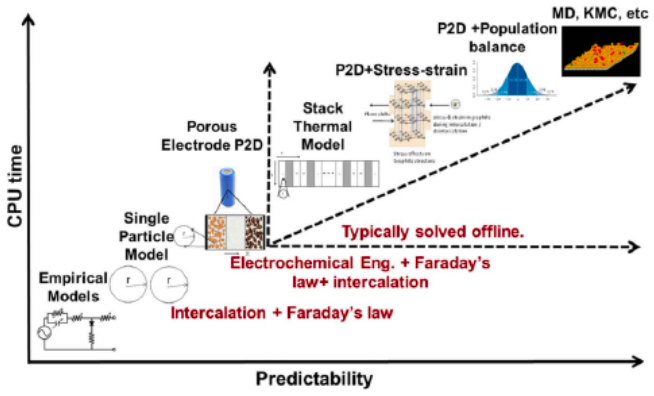

Figure 2.3: Physical battery models-computational power vs. model's accuracy [60]

2.2.2. Data Driven Model

Data driven models are a new type of battery model that has emerged recently. A data driven model is considered a black box model since there is no direct physical link between the model parameters and its outputs. These black-box models model the behavior of battery behavior using some intelligent modeling methods without the need to understand the underlying electrochemical that occurs in the battery [87]. An example of such a model is the model proposed in [37]. This model used a RBF-kernel based SVM method. The model could be used to simulate battery dynamics as assisted by a small amount of experimental data. Another example of a data-driven model is the model proposed in [11]. In this model, battery capacity was modeled using an artificial neural network. In general, the performance of these types of models depends largely on the training data and training procedure. To achieve a suitable accuracy,usually a large number of parameters and a good set of training data is required. The need for this a very large set of training data sets makes

this type of model not well suited for use during the (preliminary) design phase of an aircraft. This is simply due to the fact that at this point in the design procedure very extensive experimental data are usually not yet available and only general data such as typical cell discharge curves are available. This type of experimental data is not enough to properly train the model to a sufficient accuracy level.

2.2.3. Empirical Model

In comparison to physical models, empirical models are rather simple and do not require a lot of computer power. In empirical models, typically, the discharge curves are taken and modeled through various mathematical functions. Empirical models use polynomial, exponential, power-law, logarithmic, and trigonometric function fits with past experimental data to predict the future behavior of Li-ion batteries. However, these models use parameters that lack physical meaning. Although these models are very easy to develop from a mathematical point of view, they are not accurate outside the limited set of conditions from which they were developed [43]. In the literature a different name used for empirical models can be mathematical or analytical models. Three of the most well-known empirical models are the Unnewher, Nernst, and General Shepherds models. A detailed description of these three empirical models is provided in [3]

2.2.4. Electronic Equivalent circuit Model

Electrical equivalent circuit models (EECM) use various electronic components such as resistors, voltage sources, and capacitors to model battery behavior. (An example circuit model can be seen in Figure 2.4 Similarly, as in the case of empirical models, EECMs do not have a deeper physical/chemical model. However, each circuit element in the can be linked to specific physical battery behavior phenomena. These types of models are able to accurately model the battery behavior, given that enough components are used in the circuit. The more components used, the more complex the model becomes. This creates a trade-off within these types of model between high fidelity and computational efficiency. In general, EECMs are capable of operating within reasonable computer power while obtaining an accuracy higher than that of empirical methods. A drawback of this type of model is that often access to the real battery is needed, since a series of tests is usually needed to obtain the internal model parameters.

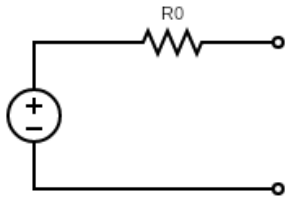

Figure 2.4: Schematic of 0-RC or R_0 EECM

The need for experimental data to obtain the model parameters is very similar to that seen with data-driven models. The amount of data required to configure an EECM however, is much less than that needed to train a full data driven model. This places the EECM model type in the middle between the empirical approach which needs almost no data and data-driven approach which needs a lot of data to be properly trained. The high accuracy of the EECM [33] and the relatively simple experimental procedure to obtain the experimental data required for this model ([40], [35]) make this type of model the most suitable to use in this thesis.

2.3. Pipistrel Velis Electro

The Pipistrel Velis Electro is the world's first fully certified battery powered electric aircraft [6]. The plane is powered by two lithium-ion battery packs, made up of 1152 18650 cylindrical lithium-ion cells, which give it a maximum endurance of 50 minutes. One of the batteries is mounted on the nose of the plane and the other is mounted on the aft side, as seen in Figure 2.6. The layout and technical specifications of the battery pack will be further elaborated on insubsection 2.3.1 while information on the battery cells used will be provided in subsection 2.3.2. The batteries have a dedicated thermal management system consisting of two coolant pumps and a radiator. A detailed overview of the thermal management system will be provided in subsection 2.3.3.

Figure 2.5: An image of the Pipistrel Velis Electro [56]

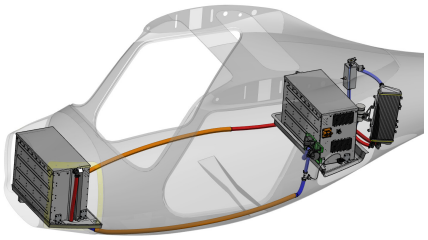

Figure 2.6: The battery placement in the Pipistrel Velis Electro [68]

2.3.1. Battery Pack

The Velis Electro has a high voltage electric power system. The primary energy sources are two Pipistrel PB345V124E-L battery packs. This ensures redundancy of the power source. In case of battery failure, the faulty battery is disconnected from the system. A single battery is capable of standalone operation and has enough power output capability to support climbing of the aircraft and continuation of flight (single battery operation is not considered normal procedure). Batteries can be charged via an onboard charging port. The electric charger is not part of the aircraft [68]. The performance parameters of the battery pack can be seen in Table 2.2.

Table 2.2: Battery Pack Parameters [68]

Parameter	Value
Cell Type	INR18650-33G
Minimum voltage	260 V
Nominal voltage	345 V
Maximum voltage	398 V
Maximum discharge current	120 A
Maximum cont. discharge power	40 kW
Maximum charging current	40 A
Operating temp. range (discharge)	0 deg C - 58 deg C
Operating temp. range (charge)	0 deg C - 45 deg C
Allowable temp. range for storage	0 deg C - 30 deg C
Rated capacity	33Ah, 11 kWh
Configuration	96S12P

The battery pack has a cell arrangement of 96 cells in series and 12 in parallel. This gives each battery pack a total of 1152 cells. Since the internal layout of the battery pack is proprietary information and thus not publicly available, and there was no possibility of opening a battery pack during this thesis, a number of assumptions needed to be made about the internal layout of the battery pack. Assumptions must be made on the internal battery cell layout and the internal thermal management system. Support for the assumption on the internal cell layout will be provided in this section, and the assumption on the internal thermal management system will be provided in subsection 2.3.3.
When considering the geometric dimensions of the aluminum package enclosure of 0.26x0.54x0.38 m (LxWxH) and the 3 grooves on the sides of the battery enclosure, the conclusion can be drawn that the battery pack will

have 4 layers stacked vertically on top of each other. This means that each layer will have 1152 / 4 = 288 cells per layer. These 288 cells can be arranged either with a square arrangement, where the centers of each cell are on a straight line, or with a hexagonal arrangement, where there is an offset between the cell centers to better utilize the available space. The assumption is made that the packaging of the battery cells was done as compactly as possible and that a hexagonal arrangement is assumed. Taking into account the arrangement of 96s12p, it would be logical to have 12 cells on one side of the battery. 12 cylindrical cells of type INR18650-33G end-to-end would have a total length of 21.6 cm. When these cells are placed on the length side (0.26 m) of the battery pack, they still have a margin of 2.2 cm on each side. This is considered a suitable margin. When the length side has 12 cells, the width side (0.54 m) must have 24 cells to meet the total cell count of 288 cells per layer. The total length of the width side cell would be 43.2 cm leaving a margin of around 10 cm at the edges for electrical wires, data connectors, or coolant ducts. The final cell arrangement now be 12x24x4 (LxWxH). A visualization of a 12x24 vertical layer is provided in Figure 2.7.

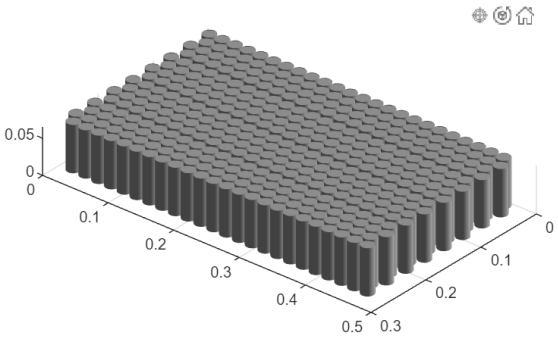

Figure 2.7: A visualisation of the 12x24 battery module

2.3.2. Battery Cell

As stated in Table 2.2 the lithium-ion battery cell used in the battery pack is the INR18650-33G cell manufactured by Samsung [68]. This battery cell is a cylindrical 18650 cell. The 18650 form factor means that the cell has a diameter of 18 mm and a height of 65 mm. The cell uses NMC cathode chemistry to achieve a higher energy capacity. An image of the battery cell can be seen in Figure 2.8 and the cell specifications can be seen in Table 2.3.

Figure 2.8: An image of the Samsung INR18650-33G cell [44]

Parameter	Value
Typical capacity	3150 mAh
Minimum capacity	3000 mAh
Charging voltage	4.2 V
Nominal voltage	3.60 V
Charging current	975 mA
Max. charge current	3250 mA
Max. discharge current	6500 mAh (con. discharge) 9750 mAh (non con. discharge)
Discharge cut-off voltage	2.5 V
Cell weight	48 g
Cell dimensions	Height: 65.2 mm Diameter: 18.4 mm
Operating Temperature	Charge: 0 to 45 °C Discharge: -20 to 60 °C

Table 2.3: Specifications of the Samsung INR18650-33G Cell [47]

2.3.3. Battery Thermal Management System

In order for lithium ion battery cells to operate safely, they must be kept in a strict temperature window of 0 to 45 $°C$ for charge and 0 to 58 $°C$ for discharge [68]. Ideally, this temperature window is kept between 10 and 35°C for maximum performance. The drop below the 0 °C threshold will cause the internal resistance of the battery to increase, decreasing the available energy and open circuit voltage. Increasing above the temperature threshold of 45 °could cause the battery cell to experience a thermal runaway in which the battery cell temperature increases in an uncontrollable way due to the increase in heat production within the cell. The purpose of the battery thermal management system (BTMS) is to keep the battery cell temperature within this temperature window and to minimize the temperature difference between the battery cells given different operating conditions.
In Figure 2.9 the configuration of the external BTMS for Pipistrel Velis Electro can be seen. External means how the heat is transported externally from the battery out of the aircraft. In Figure 2.9 it can be seen that there is one heat exchanger connected to two serially connected coolant pumps. The coolant pumps are two 12 Volt pumps manufactured by Bosch [63]. This coolant pump has a maximum volumetric flow rate of 1100 l/h [9]. After the coolant pumps, the coolant splits into two flows, one for each battery after the pump, and combines again at the heat exchanger. This system is shown schematically in Figure 2.10.

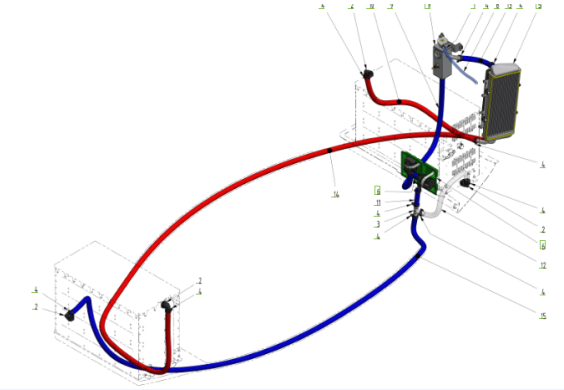

Figure 2.9: The external BTMS of the Pipistrel Velis Electro [68]

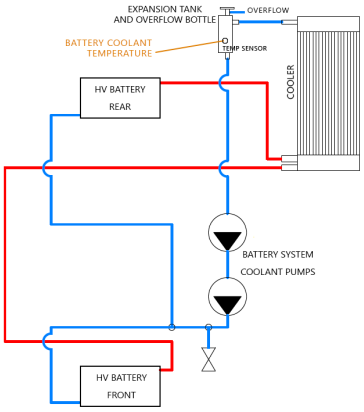

Figure 2.10: A schematic of the BTMS of the Pipistrel Velis Electro [68]

As with the internal battery cell configuration, there is no information available on what is inside the battery pack. For this reason, assumptions must be made about the layout of the internal BTMS. After internal discussions with NLR experts, the decision was made to investigate the two most common ways of liquid cooling a battery pack. These two options are ribbon and cold plate cooling. subsubsection 2.3.3.1 and subsubsection 2.3.3.2 will provide information on what these cooling methods look like and how they extract heat from the battery pack.

Ribbon cooling

Ribbon cooling is a form of liquid cooling in which the coolant is pumped around in a ribbon that is attached to the sides of the battery cells. This ribbon snakes around the sides of the cells through the entire battery pack to transport heat out of the battery pack. An example of a cooling ribbon can be seen in Figure 2.11. The benefit of using a cooling ribbon over the cold plate cooling option is that the ribbons have a much larger surface area in contact with the battery cell. This provides more area for heat flow and does not produce two low-temperature regions at the ends of the battery cell, as will be shown with the cold plate option.
Cooling ribbons do have a number of downsides compared to a cold plate. The first downside of using ribbon cooling is that heat needs to be conducted radially out of the core of the battery rather than axially. In general, the thermal conductivity of a lithium-ion battery cell in the radial direction is an order of magnitude lower than that in the axial direction[92]. Second, the cooling ribbons are harder to manufacture and integrate in the battery pack as they are'snaked' in between the cells and thus influence their arrangement. Third, the coolant will experience more resistance to flow as a result of the small bends in the ribbon, meaning that a larger pressure differential will be needed to achieve the same flow rate as with a straight channel. The larger pressure differential can only be achieved with the use of a more powerful pump that requires more electrical energy.

Figure 2.11: An Image of a cooling ribbon [1]

Cold plate cooling

Cold plate cooling is a form of liquid cooling in which battery cells are connected to a plate directly. The plate contains channels through which the coolant is pumped to transport the heat to the external heat exchanger. An example of a cold plate can be seen in Figure 2.12. The battery cell will be sandwiched between two of these plates, as seen in Figure 4.17. The main variation between different types of cold plates is the path that the cooling channels follow throughout the cold plate. The channels can be parallel to each other along the cold plate length, snake around the plate in a u-shape, or flow only at the edge of the plate. In this thesis work, only the parallel-channel cold plate configuration will be considered, since this configuration is the easiest to model. This is because the flow in the straight parallel channels is simple, since there is no need to account for any bends or curves in the cooling channels. This cold plate configuration is also the simplest to model geometrically, since the channels only go in one direction, making the discretization of the cold plate easier and hence making the integration into a lumped-parameter thermal network model simpler. How exactly this works will be explained in more detail in subsection 4.3.3.

Compared to ribbon cooling, a cold plate has the advantage of being very easy to integrate into the battery pack. No changes to cell configuration or intercell distances are required, so this cooling solution can be applied to nearly all battery packs. The cold plate also extracts heat from the batterycell in an axial direction. The thermal conductivity of a lithium ion battery cell in the axial direction is an order of magnitude greater than in the radial direction [91]. This could offset the downside of having a smaller contact area between the cell and the plate compared to the cooling of the ribbon, but investigation into this will be necessary. This investigation will be conducted in subsection 4.3.3. An additional downside of the cold plate compared to ribbon cooling is that the cold plate will create two regions of low temperature at the ends of the battery cell. This will create a temperature gradient along the axial direction of the cell. Since the lumped-parameter thermal network model will lump the battery cell together into one thermal mass of a single temperature, care must be taken to analyze if this temperature gradient is not so large that the lumped thermal mass assumption is no longer valid.

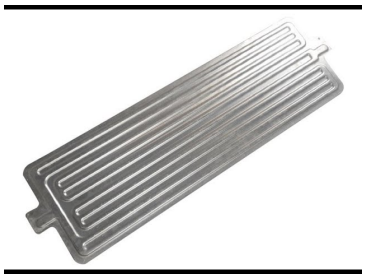

Figure 2.12: An example of a cold plate [2]

[1] https://i.ytimg.com/vi/LVRRG1YM_J0/sddefault.jpg
[2] https://encrypted-tbn0.gstatic.com/images?q=tbn:ANd9GcRsFjB7UsxaaJmyWPSGDGTg2b3AFF9mIo9MVg&usqp=CAU

3

Research Plan

As concluded in the literature study [3] a good BTMS is extremely important. However, a BTMS adds weight to the aircraft, since many components such as coolant pumps and heat exchangers will be required. These components add weight to the aircraft requiring a bigger battery, requiring a bigger BTMS etc. This can trigger a snowball effect. For this reason, it is very useful to have a model that can model the thermal behavior of a battery pack of an electric aircraft considering different thermal management systems. This model should consider the typical mission profile of the aircraft from which a required power profile and boundary conditions will follow. From this power profile, a suitable battery pack geometry should be sized, and from this pack geometry and the chosen thermal management strategy, the heat load of the battery pack should be determined during the various flight phases.

This thesis will address the challenge described in the paragraph above and fill in this research gap by developing a combined electronic equivalent circuit (EECM) and a lumped parameter thermal network (LPTN) model of a battery pack from an electric general aviation aircraft to investigate the thermal behavior of batteries during a typical mission. So far, empirical relations have been the main model used to model the thermal behavior of battery cells [43]. The use of more accurate electrical equivalent circuit models has been rather limited, although these models give more accurate results [33].

This thesis attempts to use the EECM to find the heat production of the battery cell and then proceeds to use an LPTN to model the thermal behavior of the complete battery pack considering different BTMS. So far, most research has focused on either the thermal behavior of a single battery cell or model-complete battery packs using LPNT but with rather simple electrical cell models. This thesis work tries to improve on this by making a link between the EECM and LPNT, and, therefore, having both a sophisticated electrical and thermal model.

The use of the described modeling approach also allows for the investigation of the effectiveness of various BTMS on battery thermal management by finding their influence on the LPNT. With the BTMS models, it is also possible to perform analysis on the sensitivity of a BTMS to its geometric parameters. The Pipistrel Velis Electro use case also presents a unique opportunity in which there are actual validation data available on both the electrical and thermal performance of the battery pack. From these statements, several research gaps have been identified, as seen in the following list.

- **The use of electric equivalent circuit models to model battery cell behaviour in a battery pack is relatively unexplored**
- **The usage of combined electronic equivalent circuit models and lumped parameter thermal models has been under investigated**
- **Proper sensitivity studies on the influence of the geometric parameters of different battery thermal management system has not been extensively conducted**
- **The availability of actual flight test data of the full battery pack system is uncommon.**

3.1. Research Objective

Main Research Objective

To develop a combined electronic equivalent circuit and a lumped parameter thermal network model to evaluate the performance and thermal behavior of a lithium ion battery pack during a typical mission of a general aviation electric aircraft considering different battery thermal management systems.

3.2. Research Questions

This section will provide an overview of the main research question, as well as related subquestions needed to obtain the main research objective. The main research question is divided into two parts (MQ-1 and MQ-2) and can be found below. Below the main research question, a number of subquestions are listed that support the answer to the main research question. These questions can be seen in subsection 3.2.1.

MQ-1 **What is the performance and thermal behavior of a lithium-ion battery pack during a typical mission of an electric general aviation aircraft?**

MQ-2 **How to access the thermal behaviour of a lithium-ion battery pack during a typical mission of an electric general aviation aircraft considering different thermal management strategies**

3.2.1. Sub-questions

SBQ-1 **How can a lumped parameter thermal network model be used to represent a battery pack?**

- SBQ-1.1 How can battery cells be used to make up the nodes in the thermal network?
- SBQ-1.2 How can the thermal capacity of each node be accurately determined?
- SBQ-1.3 How can the thermal resistances between each node be calculated?
- SBQ-1.4 How many nodes will be needed to accurately present the battery pack?

SBQ-2 **How can an electrical equivalent circuit model be used to model the behaviour of the battery cell?**

- SBQ-2.1 How can the parameters of the electrical equivalent circuit model be configured to represent a specific Li-ion battery cell?
- SBQ-2.2 What experimental data are needed to configure the model?
- SBQ-2.3 What is the influence of the number of resistor-capacitor pairs on the accuracy and complexity of the model?
- SBQ-2.4 How can the heat production inside a cell be modeled with this model?

SBQ-3 **How can lumped parameter thermal network models in combination with electronic equivalent circuit models be applied to assess various thermal management systems?**

- SBQ-3.1 What are the main influences of the thermal management system on the thermal network?
- SBQ-3.2 How can we estimate the size of the thermal management system and indicate the impact of the different thermal management strategies on the operational empty weight and the required air mass flow from the heat exchanger of the aircraft?
- SBQ-3.3 Is there a need for heating the battery pack during low-ambient-temperature operations and how does this influence battery performance?
- SBQ-3.4 How does the thermal behavior of the battery packs differ during charging, and how does this influence the battery thermal management system?

SBQ-4 **How sensitive is each thermal management system of to its own geometric parameters?**

SBQ-5 **How can the performance and accuracy of the developed lumped parameter thermal network model be analyzed and explained**

- SBQ-5.1 Which metrics and performance indicators can be used to evaluate the performance of the model?
- SBQ-5.2 What kind of experimental data is available on thermal behavior of a battery pack?
- SBQ-5.3 How well does the model convergence to a solution when its nodal resolution is increased?

4

Modelling Approach

The goal of this thesis is to develop a combined electronic equivalent circuit (EECM) and lumped parameter thermal network (LPTN) model for a lithium ion battery pack. As the goal suggests, two separate models will need to be developed and integrated to achieve this goal. The purpose of this chapter is to present the modeling approach used to achieve the research objective. First, an overview of how the EECM and LPTN models are interconnected will be provided in section 4.1. Afterwards, the EECM and LPTN modeling approach will be explained in more detail in section 4.2 section 4.3, respectively. The models were implemented in MATLAB using the Simscape toolbox SimBattery (oi.d.).

4.1. Model Overview

This section aims to provide an overview of the interconnectivity of the EECM and the LPNT model. The main goal of the EECM is to model the electrical performance of the battery pack. The main input of the EECM is the current drawn from the battery pack and the cell temperature. Throughout this thesis work, the current drawn from the battery pack will be referred to as the current profile and is considered positive going into the battery (charging). The main output of the EECM is the output voltage and the SoC of the battery pack. With the output voltage, SoC, and current, the heat load (Q) of the battery can be calculated, as will be described in more detail in section 4.2.

The calculated heat load serves as an input for the LPTN model. With this heat load, the LPTN can calculate the new temperature of the battery cell and feed this temperature back into the EECM as an input. The calculation procedure for the new cell temperature is highly dependent on the ambient temperature around (i.e. the temperature of the compartment space around the battery pack) the battery and the temperature of the coolant flowing into the battery pack. For this reason, the ambient temperature and the coolant temperature serve as an additional input to the LPTN model. With the heat load, ambient temperature and coolant in temperature for each different BTMS, both the battery pack and the coolant out temperature can be calculated. In Figure 4.1 the links between the input and output of the two models are visualized.

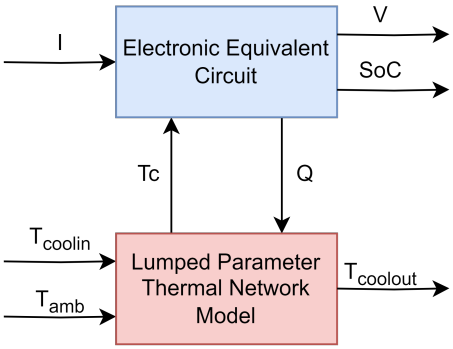

Figure 4.1: An overview of the intergration of the EECM and LPTN models

4.2. Electronic Equivalent Circuit Model

This section will describe how the electrical performance of the battery pack will be modeled. First, a general description of the concept of an electronic equivalent circuit model (EECM) along with a number of model definitions will be provided in subsection 4.2.1. This will be followed by an explanation on how different types of EECM can be used to model lithium-ion cells in subsection 4.2.2. The section will be concluded with an elaboration on how the EECM cell model can be integrated to form a battery pack model in subsection 4.2.3 and how the EECM output can be used to calculate the heat generation of a battery cell in subsection 4.2.4.

4.2.1. General Description

The equivalent circuit model uses electrical circuit components to form a specific circuit network to characterize the operational characteristics of the battery. This model establishes the relationship between the external characteristics exhibited by the battery during operation and the internal states of the battery itself [75]. The goal of a lithium-ion battery model is to provide accurate relationships between the characteristics of V, the state of charge (SoC), the temperature, and the state of health (SoH) [69].
From the statements above, it can be deduced that an EECM is providing a relation between battery states and voltage. Equation 4.1 shows what relation between output voltage and battery states is considered in this thesis work. From Equation 4.1 it can be seen that SoH is not included in the equation. This is because the to be developed model aims to model the voltage of the battery during a typical mission. Battery aging is a slow phenomenon that will only occur after a number of charge and discharge cycles [4]. For this reason, the change in SoH during the one mission (one charge/discharge cycle) is negligible. Therefore, SoH is considered constant during the flight duration and independent of the model time (t). The effect of SoH on the model will only be taken into account when determining the initial conditions but will not be modeled with the EECM. The influence of SoH of the battery on the initial conditions can be found in subsubsection 4.2.2.6.

$$V(t) = f(SoC(t), I(t), T(t)) \tag{4.1}$$

In the literature many different ways of determining the SoC of a battery can be found [3]. For this thesis work the decision was made to use a simple method of determining the battery SoC in the form of the Coulomb counting method. With Coulomb counting, the amount of remaining electrical charge inside a battery is determined by integrating the current being drawn or put in to the battery over time. Equation 4.2 shows what this looks like in equation form.

$$SoC(t) = SoC(t_0) - \frac{\int_{t0}^{t} I(t)dt}{Q_0} \tag{4.2}$$

4.2.2. Types of EECMs

EECM use different electrical circuit components such as resistors, capacitors, voltage and current sources. There are many different configurations of these components that result in different types of EECMs. The most simple EECM is the open circuit voltage model (OCV). This model is very simple and only links the open-circuit voltage of the battery cell to the SoC at the specified moment of time. The only electrical component used in this model is a voltage source.
The relationship between OCV and SoC can typically only be obtained for a constant current discharge curve, as in Figure 4.2. In Figure 4.2 it can be seen that at an SoC of around 1 there is a very sharp voltage drop. The OCV curve then decreases roughly linearly between SoC 0.95 and 0.15. After SoC 0.15 the voltage again drops steeply. For an explanation on why the OCV curve shows this behavior, see [3]. As seen in Figure 4.2, the voltage of the OCV also depends on the temperature of the battery [89]. The battery temperature can thus be added as an additional input to the OCV model. The OCV behavior can be captured by extracting the OCV value at various SoCs and storing these values in a lookup table. Using experimental data to extract values for the circuit parameters and storing these in look-up tables is also the basis of the other EECMs described in the remainder of this section.

$$V(t) = V_{OC}(SoC(t), T(t)) \tag{4.3}$$

The Open Circuit Voltage model is the simplest form of EECM and does not model effects such as voltage drops due to internal resistance or any voltage dynamics of the battery. In order to model these effects, additional electrical components such as resistors and resistor-capacitor pairs will need to be added to the circuit.

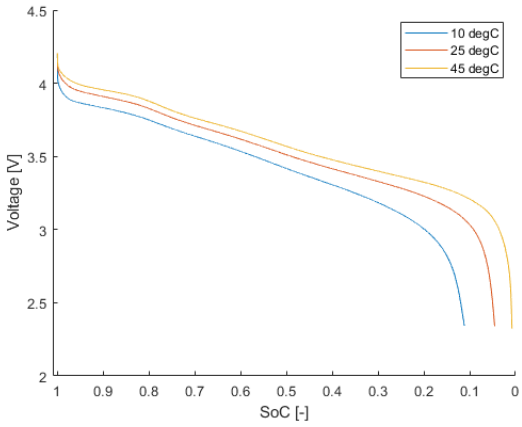

Figure 4.2: The relation between OCV and SoC

The next 3 sections will provide an overview of these more elaborate types of EECM in increasing order of model complexity.

0-RC Model

One of the most widely used EECM battery cell models is the 0-RC model. This model adds to the OCV model by adding a resistor in series to the OCV voltage source [18], as seen in Figure 4.3. The voltage equation for this model can be seen in Equation 4.4. For this model, the internal resistance R_0 can be determined by connecting a load to the battery to a fully charged battery and detecting both the terminal voltage and the current [69]. Since the load resistance is known, the excess voltage drop compared to the OCV can be attributed to the internal resistance. Ohms law can then be used to determine the internal resistance.

$$V(t) = V_{oc}(SoC(t), T(t)) - I(t) \cdot R_0(SoC(t), T(t)) \tag{4.4}$$

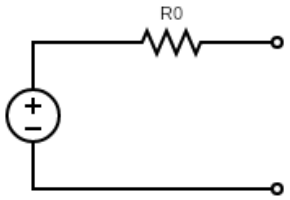

Figure 4.3: Schematic of 0-RC or R_0 EECM

This model does not explicitly consider the influence of the SoC and the temperature of the battery on the internal resitance. However, the voltage and current measurements when an external load is attached could be repeated at various SoC levels and temperatures. This will create a lookup table for R_0 in the various internal states of the battery. The measurement data required for this procedure are usually available on the specification sheet of a battery cell in the form of a standard continuous discharge test. The creation of lookup tables for the electrical parameters at different batteries states from the experimental data is called parameter estimation. The exact procedure on how this parameter estimation can be performed, what experimental data are required, and how the experimental data can be obtained will be explained in chapter 5. Throughout this report, the term configured model will be mentioned. With a configured model, one means an EECM for which the parameters in the component lookup tables have been estimated.
As mentioned in [3], none of the electrical components in the 0-RC EECM has any dynamic component, and therefore this type of circuit cannot model any dynamic voltage response. This shortcoming can be overcome by adding a parallel resistor-capacitor (RC) pair to the circuit. This circuit type will be explained in more detail in the next section.

1-RC Model

One of the main shortcomings of the 0-RC or R_0 model is that it cannot model any voltage dynamics of the battery. One of the ways in which an electrical circuit can model voltage dynamics is by adding a resistor-capacitor pair to the circuit, as seen in Figure 4.4. The voltage equation for this model can be seen in Equation 4.5 with U_1 being the voltage drop of the RC pair. The continuous-time expression for U_1 can be seen in Equation 4.6[72].The expression contains a exponential decay function since the charge across a capacitor cannot change instantaneously. With the change in charge $\Delta Q = I\Delta t$, there must always be a non-zero time before the charge can change a non-zero amount, unless there is an infinite current. τ in Equation 4.6 is the time constant and the product of the resistance and the capacitance of the RC pair, as seen in Equation 4.7. Each RC pair therefore adds two parameters to be estimated, the resistance and the capacitance of the pair. In the parameter estimation, the decision was made to estimate the time constant instead of the capacitance of the RC pair. The rationale behind this will be provided in chapter 5

$$V(t) = V_{oc}(SoC(t), T(t)) - I(t) \cdot R_0(SoC(t), T(t)) - U_1(SoC(t), T(t), I(t)) \tag{4.5}$$

$$U_1 = V_0 e^{\frac{-t}{\tau}} \tag{4.6}$$

$$\tau = R_1(SoC(t), T(t)) \cdot C_1(SoC(t), T(t)) \tag{4.7}$$

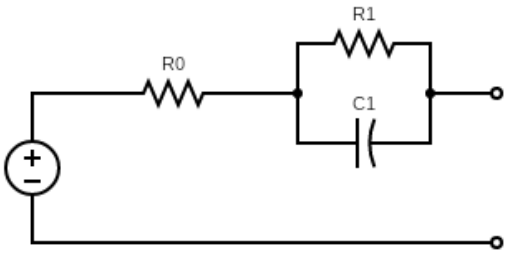

Figure 4.4: Schematic of 1-RC or Thevin Equivalent Circuit EECM

It is more useful to rewrite Equation 4.6[71] as a discrete-time ordinary difference equation (ODE), since the implementation of this model will be done in Matlab. ODEs better suit the construction and calculations of the MATLAB model [71] as they can be written in discrete time steps. The discrete form can be seen in Equation 4.8 where j denotes the time step with Equation 4.9. The full voltage equation can then be written in discrete form as in Equation 4.10.

$$U_{1,j+1} = \exp\left(-\frac{\Delta t}{R_1 C_1}\right) U_{1,j} + R_1 \left[1 - \exp\left(-\frac{\Delta t}{R_1 C_1}\right)\right] I_j \tag{4.8}$$

$$U_{1,0} = 0 \tag{4.9}$$

$$V_j = OCV - R_0 I_j - U_{1,j} \tag{4.10}$$

The addition of an RC pair to the R_0 model makes the equivalent circuit model of 1-RC or Thevenin ([18], [69]). By adding the capacitor to the circuit, the circuit has an element that can act as a voltage buffer, and therefore model voltage dynamics. As shown in [3] the addition of the RC pair allows the model to give better results than the 0-RC model because electrical and non-electrical losses are modeled by R_0 and R_1. A split can be made between the voltage drop due to the internal resistance of the batteries R_0, which causes an instant voltage drop, and the more gradual voltage drop due to diffusion. In Figure 4.5 this separation can also be observed. The step drop denoted by $|\Delta u_0|$ is the voltage drop due to internal resistance and $|\Delta u_d|$ denotes the voltage drop due to diffusion.

The voltage diffusion is the phenomenon that, in relaxation mode, without current being drawn or supplied to the battery, the voltage gradually reduces to its open-circuit equilibrium voltage. After the current has been drawn from the battery, the ions in the battery are no longer in a steady state. When no more current is being

drawn from the battery, it takes some time for the battery to reach a steady state again. This is what causes the voltage diffusion. This effect can be seen in Figure 4.5, where the voltage response to a pulsed charge and discharge current is plotted. A clear instantaneous straight voltage drop can be seen, which can be attributed to the ohmic polarization, and a more exponential curved voltage drop follows the initial straight voltage drop, which is caused by the diffusion voltage.

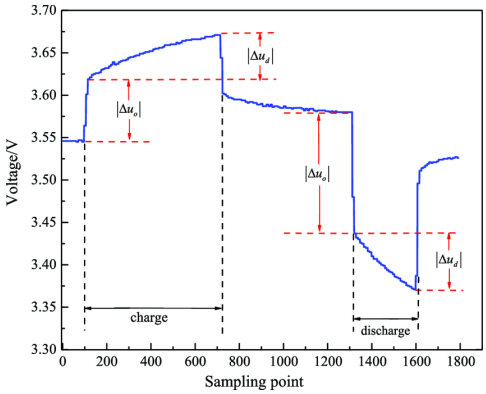

Figure 4.5: A visualization of the voltage drop due to ohmic- (ΔU_0) and diffusion polarization (ΔU_d)[45]

However, the 1 RC model cannot adequately model the capacitance effect of a battery cell [69]. The capacitance effect is that, next to an internal resistance, a nonideal battery acts a little like a capacitor. This gives the effect of a "phantom capacitor" that appears between the positive and negative electrodes of the non-ideal battery. When the battery is suddenly connected to a load, the capacitive effect allows a brief and sudden surge or a "transient" of current to flow out of the battery [58]. This effect can be modeled by adding an addition of another RC-pair to the circuit. This 2-RC model will be described in the next section.

2-RC Model

With the addition of an RC pair, the EECM was able to model the diffusion voltage of the battery. However, transients due to the capacitance effect could not be accurately modeled yet [69]. The voltage equation for the 2-RC model can be seen in Equation 4.11 and the circuit schematic in Figure 4.6. The 2-RC pair model is called a second-order EECM. A second-order EECM is defined as a dual polarization model that can provide a refined representation of polarization characteristics, concentration polarization, and electrochemical polarization independently [31]. The 2-RC model includes the effective capacitance C_1 and C_2, which represent the transient response of the batterys charge/discharge process and the polarization characteristic [71]. The voltage drops over the RC pairs can be calculated in a similar manner with a linear ordinary differential. This allows the voltage equation to be written in discrete form along with the RC-voltage drops to better suit the Matlab modeling structure. These equations can be seen in Equation 4.12, Equation 4.13, and Equation 4.14.

$$V(t) = V_{oc}(SoC(t), T(t)) - I(t) \cdot R_0(SoC(t), T(t) - U_1(SoC(t), T(t), I(t)) - U_2(SoC(t), T(t), I(t)) \tag{4.11}$$

$$V_j = OCV - R_0 I_j - U_{1,j} - U_{2,j} \tag{4.12}$$

$$U_{1,j+1} = \exp\left(-\frac{\Delta t}{R_1 C_1}\right) U_{1,j} + R_1 \left[1 - \exp\left(-\frac{\Delta t}{R_1 C_1}\right)\right] I_j \tag{4.13}$$

$$U_{2,j+1} = \exp\left(-\frac{\Delta t}{R_2 C_2}\right) U_{2,j} + R_2 \left[1 - \exp\left(-\frac{\Delta t}{R_2 C_2}\right)\right] I_j \tag{4.14}$$

With the addition of the extra RC pair, the model is able to model the batteries voltage more accurately. The accuracy of the model can be even further increased by adding even more RC branches to the circuit to create 3-RC, 4-RC to N-RC models. The increase in model accuracy comes at the cost of model complexity and computational cost. A model with more RC branches has more look-up tables to be stored and looked through to calculate the model voltage since each look-up table holds the components' value for combinations of SoC and temperature. These extra lookup tables increase the computational cost of the model and slow it down. Since the to-be-developed model will not model a single cell but a complete battery pack, which consists of

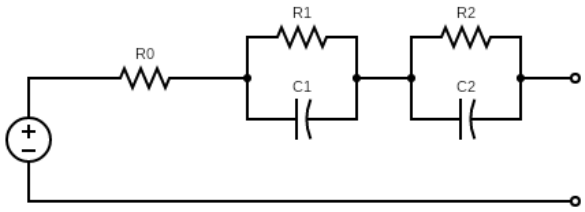

Figure 4.6: Schematic of 2-RC or Dual Polarization EECM

many cells, it is important to have a good trade-off between model accuracy and computational cost of the single-cell models. Even a moderately slow single cell model would greatly increase the time needed to model a full battery pack that can contain more than 1000 single cells, all of which would need to be modeled. For this reason, the decision was made not to use an EECM with more than three RC branches in the full pack model.
The difference in terms of model accuracy and computational cost when modeling a single battery cell between 0-, 1-, 2-, and 3-RC EECM in this thesis work will be investigated. However, for the full pack model the amount of RC branches will be limited to two as in [3] it was found that this amount of RC pairs would provide a good balance between model accuracy and computational cost. This comparison between models will be presented in subsection 6.3.4. An additional reason to not use an excessive amount of RC-pairs is that increasing the amount of RC-pairs increases the amount of time the parameter estimation takes. This will be discussed in more detail in chapter 5.

Self-Discharge

The phenomena of self-discharge of a battery is the phenomenon in which internal chemical reactions reduce the stored charge of the battery without any connection between the electrodes or any external circuit [77]. This phenomenon can be modeled by adding a resistor in parallel to the output terminals of the circuit. This is called a parasitic branch, and an example of such a circuit can be seen in Figure 4.7. For lithium electrochemistry, the parasitic branch (containing R_{self}) is often neglected in modeling lithium cells, due to its high coulombic efficiency and low self-discharge under typical operating conditions ([32], [12]). Also, for this thesis work the battery will mainly be modeled when in operation. This means that either current is being drawn or supplied to the battery. When current is being supplied or drawn from the battery, a load is connected between the electrodes and therefor there will be no self-discharge of the battery. For this reason and the reason that LIB have a low-self discharge of themselves, it was decided to not include the parasitic branch in the EECM models.

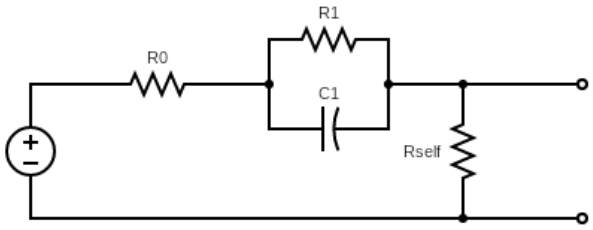

Figure 4.7: Schematic of 1RC EECM with self discharge

Hysterisis

Hysteresis is a phenomenon in which an output lags behind its input when the system changes direction. In battery systems, this is most commonly seen after charging when the open circuit voltage is different from the OCV after discharging to the same SoC. It can significantly affect the accuracy of an SoC estimation algorithm and, therefore, the entire system performance [93].
The decision was made not to include the hysteresis effect in the EECM model. This was done because this effect is only prevalent when the current changes direction. Unlike an electric car, which has regenerative breaking, the Pipistrel Velis Electro does not possess the ability to regenerate electric energy during descent or under no-power conditions. Normally during these conditions, the electric motor would turn into a generator generating electrical energy, and therefore the current direction would reverse, causing a hysteresis effect. This means that the only time the current changes direction is when the airplane is charged after a mission. The current does not change direction during a mission, and since the aim of the EECM is to model the voltage of the battery pack during a mission the hysteresis effect will be omitted.

Battery Aging

Battery aging is the phenomenon of a lithium-ion battery cell performance deteriorating as it is used. There are two types of battery aging; cyclic aging and calander aging. Calendar aging comprises all aging processes that lead to degradation of a battery cell regardless of charge-discharge cycling. [38] This phenomena usaully occurs when a battery is stored for a long period of time. As the goal of the model in this thesis is to model the battery during a flight, there is discharge of the battery occurring, and therefore no calendar aging will occur. For this reason, calendar aging is not considered in this model.
The second aging mechanism is cyclic battery aging. This aging of the battery cell occurs due to repeated charge and discharge cycles [66]. Cyclic aging causes the performance of the batteries to degrade. This effect can be seen in the open-circuit voltage, internal resistance, and available battery capacity. The relation between the open-circuit voltage of the battery age and the internal resistance is complex and is not yet well understood. However, since cyclic battery aging only occurs after a great number of cycles and this model only models one cycle in the form of a flight, it is expected that the battery performance does not deteriorate during a flight due to cyclic aging. However, what needs to be considered is the aged state of the battery at the start of the flight. This can be done by using the SoH parameter from the flight data. With the definition of SoH as seen in Equation 2.3, the aged battery capacity can be calculated using Equation 4.15. This aged battery capacity is now used by the model to calculate the SoC of the battery during a flight.

$$Q_{aged} = Q_{initial} \cdot SoH \tag{4.15}$$

4.2.3. From Cell to Pack

In subsection 4.2.2 various EECM models are described to model a single LIB cell. These models only model a single LIB cell. A battery pack is a combination of multiple LIB cells arranged in a parallel and/or series electrical configuration. This subsection will explain how single LIB cell models can be combined to create a pack electrical model. First, an explanation will be provided on how multiple LIB cells in series can be used to increase the output voltage of the battery pack. Second, the calculation procedure for the calculation of the minimum required parallel battery cells will be provided.

Series Connections

The main factor that determines how many cells are needed to be connected in series is the output voltage of the battery pack. The typical output voltage of an 18650 LIB is 3.6 Volts [24]. When connecting multiple cells in an electrical series connection, the output voltage of the battery can be increased to multiples of the battery cell voltage (in nominal conditions multiples of 3.6 volts).
A number of cells connected in series is called a string. The number of cells that must be connected in series can be calculated using Equation 4.16. Equation 4.16 does assume that there is no voltage drop caused by the connections between the cells. In practice, the connecting wires have a small resistance, which could cause small voltage drops, resulting in a lower pack voltage. However, connection wires are made of good conducting material, such as copper, which has low resistivity [78]. Besides this, the wires are very short, so their internal resistance and thus the voltage drop are negligible. The resistance of a wire can be calculated using Equation 4.17. When considering a copper wire with a length of 10 cm and a gauge of 12 (imperial unit for diameter, 2.05 mm), which is common for electrical wires carrying a maximum of 20 A [70], the internal

resistance would be only 3.5e-4 Ohm, as calculated with Equation 4.17. This is a factor of 100 less than the internal resistance of the cell itself (45 $m\Omega$ [47]) and therefore can be neglected.

$$N_{series} = \lceil \frac{V_{pack}}{V_{cell_{nom}}} \rceil \tag{4.16}$$

$$R = \rho \cdot \frac{L}{A} \tag{4.17}$$

Parallel Connections

The number of parallel connections required by a battery pack depends on two factors. The first factor is the maximum discharge current rate that can be drawn from a single cell. When the voltage is known, the amount of current that needs to be drawn from the battery pack can be calculated using Equation 4.18. The number of parallel cells can then be calculated by dividing this current by the maximum continuous cell discharge current allowable as in Equation 4.19.

$$I = \frac{P}{V_{pack}} \tag{4.18}$$

$$N_{parallel_{current}} = \lceil \frac{I_{drawn}}{I_{max_{con}}} \rceil \tag{4.19}$$

The second factor that determines the number of parallel cells is the capacity that the battery pack must have. The only way to increase the capacity of a battery pack without increasing its output voltage is by connecting multiple strings in parallel to each other. The amount of parallel strings needed this way can be calculated using Equation 4.20. The actual number of strings or cells connected in parallel is dictated by the maximum number of parallel strings due to current restrictions or the energy capacity constraint as seen in Equation 4.21.

$$N_{parallel_{capacity}} = \lceil \frac{Q_{pack}}{Q_{cell}} \rceil \tag{4.20}$$

$$N_{parallel} = \max\{N_{parallel_{current}}, N_{parallel_{capacity}}\} \tag{4.21}$$

4.2.4. Battery Cell Heat Generation

The heat generation within a LIB cell can generally be attributed to two phenomena. These are irreversible and reversible heating as seen in Equation 4.22. This subsection will explain how both heat terms can be calculated. First, an explanation will be provided on the irreversible heat term followed by an elaboration on the reversible heat term.

$$\dot{Q} = \dot{Q}_{irrevs} + \dot{Q}_{revs} \tag{4.22}$$

Irreversible heat

The irreversible heating term can be attributed to heat generation as a result of voltage drop. The voltage drop is the difference between the OCV of the battery cells and the terminal voltage, as seen in Equation 4.23. This voltage drop is the result of current flowing through the restive components of the battery. In the EECM analogy, the restive components would be the resistors in the electronic circuit. The resistance of the capacitors can be neglected in this case, since an ideal capacitor has an infinite amount of resistance. The equivalent resistance of the parallel RC pair would then become equal to the resistor resistance value. This impedance of resistor components produces a voltage drop, which in turn causes a joule heating effect [82]. The amount of joule heating can be calculated by multiplying the voltage drop with the current as in Equation 4.25.
Since the topology of the EECM model was chosen in this thesis, the voltage drop term can be calculated by multiplying the total equivalent resistance of the EECM model with the current. Since all the resistive elements of the EECM are connected in series, this is simply the sum of all resistance values of each component of the circuit. With this in mind, Equation 4.25 can be rewritten as Equation 4.26. Note that because of the square of the current, this heat term will always be positive no matter the direction of the current.

$$\eta = (OCV - V) \tag{4.23}$$

$$R_{eq} = \frac{1}{\frac{1}{R_{resistor}} + \frac{1}{R_{capacitor}}} \tag{4.24}$$

$$\dot{Q}_{irrevs} = I(OCV - V) \tag{4.25}$$

$$\dot{Q}_{irrevs} = I^2 \cdot R_{eq} \tag{4.26}$$

Reversible heat

The reversible heat term can be attributed to the heating due to the change in the entropy of the battery. Entropic heat is generated when the lithium content of the electrode changes, causing the entropy of the electrode materials to change [14].The change in entropy can be either positive or neagative, thus generating or absorbing heat [86]. The equation for reversible heat generation can be seen in Equation 4.27 where n is the number of electrons that contribute to the reaction (1 for lithium batteries) and F is the Faraday constant [82]. By rewriting the Gibbs free energy equation, the expression for the change in entropy seen in Equation 4.28 can be derived [82]. When combining Equation 4.27 and Equation 4.28 the reversible heat equation can be written as in Equation 4.29.

$$\dot{Q}_{revs} = -\frac{I}{nF} T\Delta S \tag{4.27}$$

$$\Delta S = nF\frac{\delta V_{OC}}{\delta T} \tag{4.28}$$

$$\dot{Q}_{revs} = -IT\frac{\delta V_{OC}}{\delta T} \tag{4.29}$$

Determination of Entropic Coefficients

In Equation 4.29 the factor $\frac{\delta V_{OC}}{\delta T}$ is called the entropic coefficient. Accurate determination of this coefficient is crucial for an accurate calculation of the reversible heat term. In this thesis two ways of determining the entropic coefficients of the lithium-ion battery cells will be proposed. One will be the standard experimental way, and the second uses the data from a hybrid pulse power characterization (HPPC) test with the method stated in [27]. What an HPPC test is and how it will be conducted will be explained in section 5.2.
The first standard experimental method is the method described in [74]. With this method, the entropic coefficients can be obtained by finding the slope of the open-circuit voltage (OCV) with temperature. This is commonly done with a potentionmetric method [36]. In this method, the battery cell is charged or discharged to a certain SoC level at a certain temperature, and then the output voltage is measured. The battery cell is then heated or cooled to another temperature and, again, the output voltage is measured. This is repeated at several temperatures, after which the battery is discharged to another SoC level, and the process is repeated. This results in data points roughly on a linear line in a voltage versus temperature plot at various SoC levels. An example of such a plot can be seen in Figure 4.8. With a linear regression of these data points, the slope of the voltage with respect to temperature can be determined, resulting in the entropic coefficient. The downside of using this method is that the tests to gather the data points can take a very long time. After each SoC or temperature change, the battery must rest for quite some time to ensure that the complete battery has reached the required temperature level. Additionally, after each discharge pulse the battery should be left to rest a certain amount of time for the batteries voltage to completely diffuse to its steady state value and thus for the battery to reach steady state. The number of data points required for these tests is quite large. For example, if 10 SoCs are to be considered at 4 temperatures, this would result in 40 data points. If measuring every data point takes around 1 hour, the total test would take up to 40 hours, which is quite a substantial duration.

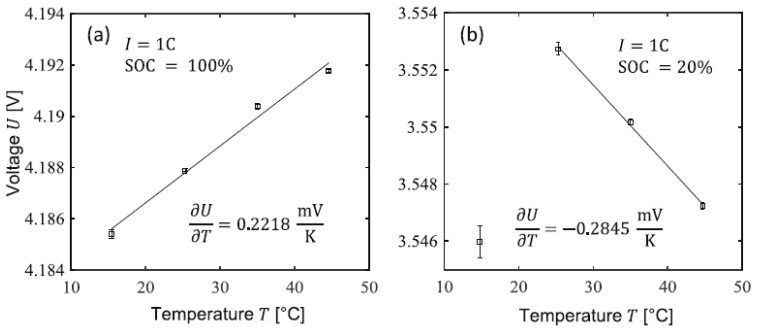

Figure 4.8: Example of the linear regression of the voltage data points to find entropic coefficient [27]

The method prescribed in [27] addresses the problem of time duration of the standard experimental method. As an alternative, the data collected during the HPPC test is used to obtain the required data points. During the HPPC test, the cell is already measured essentially at different SoC and temperature levels. In [27] the voltage measurements between the current pulses during the relaxation period are averaged and considered

to be the measured output voltage as needed for the linear regression to determine the slope. The downside of this method is that during the relaxation period the voltage does vary over time, so averaging is needed. A good measure to see if the voltage is properly relaxed during the period is to look at the standard deviation of the measurement. If the standard deviation is large, the voltage is not yet relaxed, and therefore care must be taken if the entropic coefficient is determined with this method.

4.3. Lumped Parameter Thermal Network Model

This section will explain how a battery pack containing battery cells can be modelled with the use of a lumped parameter thermal network. First, the concept of what is considered a node in this LPTN model will be described in subsection 4.3.1 along with how the thermal capacity of these nodes can be determined. Second, the links between the nodes and the surrounding elements will be elaborated on in subsection 4.3.2 and subsection 4.3.3 along with how an analogy of an electric circuit can be used to solve the network heat flow equations.

4.3.1. Nodes

In LPTNs the nodes are elements of lumped thermal capacitance [80]. With this modeling method, elements, such as a cell, are lumped into one node with one (averaged) temperature, of which the thermal mass is determined by all the thermal capacities of the elements being lumped together. The number of cells that are lumped together can vary and can be set by the user. Less cells being lumped into one node results in more overall thermal nodes and thus better model accuracy, but increases model computational complexity. An investigation of the effects of varying the number of thermal nodes will be presented in section 6.5.
For a node containing battery cells, the thermal mass or heat capacity can be determined by looking at the specific heat of the battery cell and multiplying it by its mass as seen in Equation 4.30. In Equation 4.30 C is the thermal mass in $[J/kgK]$, C_p is the specific heat of a component in $[J/kgK]$ and m_i is the mass fraction of the component. The specific heat of the battery cell can be determined by using the mixture rule. In this case, the mixture is made up of various components of the battery cell such as the anode, cathode, electrolyte, separator, etc. For NMC chemistry, this method results in a specific heat capacity of 1040 +/-34 [J / kgK] ([55], [46], [59]). In [59] it is also stated that the specific heat capacity varies with SoC and temperature. However, this variation for SoC is only between 2 and 5 %, and the variation due to temperature changes is even smaller. For this reason and to reduce the complexity of the model by not having specific heat as a function of the state of charge and temperature, the assumption was made to keep the specific heat of the nodes constant at 1040 [J / kg K].

$$C = \Sigma_{i=1}^{n} C_{p_i} \cdot m_i \tag{4.30}$$

4.3.2. Thermal Resistances

The nodes in the LPNT are connected to each other with thermal resistances. Thermal resistance is a measure of the resistance of a material to heat flow [81]. The value of this thermal resistance is primarly dependent on the way heat can be transferred. There are three main ways for heat transfer; conduction, convection, and radiation. An explanation of the three types of heat transport will be provided in the following sections.

Conduction

Thermal conduction is the diffusion of thermal energy (heat) within a material or between materials in contact. The general heat equation for conduction can be seen in Equation 4.31[2]. Equation 4.31 k is the conductivity of the material $[W/(m \cdot K)]$, A is the cross-sectional area $[m^2]$ through which heat flows. L is the length in $[m]$ and ΔT the temperature difference between two nodes. The thermal resistance for heat transport by conduction is calculated using Equation 4.32 with R_{cond} being the thermal resistance due to conduction.

$$\dot{Q}_{cond} = \frac{kA}{L}\Delta T \tag{4.31}$$

$$R_{cond} = \frac{L}{kA} \tag{4.32}$$

Convection

Convection (or convective heat transfer) is the transfer of heat from one place to another as a result of the movement of fluid. The integral form of the general heat equation for convection can be seen in Equation 4.33[2] this is also called Newton's law of cooling. In Equation 4.33 h is the convective heat transfer coefficient $[W/(m^2K)]$ and A is the surface area in contact with the fluid $[m^2]$. The thermal resistance for convective heat transfer can in turn be calculated using Equation 4.34.
The amount of heat transfer by the fluid is highly dependent on the motion of the fluid. Therefore, it is important to first establish whether the flow is laminar or turbulent. In laminar flow, the fluid moves in layers, and the fluid particles follow a smooth and continuous path. In this type of flow, heat is transferred only by molecular conduction within the fluid as well as the interface between the fluid and the surface. In turbulent flow, the path of the fluid particles is irregular, and even though the general trend of the motion is in one direction, eddies or mixing currents do exist. In addition to the modification of the heat transfer

mechanism, heat transfer is also increased due to energy being carried by the fluid particles through the flow streamlines and mixing with other particles in the fluid [2].
With convective heat transfer, the surface area in contact with the flow can usually be calculated from the geometric configuration. However, determining the convective heat transfer coefficient h is not as straightforward. When the type of flow is known, there are generally relations that can aid in determining the convective heat transfer coefficient. When using these empirical relations, care must be taken that they are used in the flow conditions to which they are applicable. This can be done by calculating the Reynolds, Prandtl, and Grasshof numbers and comparing if they fall within the applicable range of the empirical relation found. In general, there are two types of empirical relations. Relations describing natural convection (laminar flow) and relations describing turbulent convection (turbulent flow). A more detailed explanation of the differences in empirical correlations for these two types of convection can be found in [3].

$$\dot{Q}_{conv} = h \cdot A \cdot \Delta T \tag{4.33}$$

$$R_{conv} = \frac{1}{h \cdot A} \tag{4.34}$$

Radiation

Every object that has a certain temperature also emits heat in the form of radiation. The amount of heat that an object of a certain temperature emits as radiation can be calculated using the Stefan-Boltzmann law of radiation. This law can be seen in the form of an equation in Equation 4.35. In Equation 4.35 σ is equal to the Boltzmann constant, which has a value of $= 5.67 \text{ x } 10^{-8} J/s \cdot m^2 \cdot K^4$. This is a small value, which means that if either the area or temperature of the object is not very large, the amount of heat radiated from the object will not be large. For example, a battery cell at 20 $^\circ C$ of the standard 18650 form factor with a casing of aluminum (65 mm height, 18 mm diameter, and emisivity 0.05 [88]) would emit around $8 \cdot 10^{-2}$ Watts. This amount of heat emission is low compared to the amount of electrical power drawn from one battery cell (10 W). For this reason and because of the low emisivity of the aluminum casing material, the assumption will be made during this thesis work that radiative heating effects can be neglected.

$$\dot{Q}_{emit} = \sigma e A T^4 \tag{4.35}$$

4.3.3. Network Connections

In the previous sections, various modes of heat transport were described. With the description of these heat transport modes, it becomes possible to describe the network connections in the LPNT. When the network connections are described in the form of thermal resistances, the resulting network has a strong analogy with an electrical circuit. The analogies can be seen in Table 4.1. Typical solution methods such as Kirchoff voltage and current laws can now also be used to solve the thermal network equations [2].

Table 4.1: Thermal-Electrical System Analogy [2]

Quantity	Thermal System	Electrical System
Potential	T [K]	E [V]
Flow	$\dot{Q}$ [W]	I [A]
Resistance	R [K/W]	R [Ω]
Conductance	G=1/R [W/K]	G=1/R [S/m]
Capacitance	C [J/K]	C [f]
Ohm's law	$\dot{Q}$=T/R	I = E/R

The network connections in the LPNT are the thermal resistances from the cell to the coolant, to the other cells, and to the battery pack environment. An example of such a network model for 4 nodes (cells) is provided in Figure 4.9. The thermal resistance of the cell to the coolant ($R_{coolant}$) is the thermal resistance of the cell node to the wall past which the coolant flows. The thermal resistance of the cell to ambient conditions (R_{amb}) is the thermal resistance of the cell node to ambient conditions, which in the case of this model is the cabin temperature. The thermal resistance between two cells i,j is ($R_{i,j}$).

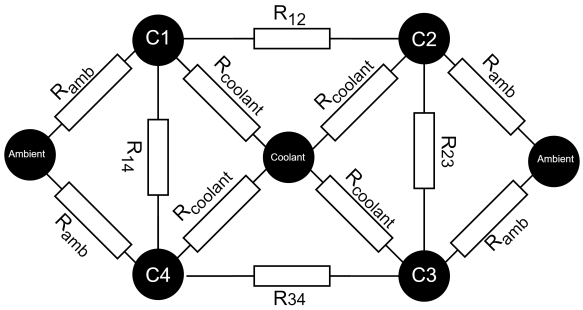

Figure 4.9: An example thermal network for 4 nodes

The calculation procedure to determine the values of these thermal resistances is highly dependent on the type of battery thermal management system used. In section 2.3 two battery thermal management systems, cold plate cooling and ribbon cooling, were described. In addition to these two thermal management systems, this thesis work will also investigate an additional thermal management system in the form of air cooling. The following subsections provide the procedure and schematics on the thermal paths used to calculate the thermal resistances for these three battery thermal management systems.
For each BTMS, an LPNT will be created for one 12x24 battery module as described in subsection 2.3.3. In total, each Pipistrel battery pack has four of these modules stacked vertically. It is assumed that a layer of insulating air is present between each module, and therefore each module is thermally isolated from each other. This also makes the modeling approach more modular and applicable to other types of battery pack arrangements. A geometric overview of the parameterization of the battery pack can be seen in Figure 4.10.

Ribbon Cooling

As described in section 2.3 ribbon cooling is cooling using a ribbon attached to the sides of the battery cells through which the coolant flows. To calculate the thermal resistances, first a geometric parameterization of the ribbon geometry is necessary. In Figure 4.12 and Figure 4.11 the geometric parameterization chosen can be seen. In Figure 4.11 ϕ is the angle of the ribbon. This angle indicates the amount of cell perimeter that is covered by the ribbon. t_{ribbon} and w_{ribbon} are the thickness and width of the ribbon, respectively. The thickness of the ribbon is the thickness of the wall of the ribbon and the width of the ribbon is the width of

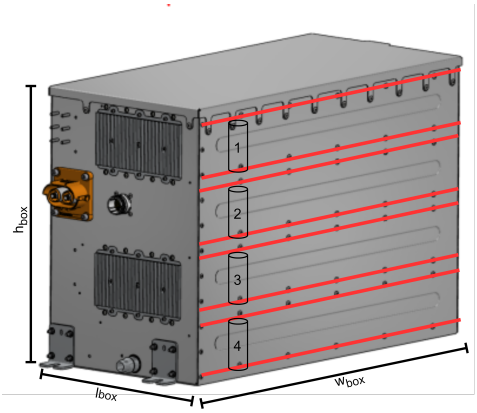

Figure 4.10: A geometric overview of the Pipistrel battery box [63]

the channel through which the coolant flows. Finally, in Figure 4.12 f_{ribbon} indicates the factor of the ribbon. This fraction indicates how much of the cell is covered by the ribbon in vertical direction.

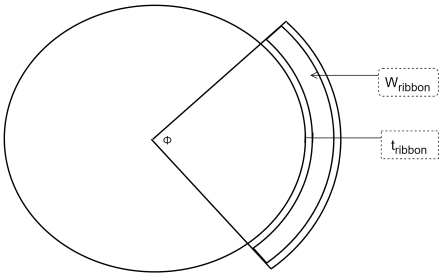

Figure 4.11: Ribbon cooling parameterization top view

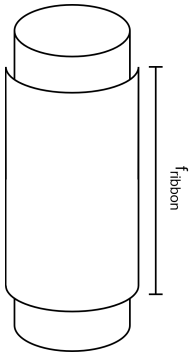

Figure 4.12: Ribbon cooling parameterization side view

With the geometric parameterization known, it becomes possible to determine the thermal paths and thermal resistances of those paths. The approach used to determine the thermal paths for ribbon cooling is similar to the approach described in [91] which is applied to a cold plate case and will be described in the next section. When the assumption is made that cell heat production occurs at the core of the cell and that the cell is lumped into one thermal mass, the heat has to be conducted through the ribbon to reach the coolant, resulting in the thermal path seen in Figure 4.13. There are two of the same thermal paths in parallel, since each cell will have a ribbon attached on two sides, allowing for parallel heat flow.
Individual conductive thermal resistances of the thermal path of the coolant in Figure 4.13 can be calculated using Equation 4.36 [91]. In Equation 4.36 k and c_d are the thermal conductivity of the ribbon material and the diameter of the cell, respectively. When determining the equivalent thermal resistance of Figure 4.13, the equivalent thermal resistance of the thermal path to the coolant can be found with Equation 4.37. There are two ribbon thermal resistances present since there is a ribbon attached to both sides of the battery cell, and thus a parallel thermal path is formed.

$$R_{ribbon} = \frac{t_{ribbon}}{k \cdot \frac{\phi \cdot \pi}{360} \cdot c_d \cdot c_h \cdot f_{ribbon}} \tag{4.36}$$

$$R_{coolant} = \frac{R_{ribbon}}{2} \tag{4.37}$$

The calculated thermal resistance of the coolant is the thermal resistance from the cell to the wall ribbon through which the coolant flows. To calculate the actual heat transfer from this coolant wall to the coolant, additional modeling is required. This heat transfer in the cooling channel is modeled with a Simscape thermal liquid pipeline element [49]. This pipe element calculates the heat transfer rate based on convective heat transfer. For laminar flow in the coolant channel, the Nusselt number to calculate the convective heat transfer coefficient is set to 3.66 [49]. For turbulent flow in the channel the Nusselt number can be calculated using Equation 4.38 which is the Gnielinski correlation [49]. In Equation 4.38 f_{avg} is the average Darcy friction coefficient, Re is the averaged Reynolds number, and Pr is the average Prandtl number. f_{avg} can be calculated using Equation 4.39 . In Equation 4.39 r is the roughness of the pipe surface in [μm] which depends on

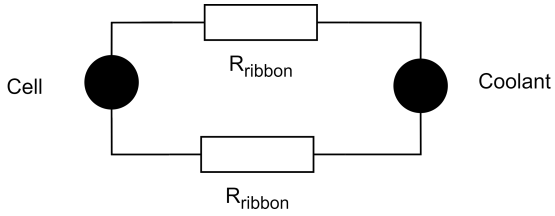

Figure 4.13: The coolant thermal path with ribbon cooling

the material and finish from which the cooling ribbon is made. D is the hydraulic diameter in $[m]$ of the cooling channel. As the cooling ribbon can be approximated as a rectangle, the hydraulic diameter of the channel can be calculated using Equation 4.40. The convective heat transfer coefficient can be calculated as in Equation 4.41 with k being the averaged thermal conductivity.

$$Nu_{tur} = \frac{\frac{f_{avg}}{8}(Re_{avg} - 1000)Pr_{avg}}{1 + 12.7\sqrt{\frac{f_{avg}}{8}}(Pr_{avg}^{2/3} - 1)} \tag{4.38}$$

$$f = \frac{1}{\left[-1.8\log(\frac{6.9}{Re} + (\frac{1}{3.7}\frac{r}{D})^{1.11})^2\right]} \tag{4.39}$$

$$D_h = \frac{2 \cdot w_{ribbon} \cdot c_h \cdot f_{ribbon}}{w_{ribbon} + c_h \cdot f_{ribbon}} \tag{4.40}$$

$$h = Nu \cdot \frac{k_{avg}}{D_h} \tag{4.41}$$

The ambient thermal path is again determined with a method similar to that presented in [91]. First, the heat needs to be conducted away from the cell walls into the still air inside the battery pack. This still air then convects the heat away to the enclosure walls. The heat is then conducted through these walls and convected into the cabin. A schematic of the situation can be seen in Figure 4.14. The heat can be convected away from all vertical sides of the battery, so there are 4 parallel thermal paths.

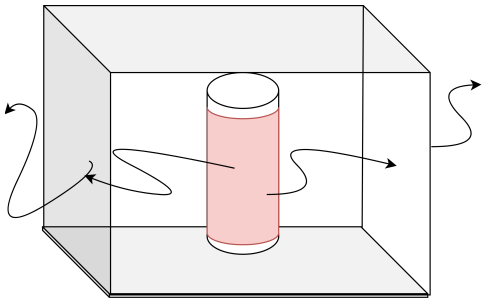

Figure 4.14: A schematic representation of the ambient thermal path with ribbon cooling

From the schematic overview provided in Figure 4.14 the resistor analogy can be derived for the thermal path to the ambient of the cooling solution of the ribbon. This thermal resistor analogy schematic can be seen in Figure 4.15. Each resistor in Figure 4.15 can be calculated with Equation 4.42, Equation 4.43, Equation 4.44, Equation 4.45, Equation 4.46, Equation 4.47 or Equation 4.48. The equivalent thermal resistance for the side and front path can be calculated using Equation 4.49 and Equation 4.50. The total equivalent thermal resistance can be calculated using

$$R_{conv_{cell}} = \frac{1}{h_{free_{conv}} \cdot \pi \cdot c_d \cdot c_h \cdot f_{ribbon}} \tag{4.42}$$

$$R_{conv_{front,in}} = \frac{4 \cdot t_{box}}{h_{free_{conv}} \cdot w_{box} \cdot h_{box}} \tag{4.43}$$

$$R_{conv_{side,in}} = \frac{4 \cdot t_{box}}{h_{free_{conv}} \cdot l_{box} \cdot h_{box}} \tag{4.44}$$

$$R_{cond_{front}} = \frac{4 \cdot t_{box}}{k \cdot w_{box} \cdot h_{box}} \tag{4.45}$$

$$R_{cond_{side}} = \frac{4 \cdot t_{box}}{k \cdot l_{box} \cdot h_{box}} \tag{4.46}$$

$$R_{conv_{front,out}} = \frac{4 \cdot t_{box}}{h_{free_{conv}} \cdot w_{box} \cdot h_{box}} \quad (4.47) \qquad R_{conv_{side,out}} = \frac{4 \cdot t_{box}}{h_{free_{conv}} \cdot l_{box} \cdot h_{box}} \quad (4.48)$$

$$R_{eq_{front}} = R_{conv_{cell}} + \frac{R_{conv_{front,in}} + R_{cond_{front}} + R_{conv_{front,out}}}{2} \quad (4.49)$$

$$R_{eq_{side}} = R_{conv_{cell}} + \frac{R_{conv_{side,in}} + R_{cond_{side}} + R_{conv_{side,out}}}{2} \quad (4.50)$$

$$R_{amb} = \frac{1}{\frac{1}{R_{eq_{front}}} + \frac{1}{R_{eq_{side}}}} \quad (4.51)$$

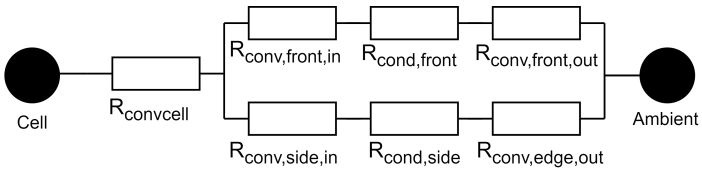

Figure 4.15: The thermal resistor schematic of the ambient thermal path with ribbon cooling

The thermal path between cells can be determined by looking at how heat is transported between battery cells. In the hexagonal battery cell stacking arrangement, there are small gaps between the cells, so they are not touching directly. This means that the main way of heat transport between the battery cells is by natural convection of air between the battery cells. This results in the resistor analogy schema as seen in Figure 4.16. The value of R_{inter} can be calculated using Equation 4.52.

$$R_{inter} = \frac{1}{(\frac{\pi}{2} - \frac{1\phi}{360}) \cdot c_d \cdot c_h \cdot h_{free,conv}} \quad (4.52)$$

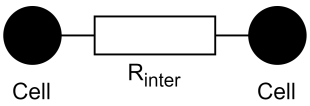

Figure 4.16: The thermal resistor schematic for the inter cell heat transport

Cold Plate Cooling

As described in subsection 2.3.3 cold plate cooling is a cooling strategy in which two aluminum plates are attached to the top and bottom of the battery cell. Heat flows from the battery cell to this plate by thermal conduction. Through this plate, channels are extruded through which coolant flows, removing the heat from the plate. As in previous sections, the thermal resistance of this cooling strategy to coolant, ambient and intercell conditions must be calculated. The 2-dimensional geometric view (in battery cell radial direction) can be seen in Figure 4.17. In Figure 4.17 t_{plate} is the thickness of the cooling plate. $D_{channel}$ and $N_{channel}$ relate to the cooling channels and are the diameter of the cooling channel and the number of channels, respectively. t_{ins} is the thickness of the electrical insulation layer between the cell and the cold plate. Since the battery cell generates electricity at its caps and the plate is made of aluminum, which also conducts electricity, a small insulation layer is needed to prevent this conduction of electricity. This layer has low thermal conductivity but is rather thin, usually on the order of a couple of tenths of a millimeter.

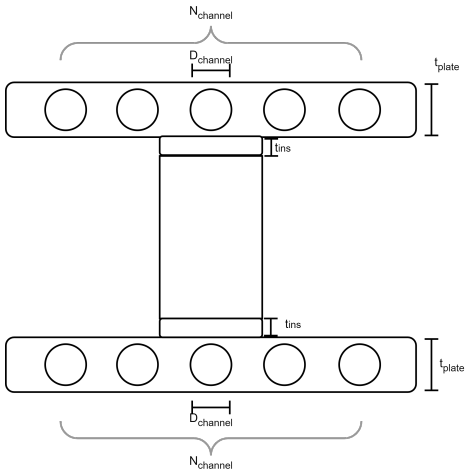

Figure 4.17: The 2-dimensional geometric view (in battery cell radial direction) of the cold plate cooling

With the geometric parameterization known, it becomes possible to determine the thermal path from the cell to the coolant. A schematic of the thermal path from the cell to the coolant for cold plate cooling can be seen in Figure 4.18. The conductive thermal resistances can be calculated with Equation 4.53 and Equation 4.54, respectively, and are derived from [91]. The total equivalent conductive thermal resistance can be calculated using the electrical resistor analogy. The total conductive thermal resistance of the cell to the coolant can be determined using Equation 4.56 which takes into account a cold plate attached to the top and bottom of the cell. The calculated thermal resistance is again the thermal resistance to the wall of the coolant channel. The actual heat transfer to the coolant is again modeled with Simscape thermal liquid pipe element just as it was with ribbon cooling. The convective heat transfer in this pipe element is calculated in the same manner as for the Ribbon cooling with the main difference being the way the hydraulic diameter of the channel is calculated. As the channel is now circular and not rectangular, the hydraulic diameter is equal to the diameter of the circular channel.

$$R_{ins} = \frac{t_{ins}}{k_{ins} \cdot c_s} \tag{4.53}$$

$$R_{plate} = \frac{t_{plate}}{2k \cdot c_s} \tag{4.54}$$

$$R_{eq} = R_{ins} + R_{plate} \tag{4.55}$$

$$R_{coolant} = \frac{R_{eq}}{2} \tag{4.56}$$

The ambient thermal path for the cold plate cooling option can be determined in the same way as for the ribbon cooling. The only difference now is that there is no ribbon that covers part of the cell, so the area for heat convection is larger. This adjustment can be made by adjusting Equation 4.42 to Equation 4.57 and removing the ribbon factor.

$$R_{conv_{cell}} = \frac{1}{h_{free_{conv}} \cdot \pi \cdot c_d \cdot c_h} \tag{4.57}$$

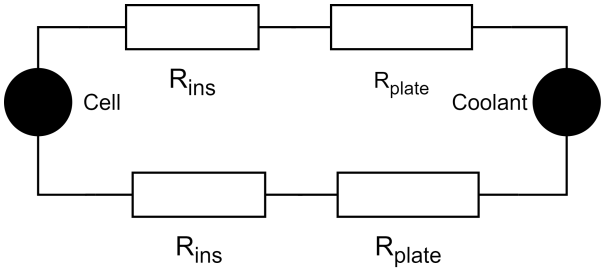

Figure 4.18: The thermal resistance diagram for the coolant thermal path of the cold plate cooling

Air Cooling

With air cooling, cool air blows directly into the battery pack along the battery cells. For the air cooling case considered in this thesis work, it is assumed that air is blown in from one of the sides of the battery pack and flows out from the other. Therefore, the air followws a horizontal path between the intercell gaps, as seen in Figure 4.19. Each gap between two rows of cells is considered as a channel through which air is blown.

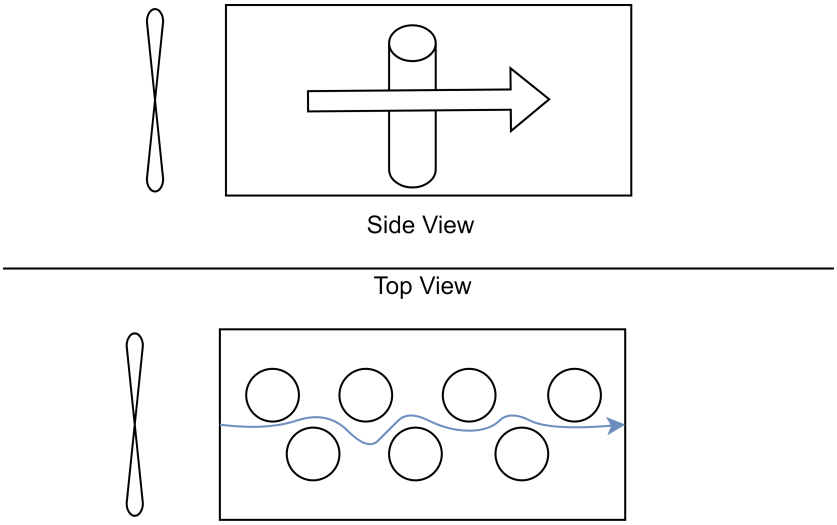

Figure 4.19: Airflow in air cooled BTMS

Since air is blowing directly onto the battery cell, the conductive thermal resistance of the cell to coolant air is zero because there is no material to conduct through. The convective heat transfer from the cylindrical battery cell to the air is modeled with the use of another Simscape pipe element. This pipe element is different from the ones used for liquid cooling as the heat transport medium is now a gas. The pipe element models the gas properties by solving the momentum, energy, and mass conservation equations under the assumption of an ideal gas. However, the convective heat transfer coefficient is again determined using the Gniensliki correlation Equation 4.38. For the path to ambient, it is considered that part of the air blowing past the cells inside the batteries convects heat to the front and back of the battery pack, from these sides the heat is transported by means of natural convection outward to the ambient conditions. The thermal resistor analogy scheme can be seen in Figure 4.20. Each resistor in Figure 4.20 can be calculated with the same equations as listed in the air cooling case. However, Equation 4.43 needs to be adjusted to take into account that on the inside of the battery pack there is not natural convection but forced convection. The heat transfer coefficient for forced convection can be determined when the flow velocity is known using [21]. The flow velocity can be determined when the mass flow rate generated by the fan is known.

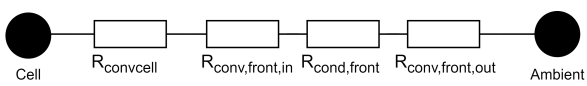

Figure 4.20: The resistor analogy scheme for the thermal path from cell to ambient for air cooling

5

Parameter Estimation & Verification & Validation Approach

This chapter will describe the parameter estimation approach used to configure the EECM models. First, the general parameter estimation procedure will be described in section 5.1. As mentioned in section 5.1 for the parameter estimation approach, a set of experimentally obtained data will be necessary. section 5.2 will show the experiment and determine how this required experimental data set was obtained. At the start of the thesis the required experimental data were not yet available for the specific battery cell used in the Pipistrel battery pack. For this reason, the parameter estimation method was first tested on a different experimental data set of lithium-ion battery cells available at the time. This was done to verify whether the method could work at all before conducting an extensive test campaign. This verification and validation approach is described in more detail in section 5.3

5.1. Parameter Estimation Approach

This section will describe the approach used to estimate the parameters used in the EECMs. The parameters to be estimated are the entries in the lookup tables for various SoCs and temperatures. Look-up tables will be generated for the open circuit voltage (V_{oc}), the values of the resistors (R_0, R_1 and R_2) and the value of the time constants (τ_1 and τ_2).

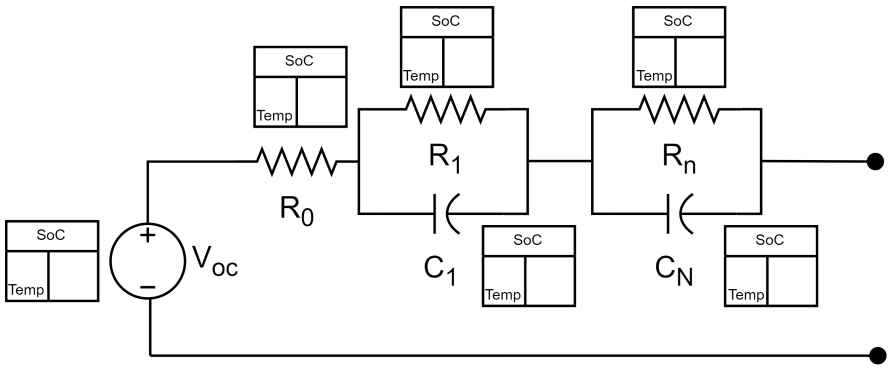

Figure 5.1: A diagram of the EECM model and the corresponding look-up tables

5.1.1. Estimation Procedure

The typical procedure for estimating model parameters is to have a set of experimentally obtained data and then to tweak the model parameters in such a way that the best possible fit between the model output and the experimental data is obtained. The best possible fit is usually obtained with some sort of regression. This problem is therefore, in essence, an optimization problem (curve fit) where the objective function is to minimize the sum-squared error between the model output and the experimental data. For this thesis, the

Simulink parameter estimator tool was used. This tool tries to minimize the objective function F(x) with x the vector of all the parameters to be estimated, as seen in Equation 5.2 where the error is defined as in Equation 5.1[53], with the output of the model (voltage), comparing it to the measurement voltage. The algorithm used to minimize this objective function non-linear least squares (lsqnonlin) with the trust-region reflective algorithm. The objective function was implemented into the MATLAB environment. For the documentation and detailed description of this algorithm, please refer to [52]

$$e(x,t) = y_{exp}(x,t) - y_{sim}(x,t) \tag{5.1}$$

$$F(x,t) = \Sigma_{t=0}^{t_N} e(x,t) \times e(x,t) \tag{5.2}$$

The type of experimental data required for the EECM parameter estimation is a pulsed current characterization test (PCCT). A typical pulsed current characterization test consists of current pulses of fixed duration and C rate ([35], [57]). The fixed duration and C-rate allow the voltage response to be measured at a specific SoC. An example of such a pulsed current profile and the corresponding voltage response can be seen in Figure 5.2. The experimental test setup and test procedure to obtain such a data set will be explained in section 5.2. The goal of parameter estimation is to adjust the parameters in the lookup tables of each EECM component in such a way that the simulated voltage matches the measured voltage as closely as possible. The look-up tables of the EECM components will have 2 dimensions, namely SoC and temperature. The length of the SoC steps have an influence on the combination of pulse duration and C rate. The SoC must have decreased by a certain percentage after each pulse. This means that each pulse must draw a certain amount of charge from the battery cell. This means that a higher C-rate pulse will have a shorter duration than a lower C-rate pulse. It is important that the C-rate of the pulse is chosen such that it is close to a typical C-rate experienced during normal operation of the battery cell.

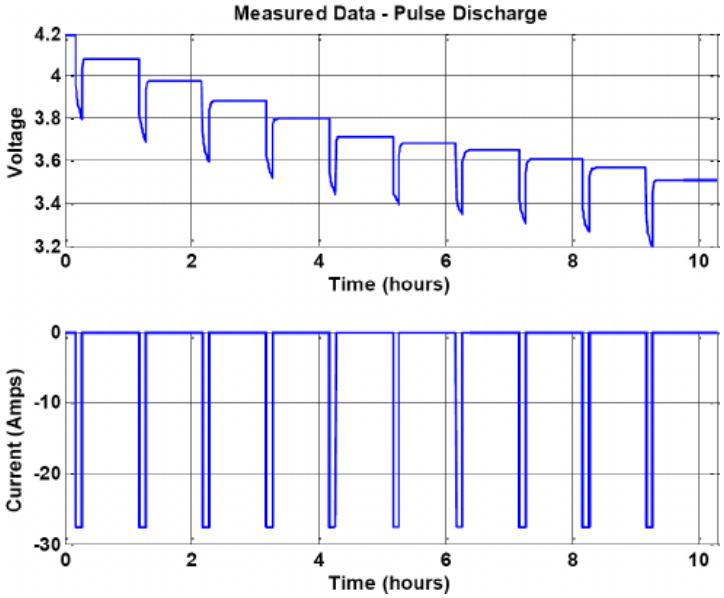

Figure 5.2: Pulse Discharge in 10% increments of SoC [35]

Figure 5.2 shows the pulse current test for pulses of equally spaced SoC breakpoints of 0.1 SoC. The decision can be made to have unequal SoC breakpoints. This decision can be made to add more SoC breakpoints in regions where the voltage behavior is expected to be irregular, such as at low and high levels of SoC. In this way, more data points are available at high and low SoCs to better characterize these regions where voltage behavior is unpredictable [35]. Note that increasing the number of SoC breakpoints increases the number of parameters in the component look-up tables. This increases the amount of parameters to be estimated and, therefore, the time needed for the parameter estimation. The number of temperature break points has the same effect on the number of parameters in the component lookup tables as the SoC. However, as will be described in section 5.2, each pulse current test is performed at a fixed temperature level, so for each temperature break point a separate parameter estimation will need to be performed. The results of these separate

parameter estimations can then be merged to create one large look-up table. The amount of RC-pairs also influences the total amount of parameters to be estimated, as more RC-pairs means more EECM components and thus more look-up tables. As an example of the influence of the amount of SoC and temperature breakpoints and the number of RC pairs on the total amount of parameters Table 5.1 is provided.

Table 5.1: Number of RC-pairs and SoC points combinations with resulting number of parameters

RC-Branches	EECM Components	SoC Break Points	Total parameters
0	V_{oc}, R_0	10	20
1	V_{oc}, R_0, R_1, τ_1	10	40
1	V_{oc}, R_0, R_1, τ_1	15	60
2	$V_{oc}, R_0, R_1, \tau_1, R_2, \tau_2$	10	60
2	$V_{oc}, R_0, R_1, \tau_1, R_2, \tau_2$	15	90
3	$V_{oc}, R_0, R_1, \tau_1, R_2, \tau_2, R_3, \tau_3$	15	120

In Table 5.1 it can be seen that with increasing RC pairs and more SoC break points, the number of parameters rapidly increases. With more parameters, the complexity of the parameter estimation increases, and it would be unreasonable to attempt a single estimation of all parameters at once. For this reason, it was chosen to divide the parameter estimation into smaller parts using a layered approach procedure that is similar to the one presented in [35].
The parameter estimation will be implemented in Matlab using the Simulink Parameter Estimator application [51]. As stated above, this tool works by performing a non-linear least squares regression using the reflective algorithm of the trust region [52]. This is a gradient-based optimization algorithm that means that for each parameter that needs to be estimated, the model must run twice per iteration of the algorithm [35]. The optimization settings used during the estimation can be seen in Table 5.2, along with the limits and initial values of each parameter in Table 5.2. Note that not all parameters were used in the parameter estimation of each type of model. The difference in the upper and lower bounds for the time constants (τ) is to be able to split up the faster and slower physical phenomena in the voltage response. As described in section 4.2, there are slower and faster physical phenomena such as the instantaneous voltage drop and the voltage diffusion. If no bounds are placed on the time constants, the optimizer can use any of the three RC pairs to model a certain voltage effect. By placing the bounds like this it ensures that the fast responses are modeled by RC1, the slower ones by RC2, and if three RC pairs are used, the slowest processes are modelled by RC3.

Table 5.2: Parameter Estimator Optimizer Settings

Parameter	Lower Bound	Upper Bound	Initial Value
V_{oc}	2	4.8	linspace(3,4.4)
R_0	1e-3	1	40e-3
R_1	1e-3	1	10e-3
R_2	1e-3	1	5e-3
R_3	1e-3	1	5e-3
τ_1	0.5	100	5
τ_2	100	250	100
τ_2	100	250	100

The optimizer used to estimate the parameters is gradient-based. As stated above, adding more SoC breakpoints and more RC branches increased the number of parameters. More parameters mean more needed function evaluations, thus a longer estimation time. When estimating all parameters at once, the solver will have to perform function evaluations exercising parameters for parts of the experimental data that they do not influence. For example, the RC parameters at 0.3 SOC should not influence the voltage response at 0.6 SoC. For this reason, it can be beneficial to split the parameter estimation into smaller parts, as is done in [35], and thus reduce the number of free parameters during each smaller parameter estimation. In addition to reducing the amount of free parameters with this method, the length of the experimental data set is also reduced. A PCCT can contain data with a duration of several hours at a sampling rate of up to 10 Hz. If the data set were not split up into smaller parts, a single-model evaluation would take significantly longer since it needs to simulate a lot of unnecessary timesteps, which in turn would greatly increase the overall estimation time.

The experimental data will be divided into sections so that the layered approach procedure as described in [35] can be followed. This approach splits the experimental data set along the SoC break points. This allowed the parameter estimator to perform separate estimations at each SoC level by looking at the discharge pulse at that specific SoC level. By looking only at the data from the discharge pulse between two SoC levels, the estimation cost was greatly reduced. This is again due to the reduction in free parameters and the reduction in the length of the measurement data. A crucial consideration for achieving the best parameter fit is that the split data must contain sufficient data to fully exercise all parameters [35]. Some parameters are applied across overlapping regions in the experimental data set. For this reason, the locations of the data splits overlapped so that each estimation task had sufficient data to exercise both free parameters. A schematic of this approach can be seen in Figure 5.3. Do note that in order to populate the look-up tables in the temperature dimensions, the complete parameter estimation should be repeated at all temperature levels. The reduction in parameters to be estimated can be seen in Table 5.3.

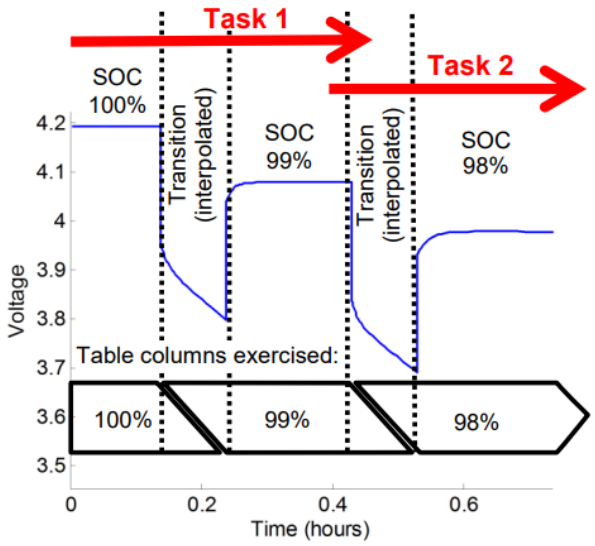

Figure 5.3: A schematic of the layered approach procedure of the parameter estimation [35]

The downside of this method is that, in place of one large estimate, multiple smaller parameter estimations need to be conducted, making the implementation more complex. Care must be taken to ensure that the data set is properly split and that the correct free parameters are used. Also, the resulting estimated parameters must be merged after all smaller estimations have been conducted requiring an extra implementation step.

Table 5.3: Number of RC-pairs and reduced SoC points combinations with resulting number of parameters

RC-Branches	EECM Components	SoC Points Applied	Total parameters
0	V_{oc}, R_0	2	4
1	V_{oc}, R_0, R_1, τ_1	2	8
1	V_{oc}, R_0, R_1, τ_1	2	8
2	$V_{oc}, R_0, R_1, \tau_1, R_2, \tau_2$	2	12
2	$V_{oc}, R_0, R_1, \tau_1, R_2, \tau_2$	2	12
3	$V_{oc}, R_0, R_1, \tau_1, R_2, \tau_2, R_3, \tau_3$	2	16

5.2. Required Experimental Data

In section 5.1 a pulse current characterization test (PCCT) was mentioned. This test is required to perform parameter estimation and configure the EECM model. At the time of this thesis, PCCT data were not available for the specific cells used in the Pipistrel. To obtain this data, a test campaign was conducted with Samsung INR18650-33G cells, as used in the Pipistrel battery pack. This section will expand on that test campaign. In addition to PCCT, several other tests were also performed, such as a continuous charge/discharge test and the test to obtain the data points to determine the entropic coefficients, as stated in subsection 4.2.4. Second, a

description of the test setup used to obtain the test data will be provided in subsection 5.2.2. subsection 5.2.1 will explain the various tests conducted and provide an overview of the order of the tests.

5.2.1. Test Types

In total, four types of tests have been carried out with the Samsung INR18650-33G battery cells. These tests were a break-in test (BIT), a continuous charge/discharge test (CCDT), a pulsed current characterization test (PCCT), and an entropic coefficient test (ECT). In the following sections, each test type will be explained.

Break-In Test

The first test that will be performed on the battery cells is the break-in test. The goal of this test is to cycle the new battery cells a total of 4 times to break these cells in. In the literature it is known that brand new lithium-ion battery cells can show an unpredictable voltage behavior during their first couple of cycles [40]. The goal of this test is therefore to remove the newness of the batteries by cycling them and to get them to work predictably.
The test consists of 4 standard 1C charge and discharge cycles. After each cycle, an ohm test will be performed. The ohm test is a test to measure the internal resistance of batteries [20]. The resulting impedance of this test should be close to the internal resistance as specified on the specsheet [47]. If the ohm test result is close to the specified internal resistance the cell can be considered broken in and ready for testing. If it is not the case, an additional break in cycle might be required.

Continuous charge/discharge test

The goal of the continuous charge/discharge test (CCDT) is to verify if the test setup, which will be described in subsection 5.2.2, is working correctly. During this test, the battery cell is being discharged and charged at a fixed ambient temperature at a rate of 1C. These data are also available in the battery specification sheet as provided by the battery cell manufacturer [47]. For this reason a comparison between the self-obtained test data and the spec sheet data can be made to verify if the measurement data is captured correctly. This test also serves as a shake-down of the test setup. Possible bugs and issues can be worked out when conducting these tests to ensure that the test setup works perfectly during the more important and longer duration PCCT and ECT test.
The test is carried out by charging the battery outside the thermal chamber. After that, the battery cell must then be placed inside a thermal chamber that is set to the desired ambient temperature. The cell must then be left to rest for at least 30 minutes to reach the same temperature as the thermal chamber. When the cell has reached the required temperature, the test can start and the battery cell will be discharged and subsequently charged with a current of 1C. In total 4 CDCT will be conducted at 0, 10, 25 and 45 degrees Celsius.

Pulsed Current Characterization Test

The PCCT is the most important test. This test is used to estimate the parameters of the EECM model. For this test, pulses of 1C of a duration that matches the required SoC step are drawn from the battery. After the current pulse, the battery is left to rest for a certain amount of time to measure the voltage response and see the voltage diffusion. As stated in section 5.1, the SoC break points do not have to be evenly spaced, but more points can be added at the high and low SoC levels to capture the irregular behavior at those levels. For this reason, the decision was made to use steps of 0.05 SoC at SoC >= 0.9 and SoC <= 0.25. At the other SoC levels SoC steps of 0.1 are used. This results in the SoC vector as seen in Equation 5.3. When a pulse of 0.05 SoC or 0.1 SoC is required at a C rate of 1C the pulse needs to have a duration of 3 and 6 minutes, respectively.

$$SoC = \begin{pmatrix} 1 \\ 0.95 \\ 0.9 \\ 0.8 \\ \vdots \\ 0.3 \\ 0.25 \\ 0.2 \\ 0.15 \\ 0.1 \\ 0.05 \\ 0 \end{pmatrix} \tag{5.3}$$

For this test, the battery was charged again outside the thermal chamber. Mean while the thermal chamber is set at the desired temperature level. Once the battery is fully charged, it is placed inside the thermal chamber and left to rest until the battery temperature reaches the desired temperature. Once the desired temperature is reached, the test can begin, and the pulsed current profile can be drawn from the battery cell. This test procedure is repeated again at the 4 temperature levels of 0, 10, 25 and 45 $^{\circ}C$ to create the required data set at multiple temperature levels.

Entropic Coefficient Test

The entropic coefficient test (ECT) is used to determine the entropic coefficients as described in subsubsection 4.2.4.2. This section will explain how to obtain the necessary data points to perform the described linear regression.
The battery cell will be fully charged outside the thermal chamber. The thermal chamber will be set to the desired temperature level. The cell is now placed inside the thermal chamber for at least 30 minutes to reach the desired temperature level. The voltage is now recorded manually. The temperature setting of the thermal chamber is now changed to the next temperature level, and again the cell is left to rest until it reaches the desired temperature. (Temperature levels are 0, 10, 25 and 45 $^{\circ}C$). Once all 4 temperature levels are recorded, the battery is discharged by a fixed SoC percentage, and the procedure is repeated. This results in 4 data points per SoC level. These 4 data points can then be used to perform the linear regression mentioned in subsubsection 4.2.4.2

5.2.2. Test Setup

This section will describe the test setup used to perform the four test types described in subsection 5.2.1. This test setup uses five pieces of equipment that are needed. These have the following function; a means of drawing a specified current from the battery, a way to record the voltage, a way to record the temperature of the cell, a way to keep the chamber temperature constant, and a way to control the setup. Each component will be described in this section. The complete setup can be seen in Figure 5.4 and Figure 5.5.

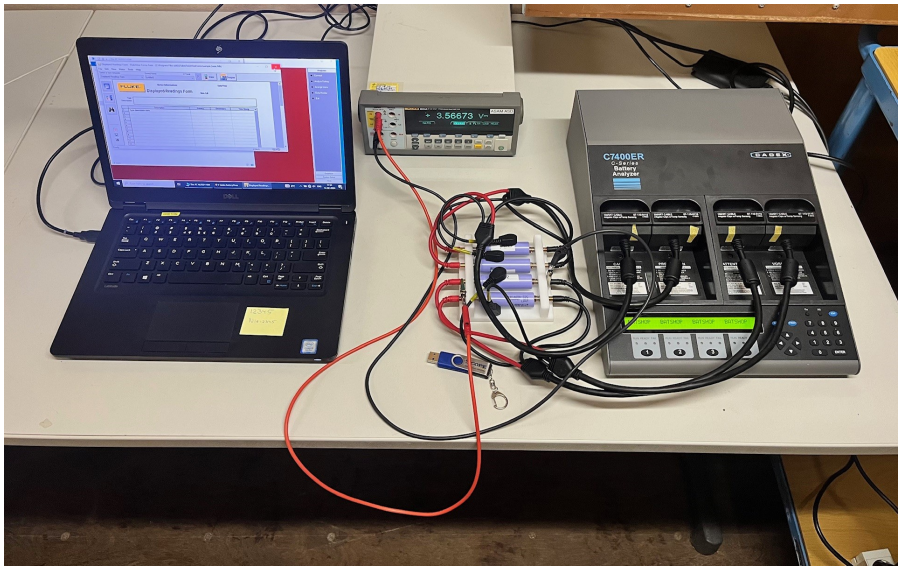

Figure 5.4: The test setup used to test the INR18650-33G battery cells

As stated above, a means to draw a current from the battery cell was required. As a current source, a CADEX 7400ER Battery Analyzer was used. The CADEX can be seen in Figure 5.4 as the large gray/black box on the right side of the picture. In addition to drawing a set current from the battery cell, this analyzer also came equipped with a temperature sensor with a resolution of 1 degree Celsius [20]. This allows the battery analyzer to be used to draw current and record cell temperature. The CADEX also has a means of logging voltage data, but since the minimum sample rate for this device was one sample per minute, it was deemed too low to get an accurate reading of the dynamic voltage response. For the current measurements, this low sample rate was not an issue, since the current profile was prescribed and therefor already known. For the temperature measurements, the low sample rate was also less of a problem since the thermal dynamics is much slower

than the voltage dynamics. In addition to this, the aim of the test is to keep the cell temperature constant during the test, so little variation is expected anyway. The CADEX was controlled through a serial connection to the laptop on which the current and temperature data were logged using the CADEX Batshop software.
The voltage response of the battery cell was recorded using a Fluke 8845A multimeter using the FLuke View software. The multimeter can be seen as the light gray box on the top of the center of Figure 5.4. The multimeter was set to log at least once every second or when a change in voltage at a minimum threshold of 0.0001 Volts was detected. The sample rate of the multimeter was 100 ms, but the Fluke View software did not record these measurements separately but recorded them as events of a certain duration. An event contained multiple measurement points, and the logging software recorded the duration, the maximum, minimum, and average voltage of the measurements contained in that event. When testing the multimeter, it was found that with these settings, a sample rate of at least 1 event per 0.5 seconds can be achieved. This sample rate is considered sufficient for recording the voltage dynamics of the battery.
In order to keep the cell temperature constant during a test, the cell is placed inside a thermal chamber to keep both the chamber temperature and the cell temperature constant. The constant temperature allows the pulsed current test to be performed at various temperature levels, creating measurement data at these different temperature levels. The parameter estimation can then be done multiple times at the different temperature levels to populate the look-up table in its second dimension which was the temperature. The thermal chamber that was used during the test campaign on the Samsung cells was old. This chamber had the disadvantage that there was no access port into the chamber to place the battery connection wires on the battery, as can be seen in Figure 5.5. For this reason, the wires needed to go underneath the door, which meant that the chamber was not completely airtight sealed. Some air outside the chamber could leak into the chamber and vice versa. However, since the chamber air volume is much larger than the volume of the cell, this leakage would be assumed to be negligible. Also, since the chamber is much larger than the cell volume and the temperature control is only done on the temperature chamber air, the cell temperature might vary due to it heating itself up during the test where the ambient temperature is kept constant by the thermal chamber. It is important to analyze how much the actual cell temperature varied during the constant ambient temperature test to be able to draw any meaningful conclusions from it.

Figure 5.5: The battery holder used in the test setup placed inside the thermal chamber

5.2.3. Test Order

Not all tests are performed on all battery cells. Every cell was subjected to a BIT but after that only a CDCT, PCCT or ECT was performed. This was done for two reasons. Number one is that this would take too much time to perform all tests multiple times. The second reason being that this eliminates the effect of battery aging between tests. This is done by ensuring that every cell has had the same amount of charge-discharge cycle before each test. Every CDCT, PCCT, ECT is conducted right after the 4 cycle BIT, and therefore the age of every battery cell is the same age at the start of every test. If this had not been done and, for example, one cell would be used for all tests by the time the ECT would need to be conducted, the battery cell would have had 8 additional cycles which could already cause cycle aging in the battery. By keeping the cycle count at the start of every test constant and using a different cell for each test, this variable behavior is eliminated. The specific type of test performed on each cell can be seen in Table 5.4. Note that cells 10 to 12 are used as

backup cells, so no tests will be performed on these cells apart from the BIT. The results of all experimental tests can be found in section 6.2.

Table 5.4: Cell numbers with corresponding tests performed on cell

Cell nr.	BIT	CDCT	PCCT	ECT
1	x	0 [degC]	-	-
2	x	10 [degC]	-	-
3	x	25 [degC]	-	-
4	x	45 [degC]	-	-
5	x	-	0 [degC]	-
6	x	-	10 [degC]	-
7	x	-	25 [degC]	-
8	x	-	45 [degC]	-
9	x	-	-	x
10	x	-	-	-
11	x	-	-	-
112	x	-	-	-

5.3. Verification & Validation Approach

This section will describe the verification and validation approach used in this thesis. First, it will explain why a separate pulsed current characterization data set was used to first verify if the parameter estimation could be used for this thesis. It will also explain how the parameter estimation was validated using a drive-cycle test. All this will be explained in subsection 5.3.1. Second, a description on how actual flight test data from test flights with the Pipistrel Velis Electro could be used to verify and validate the electrical and thermal model. This will be provided in subsection 5.3.2.

5.3.1. Verification & Validation Parameter Estimation

At the beginning of this thesis, no pulse current characterization data were available for the specific battery cell used in Velis Electro. Through the NLR the possibility was offered to perform the tests in-house and so gather the required experimental data. However, this would pose quite an extensive and long test campaign. For this reason, it had to be ensured that before an extensive test campaign was started, the EECM model with a parameter estimation performed on PCCT data would provide proper results. To validate EECM parameter estimation on PCCT data, it was first tested on a similar publicly available lithium-ion battery cell dataset by Kollmeyer [39]. This data set includes various discharge tests, CDCT and PCCT tests, and several current profiles of the drive cycle, such as the Urban Dynamometer Driving Schedule (UDDS)[22]. The PCCT test was used as the data set to perform the parameter estimation. The results of the estimation can be verified with the CDCT test. The UDDS drive cycle test can further validate the parameter estimation. All tests were carried out in a similar setup to subsection 5.2.2. The results of the verification of the parameter estimation can be seen in subsection 6.3.2.

5.3.2. Verification & Validation Flight Test Data

The specificity of this thesis in relation to the Pipistrel Velis Electro use case is primarily due to the possession of such an aircraft by the NLR, thus providing an abundance of flight test data for verification and validation objectives. The aircraft is equipped with numerous sensors, both onboard and within the battery pack, all of which are meticulously logged by the battery management system. Therefore, for the validation of the parameter estimation of the Samsung battery cell no UDDS was available but instead the actual flight test data will be used. This subsection is dedicated to explaining the logged data and the manner in which they can be used for verification and validation. Initially, test data relevant to the validation of the electrical model will be introduced, followed by the presentation of data relevant to the validation of the thermal model.

The battery management system (BMS) aboard the Velis logs several electrical parameters. The parameters of interest for validation of the electrical model are battery SoC, SoH, current, and voltage. The battery management system (BMS) also logs the data of individual battery cells. The BMS stores the voltage for each individual cell. The current through each cell can be found by dividing the total current of the battery pack by

the number of parallel cells. Utilizing the current and voltage data of the individual battery cells the electrical model can be validated for a specific test flight.
The Battery Management System (BMS) is equipped with the capability to monitor the temperature of 20 cells within the battery pack. Regrettably, the precise positioning of the thermocouples, which are instrumental in these temperature measurements, remains undetermined, thus precluding the possibility of distinguishing temperature variations at different locations within the battery pack. Moreover, the internal temperature sensor of the battery pack exhibits a resolution of a single degree. This level of granularity is somewhat crude. Consequently, the utility of this temperature data for the validation of the thermal model is confined to the observation of trends and maximum temperatures. In addition to individual cell temperatures, the BMS also provides data on the minimum, maximum, and average cell temperature recorded within the battery pack. The data corresponding to each of the two battery packs is recorded independently. The results of the verification and validation can be found in section 6.4

6

Results & Discussion

This chapter will present the results obtained following the modeling methodologies described in chapter 4 and the parameter estimation and validation approach described in chapter 5. First, the results of the verification of the parameter estimation method performed on the Panasonic data set provided by Kollmeyer [39] are presented in section 6.1. This will be followed by the presentation the experimental results obtained during the test campaign performed on the Samsung INR18650-33G cell as described in section 5.2. The parameter estimation method was applied to the experimental data obtained to estimate the EECM parameters for the Samsung INR18650-33G battery cell. The results of this parameter estimation and the verification and validation (with component test data and flight data) will be presented in section 6.3. With the electrical model validated, integration with the thermal model could be performed and validated using flight data. This is presented in section 6.4. In the same section, a comparison is made between various battery thermal management strategies. Furthermore, a sensitivity analysis of the model parameters of each of the battery thermal management systems is presented in section 6.4. To investigate the effect of increasing the nodal resolution of the lumped parameter nodal thermal network model on the accuracy and complexity of the model, a nodal convergence analysis was performed in section 6.5. An investigation of the thermal behavior of the battery pack operating during cold weather and charging conditions is provided in section 6.6. Finally, the chapter will conclude with a scale-up of the use case from a general aviation aircraft to a small electric turboprop to see how and if this model can be scaled to be applicable to a use case which has a higher power and energy requirement. This will be presented section 6.7.

6.1. Panasonic NCR1850PF Battery Cell: EECM Parameter Estimation & Validation : Example for Method Verification

This section will show how the Panasonic NCR 18650PF battery cell data set provided in [39] was used to verify whether the parameter estimation method using nonlinear regression as described in ([35], [57]) could be used. The resulting estimated parameters for a 2RC EECM will be provided in subsection 6.1.1. Subsequently, the accurate estimation of these parameters will be validated using continuous discharge current and drive cycle current data. This will be presented in subsection 6.1.2 and subsection 6.1.3, respectively.

6.1.1. Parameter Estimation

This section will present the results of the parameter estimation applied to the publicly available Panasonic data set [39]., The data set used to perform the parameter estimation was a hybrid pulsed current characterization (HPCC) test. As an example, the HPPC current profile and the measured voltage response at 0 $^{\circ}C$ are provided in Figure 6.1.

Figure 6.2 shows the resulting parameters following the parameter estimation procedure applied to the HPPC data set for a 2RC EECM model. It can be seen that for SoC higher than 0.15 the resistance values are roughly constant and show similar resistance values. When the SoC decreases to values below 0.15 a sharp increase in the resistance values is seen. This sharp increase in resistance has two reasons. The first being that at very low SoC the voltage behavior of the lithium ion battery cell becomes highly non-linear, as seen in Figure 4.2. The EECM struggles to accurately represent this pronounced nonlinearity at lower SoC levels, particularly given the sizable SoC increments of 0.05 SoC employed during this parameter estimation at these specific

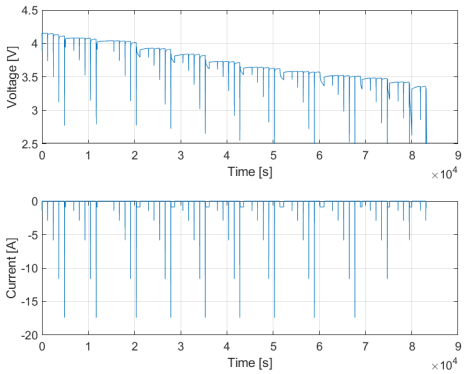

Figure 6.1: The current profile and measured voltage response of the HPPC test at 0 degrees Celsis

SoC levels. The precision of the estimation could have been improved by employing smaller SoC increments at lower SoC levels. However, given that the data set originated from an external source, this approach was not feasible.
The spike in resistance at low temperature and low SoC is due to the effect of temperature on battery charge. Lower temperatures limit the charge that can be drawn before hitting the cut-off voltage [89]. The SoC, determined by Equation 4.2, cannot reach zero if the typical capacity is not adjusted, as the cut-off voltage is reached first. When this happens, the PCCT stops, leaving no data for parameter estimation at low temperatures and SoC levels. Hence, resistance remains at the initial conditions and no parameter estimation occurs. The model may be inaccurate under these conditions, as subsection 6.1.3 shows. However, in the use case of this thesis, such conditions are rare. The pilot operating handbook [68] states that the lowest acceptable SoC level during nominal operations is 0.3, and it is unlikely that it drops below 0.2, even in emergencies. Batteries are pre-conditioned to optimal temperature before flights, and flights at temperatures below 0 $^{\circ}C$ are not allowed, as stated by the Pilot Operating Handbook (POH) [68]. Thus, a low SoC and temperature is an extreme edge case and will almost never occur.

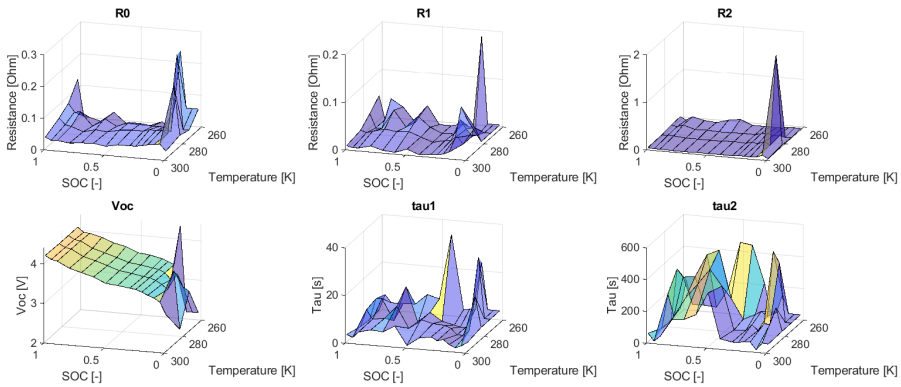

Figure 6.2: The resulting parameters of a 2RC EECM of the parameter estimation on the Panasonic data set

6.1.2. Validation Using Continuous Discharge Current

The figures Figure 6.3 and Figure 6.4 present a comparison between the manufacturer's specification data and the simulated voltage at 0 and 25 $^{\circ}C$. These two figures verify the observation that the EECM model's accuracy diminishes at lower temperatures and lower SoC levels. It can be observed from both figures that the discrepancy between the measurements and the simulation stays relatively constant but begins to escalate as the discharge capacity approaches the nominal battery capacity, indicative of a low SoC being achieved.
From the figures it can also be observed that the average residual error is larger in the simulation at 0 than at 25 $^{\circ}C$. This verifies the observation made in subsection 6.1.1 that the EECM model becomes less accurate under lower temperature conditions, especially at high discharge capacity (low SoC). This can be attributed

to the fact that lithium ion batteries behave more unpredictably and non-linearly, as seen in the figures.

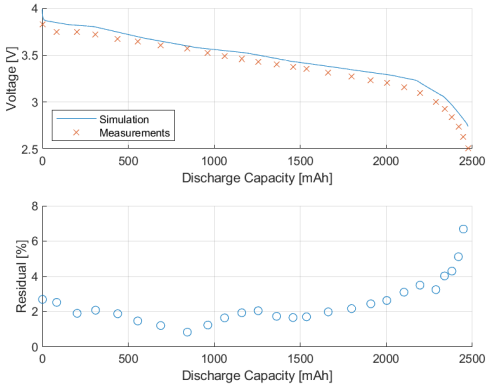

Figure 6.3: A comparison between the specification data [62] and the simulation at a current of 1C at 0 °C

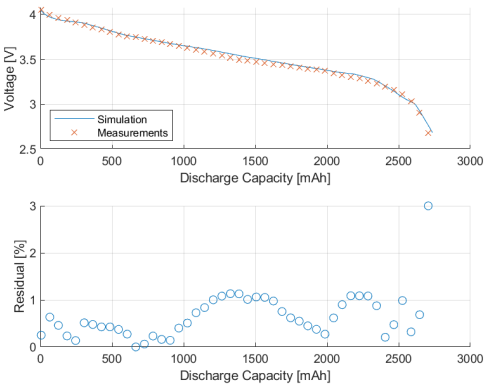

Figure 6.4: A comparison between the specification data [62] and the simulation at a current of 1C at 25 °C

6.1.3. Validation Using Drive Cycle Data

As described in subsection 5.3.1, the parameter estimation procedure can be validated by simulating a current profile that has not been used to estimate the parameters and comparing the simulated voltage with the measured voltage. For this validation, the Urban Dynamic Driving Schedule (UDDS) current profile was used. This current profile can be seen in Figure 6.5.

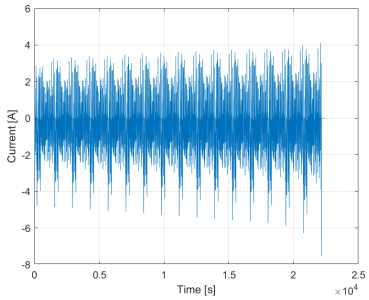

Figure 6.5: The UDDS Current Profile

Figure 6.6 and Figure 6.7 show a comparison between the measured and simulated voltage for the UDDS driving cycle. From both figures it can be observed that the results match very well. For the 25 °C simulation, the maximum error remains below 6% with an RMSE of 0.08056 % and for the 0 °C simulation it remains below a maximum error of 10% and an RMSE of 0.9478%. However, these maximum errors are obtained at very late simulation times and can again be attributed to the EECM losing accuracy at low SoC levels. When looking only at the higher SoC (so earlier in the simulation) the maximum error remains well below 4% and 2% for the 0 and 25 °C case, respectively.

Figure 6.8 and Figure 6.9 illustrate the correlation between the simulated SoC and the actual measured SoC for the UDDS drive cycle at 0 and 25 °C, respectively. Note again that the discrepancy between the simulated and experimental SoCs is minimal. However, it is noticeable that the error margin increases as the simulation continues. This tendency may be related to the method of determining the SoC in the EECM model. The approach adopted to determine the SoC in the EECM model is the straightforward Coulomb counting method, as referenced in section 4.2. This method, while extremely simple, accumulates error over time due to the noise in current measurements[16]. More advanced techniques for estimating the SoC, such as the application of extended Kalman filters as in [16], could improve the accuracy of the SoC estimation. However, in this thesis, it was decided against this approach since even the maximum cumulative error is significantly less than 5%, making the addition of this additional layer of complexity in the form of an improved SoC estimation algorithm unnecessary.

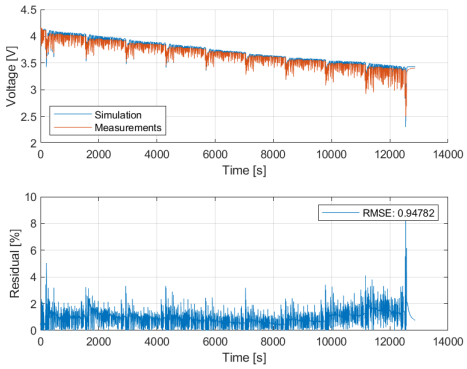

Figure 6.6: A comparison between the experiment data [39] and the simulation at a UDDS profile at 0 °C

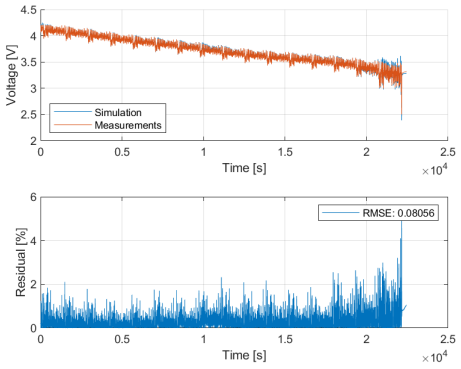

Figure 6.7: A comparison between the experiment data [39] and the simulation at a UDDS profile at 25 °C

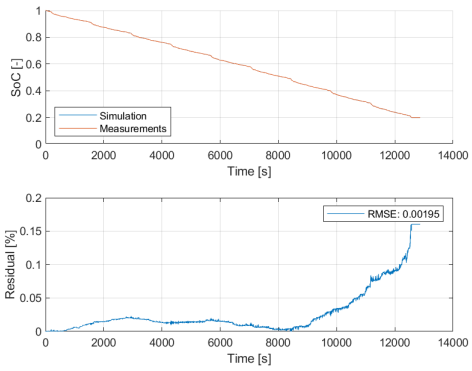

Figure 6.8: A comparison between the experiment data [39] and the simulated SoC on a UDDS profile at 0 °C

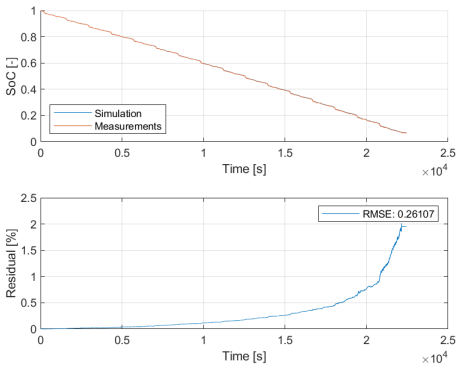

Figure 6.9: A comparison between the experiment data [39] and the simulated SoC on a UDDS profile at 25°C

The EECM approach, when integrated with the proposed parameter estimation method, has been found to accurately simulate the voltage behavior of a lithium-ion battery cell, as evidenced by Figure 6.6, Figure 6.7, Figure 6.8 and Figure 6.9. Consequently, an experimental campaign was initiated to collect the necessary data from the Samsung INR18650-33G cell, which is utilized in the Pipistrel battery pack. The findings from this experimental campaign will be disclosed in section 6.2.

6.2. Experimental Campaign with Samsung INR18650-33G Cell

This section will show the experimental data collected during the test campaign as described in section 5.2. First, the results of the continuous charge / discharge current test will be presented in subsection 6.2.1. Second, the resulting pulsed current characterization test data will be presented in subsection 6.2.2. This will be followed by the results of the entropic coefficient test shown in subsection 6.2.3.

6.2.1. Continuous Charge/Discharge Current Test

This section will show the results of the continuous charge/discharge current test (CDCT). The results can be seen in Figure 6.10. In the figure two clear trends can be seen in the discharge plot. The first is that the voltage decreases with decreasing temperature. This is similar to what was shown in [89]. The second trend that can be observed is that the amount of charge available is less when the temperature is lower. For the continuous discharge test, the battery cell was discharged until the cut-off voltage of 2.5 Volts was reached, and in the figure it can be seen that this is at a lower discharge capacity for 0 °C than for 45 °C.

In Figure 6.10, a clear trend can also be seen in the charge plot. For the charging of the batteries, the CC-CV charge method was applied. This means that the current was kept constant at 1C until the maximum charging voltage of 4.2 Volts was reached. At that point the current was decreased to keep the voltage at 4.2 Volts until no more charge could be put into the battery. In the figure it can be seen that the lower the temperature, the

earlier this CV cross-over point of 4.2 Volts was reached. This again means that the lower the temperature, the less charge the battery is able to hold.

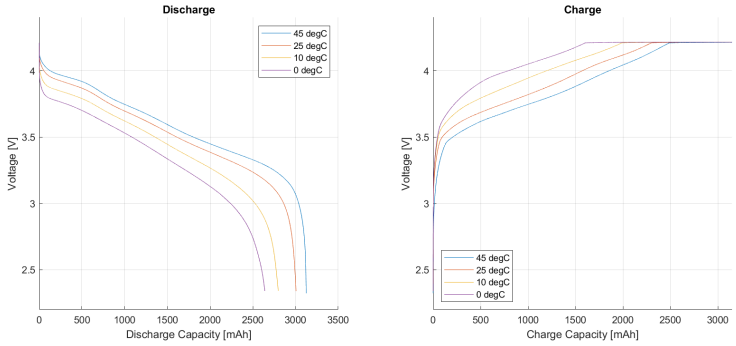

Figure 6.10: The results of the continuous charge and discharge current tests of 1C at various temperature levels of the Samsung INR18650-33G battery cell

6.2.2. Pulsed Current Characterization Test

This section will show the result of the Pulsed Current Characterization Test (PCCT). This test was performed at 0, 10, 25 and 45 $^{\circ}C$. Only the results for the 25 $^{\circ}C$ tests will be shown in this section to keep the section concise. The results for the other three temperatures can be found in section A.2.

The PCCT outcomes at 25 $^{\circ}C$ are shown in Figure 6.11. A noticeable distinction between Figure 6.11 and Figure 6.1 is that in the PCCT a consistent C rate was maintained for all current pulses, while the Panasonic data set utilized multiple current pulses at varying C rates. The choice of maintaining a single C rate in the PCCT was made to exclude the influence of different C rates on the parameter estimation. Given that an aircraft is operating predominantly in cruise conditions with a stable power setting, the C rate does not fluctuate much during a typical mission. A higher C rate is expected only during take-off, which is a brief segment of the aircraft's mission. Hence, the decision was taken to perform the parameter estimation using a PCCT with 1C pulses. If the C rate is found to have significant variations during a typical mission, the EECM model can be enhanced by transitioning from a 2D to a 3D lookup table, factoring in SoC, temperature and C rate. To be able to populate a 3D look up label additional experimental data would be required in the form of PCCT with different C rate pulses at various temperature levels significantly increasing the length of the experimental campaign.

In Figure 6.11, it can also be seen that the cell temperature during the test was not precisely constant at 25 $^{\circ}C$. This can be explained by the fact that during the test the chamber temperature was controlled and set at 25 $^{\circ}C$. However, the volume of the air chamber is much larger than that of the cell. During PCCT, current pulses cause the cell to generate heat. This heat generation causes the cell to heat up, but it is not enough heat to significantly warm up the air in the temperature chamber. Since the air in the temperature chamber is not significantly affected, the chamber does not increase its cooling power, and the cell is not cooled enough to prevent it from heating up. The cell temperature difference during the test is only 2 $^{\circ}C$ as seen in the figure so the effect this temperature difference has on the precision of parameter estimation is expected to be limited. However, without a data set in which this temperature difference is not present, this assumption cannot be validated. For this reason, it is recommended that for any future PCCT, a different way of temperature control is used. This would preferably be a way that controls (cools) the cell temperature directly, for example submerged cooling, and not indirectly as was done in this thesis work by controlling the chamber temperature.

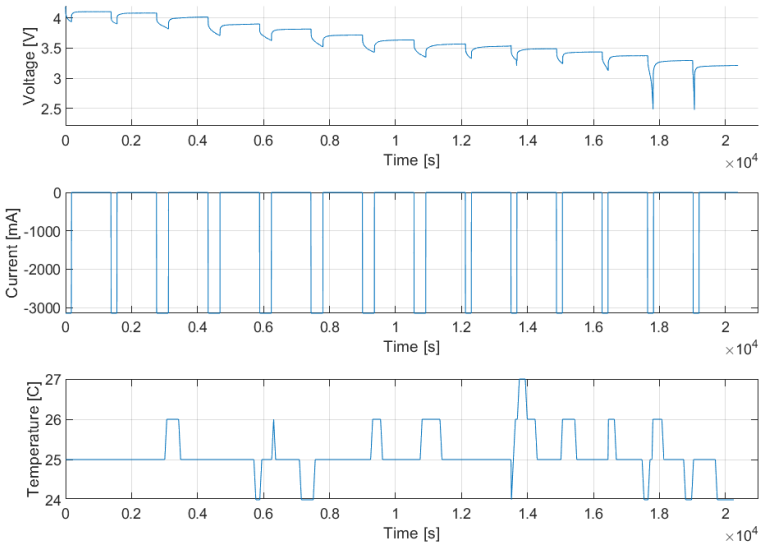

Figure 6.11: The results of the PCCT on the Samsung INR18650-33G Cell at 25 °C

6.2.3. Entropic Coefficients Test

This section will show the results of the entropic coefficient test as described in section 5.2. It will also show a comparison between the two described methods for determining the entropic coefficients. As described in subsection 6.2.3, these two methods were the experimental method and extraction from the PCCT data set as used in [27].

In Figure 6.12 an example plot is provided on how the entropic coefficients were determined by performing linear regression on the ECT measurement points. The figure shows the open-circuit voltage at a SoC of 1 for 4 different temperature levels. By performing a linear regression on these points and determining the slope of this linear line, the entropic coefficient was found. The equation found by linear regression can also be seen as the title of Figure 6.12. This type of regression was performed at all SoC levels listed in Equation 5.3. However, to keep this section compact, only the regression for SoC at 1 is shown. The regression plots of the remaining SoC levels can be found in subsection A.2.2.

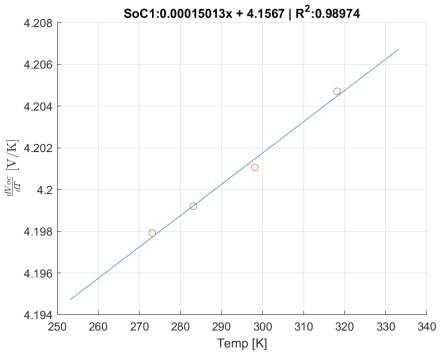

Figure 6.12: An example of an entropic coefficient regression plot at SoC=1 for the voltage measurements

The same linear regression method was applied to the 4 open-circuit voltage values obtained from the PCCT data as was described in subsubsection 4.2.4.2. The regression plots for all SoC levels can be seen in subsection A.2.2. A comparison between the values of the entropic coefficient obtained by the experimental method and the PCCT data method is provided in Figure 6.13. From the figure it can be seen that both methods follow a similar trend and that the PCCT method predicts a less fluctuating entropic coefficient value at all SoC levels.

From Figure 6.13, the results of the ECT test appear erratic. This is likely due to insufficient rest periods after

discharge. Ideally, the cell should rest for hours to reach electrical equilibrium and the prescribed temperature. However, time constraints limited the rest period to 20 minutes per discharge pulse, preventing the cell from reaching equilibrium and causing ongoing voltage diffusion. This diffusion, particularly noticeable immediately after discharge at 0 $^{\circ}C$, decreased by the time of the measurement at 45 $^{\circ}C$. Given the entropic coefficient's millivolt order, this voltage diffusion significantly affected the readings, potentially leading to inaccuracies. For this reason, the decision was made to use the PCCT entropic coefficients in the thermal model as they produced a more steady entropic coefficient and in [27] accurate results were produced using this method. As a recommendation for a future investigation, more time should be taken to accurately perform the ECT by having a longer rest time after each discharge pulse.

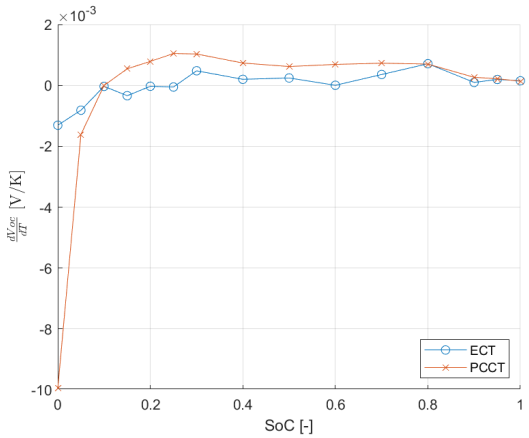

Figure 6.13: A comparison plot between the entropic coefficients obtained experimentally and with the PCCT method

6.3. Samsung INR18650-33G Battery Cell: EECM Parameter Estimation & Validation

This section will show the results of the parameter estimation procedure applied to the experimental data obtained as presented in section 6.2. subsection 6.3.1 will show the estimated parameters obtained after the estimation procedure. These parameters will be verified using continuous current data in subsection 6.3.2. For the validation of the EECM model of the Samsung INR1865033G battery cell, no UDDS data was available; instead the logged voltage data of an actual flight test will be used to validate the EECM. This validation of estimated parameters using actual flight test data will be provided in subsection 6.3.3.

6.3.1. Parameter Estimation

In Figure 6.14 the results of the parameter estimation on the experimental data obtained for a 3RC EECM model can be seen. The estimation procedure was also applied for 0-, 1-, 2RC models. These parameter plots can be seen in subsection A.2.3. From Figure 6.14 the same trends can be observed as described in subsection 6.1.1. The resistance values remain roughly constant but begin to increase as temperature and SoC decrease, causing a spike in the estimated resistance values. The reason for this has already been explained in subsection 6.1.1 and could be attributed to the absence of experimental data to estimated the parameters on at low SoC and temperature and the increase of internal resistance of lithium ion batteries at low SoC and temperature.

The resistance values found are also less erratic than seen in Figure 6.2. This has two reasons. The first reason being that for this PCCT only pulses of 1C were used, whereas the Panasonic data set had multiple pulses of various C rates for each SoC level. Pulses with different C rates cause a difference in the measured voltage responses and therefore affect parameter estimation. Since the PCCT uses only pulses of 1C, the effect of different C rate pulses is eliminated. For future work, this effect could be included by performing PCCT at different C rate pulses and transitioning from a 2D to a 3D look-up table based on SoC, temperature, and C rate.

The second reason for the more smooth looking surface plots for the resistances values is that the data set was obtained in-house. Since the data set was obtained in-house, more data points were available at more

combinations of SoC and temperature levels. As explained in subsection 6.1.1, under lower SoC and lower temperature conditions, the cut-off voltage would be reached at an SoC that is not zero. In the PCCT test conducted in the experimental campaign, this occurred at a later stage than with the publicly available Panasonic data set. This allowed more parameters in the form of look-up table entries to be estimated as data for these entries was available. This left the parameter values not just equal to their initial guess value. This will expand the applicability window of this EECM model as the actual EECM circuit parameters are now estimated at a wider SoC and temperature range, which was not the case for the Panasonic data set. Better performance of the EECM model is now expected at low SoC and temperature, but it must be verified and validated in subsection 6.3.2 and subsection 6.3.3.

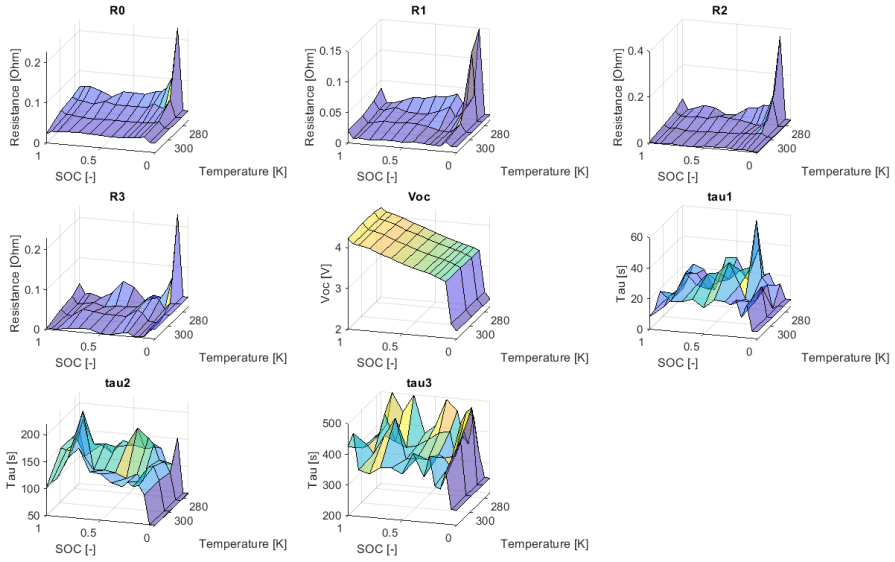

Figure 6.14: The resulting parameters of the parameter estimation procedure for the Samsung INR18650-33G battery cell with a 3RC EECM

6.3.2. Validation using Continuous Discharge Current Data

In Figure 6.15 and Figure 6.16 a comparison between the measured voltage and the simulated voltage at a continuous discharge current of 1 C is plotted for the test 0 and 45 $^{\circ}C$. Similar plots are available for the tests 10 and 25 $^{\circ}C$. These can be found in subsection A.2.4.

Similarly to what was explained in subsection 6.1.2, it is clear that the simulated voltage matches the voltage measured at high SoC levels very well. It starts to deviate from the measurements at low SoC, as can be seen by the increase in the residual value. The reason for this behavior is the same as explained in subsection 6.1.2 and is due to the voltage behaviour of the lithium ion battery becoming highly non-linear at low SoC and the unavailability of data to perform the parameter estimation on at the low SoC entries of the EECM look up tables. From the good match between the simulated and measured voltage in Figure 6.15 and Figure 6.16 it can be verified that the parameter estimation procedure was applied correctly. The EECM can now be validated using actual flight test data as will be done in subsection 6.3.3.

6.3.3. Validation Using Flight Data

The EECM model for the Samsung battery cell can be validated with the use of real flight test data. This data was logged during a flight with the Pipistrel Velis electro aircraft. Many of such data sets are available for different flights. The decision was made to use the flight data set with the longest flight duration, as this would cover the greatest SoC range. The current profile drawn from the battery during the chosen test flight can be seen in Figure 6.17. In the figure a distinct power peak can be observed at around 1000 seconds. This peak is due to the aircraft starting its take-off run and the pilot selecting the take-off power. Afterwards, the power is reduced to the climb power for a short while after which the power level remains roughly constant for a long period of time. This period is the cruise phase of the flight. After the cruise phase at 2100 seconds, the power

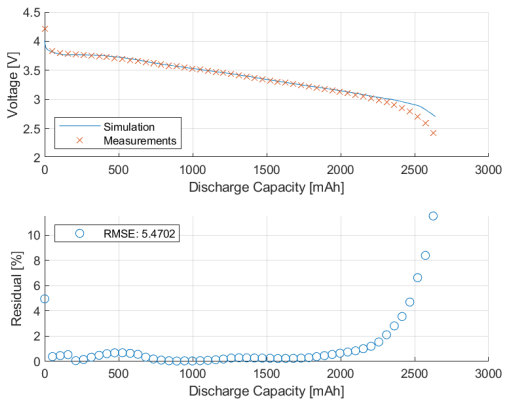

Figure 6.15: A comparison of CDCT data and the simulated voltage at a continuous discharge current of 1C at 0 $^{\circ}C$ using 3RC EECM

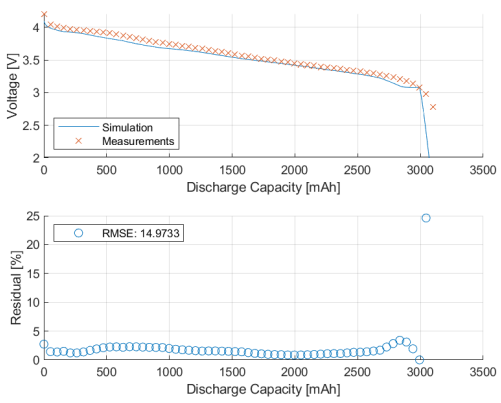

Figure 6.16: A comparison of CDCT data and the simulated voltage at a continuous discharge current of 1C at 45 $^{\circ}C$ using 3RC EECM

is reduced to almost zero to descend down to the runway. After the descent at 2250, 4 new distinct peaks in the current can be observed. This is due to the fact that the aircraft in this flight performed 4 go-arounds and thus had to select max go-around power after the 'failed' landing attempt. This explanation can be confirmed by the logged altitude data as seen in Figure 6.18. In the figure, it can also be noted that the altitude at the start of the data set is negative. This is due to the fact that the flight was conducted at Rotterdam The Hague Airport and this airport is 4.5 meters below sea level. Unlike all previous tests, the battery temperature during this test was not constant. As the goal of this validation is to validate only the electrical model and not yet integrate it with the thermal model, the battery cell temperature for these validations is taken from the flight data and prescribed as input to the model.

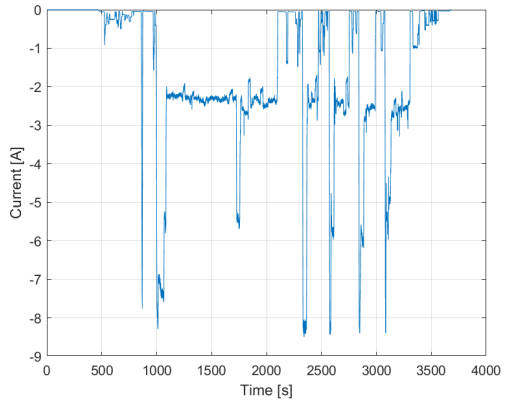

Figure 6.17: The current profile of the chosen test flight

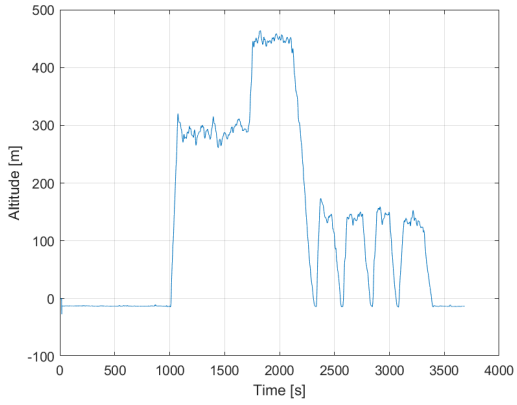

Figure 6.18: The altitude data of the chosen test flight

In Figure 6.19 the comparison between the measured cell voltage and the simulated cell voltage during the described test flight can be seen. From the figure it can again be seen that the match between the measured and simulated voltage is very good with the maximum residual error remaining below 2.5% and the RMSE of 1.5225 %. Overall, all the dynamic voltage responses are captured well by the model as it shows the same dips and jumps in the voltage response at the correct times. Between 1000 and 2100 seconds the simulated and measured voltages are nearly identical. After 2100 seconds the residual error starts to increase slightly. The same voltage jumps can be observed due to the dynamic current however, the EECM seems to over estimate the voltage slightly. This overestimation remains consistent for the remainder of the flight test. The overall residual error is very low, and therefore, it can be concluded that, in terms of voltage modeling, the developed EECM is validated. An additional investigation on the effect of removing RC branches on model accuracy is warranted. This will be provided in subsection 6.3.4.
In Figure 6.20 a comparison is provided between the simulated SoC and the measured SoC. It is interesting to see that when comparing the residual error to that seen with the Panasonic validation plot (Figure 6.8, Fig-

ure 6.9) the residual hovers around a constant value of around 4% and slightly decreases toward the end of the flight test. There are two explanations for this difference in the SoC. The first was described in subsection 6.1.3. The SoC estimation algorithm used by this model was the simple Coulomb counting method. This method is sensitive to noise in the current measurements and therefore accumulates an error over time.
The second explanation for the error between the SoC estimation of the model and the measurements can be attributed to battery aging. This thesis work only considers the effect of battery aging in a very simple manner. As described in subsection 4.2.2, only the effect of battery aging on available battery capacity through the state of health of the battery is considered. It was assumed that the actual battery capacity could be calculated as in Equation 4.15. The assumption that the aged cell capacity is linearly related to the SoH of the battery could be not valid and causing an error. This explains the near-constant offset throughout the test. The effect of battery aging on the open circuit voltage of the battery cell is also not taken into account in this thesis work. Cyclic aging, and therefore SoH, is known to have an effect on battery voltage behavior as shown in [84]. This effect was not noticed when Panasonic cells were validated as these cells were brand new when Kollmeyer [39] started the testing campaign. By the time the battery cells were used to perform the drive cycle test, they had only experienced a few cycles, so the effect of cyclic aging on the battery cells was negligible. However, this was not the case for the battery cells in the Pipistrel battery pack during the test flight. The SoH at the start of this test flight was 0.88 so the battery cells had already experienced quite a number of cycles. However, the exact number of cycles the battery pack had experienced is unknown, as the details on the algorithm the Pipistrel uses to determine the SoH of the battery are unknown. Therefore, a more detailed investigation on the effect of battery aging on electrical performance is recommended. This could possibly be done by including the SoH as a parameter entry into the look-up table and seeing the effect SoH has on the EECM circuit parameters and so transforming the lookup table from 2D to 3D and possibly 4D if the effect of the C rate was also included. However, this would require a significantly more testing time since the battery cells will have to be cycled a great number of times to reach various SoH levels before a PCCT could be applied on them.

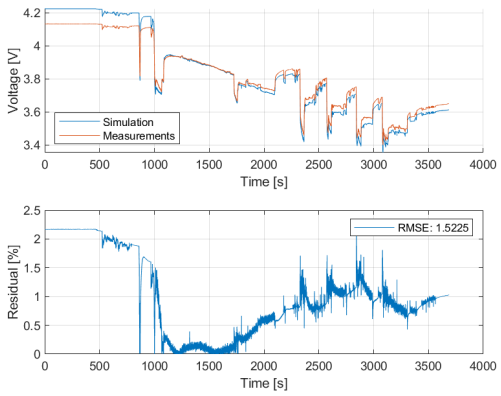

Figure 6.19: A comparison between the flight test cell voltage data and the simulated voltage using a 3RC model

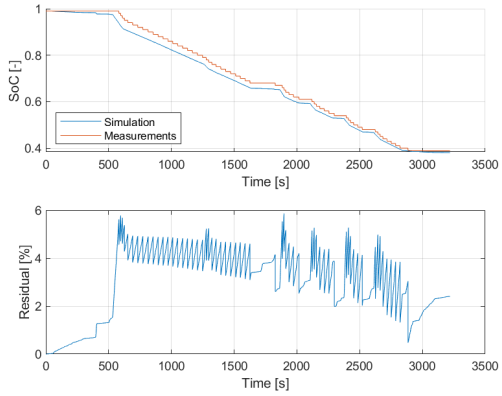

Figure 6.20: A comparison between the flight test cell SoC data and the simulated SoC using a 3RC model

6.3.4. Number of RC Pairs Comparison

In Figure 6.21 a comparison between the simulated voltage and the measured voltage can be seen for various order xRC EECM models. From Figure 6.21 it can be seen that, as expected, the performance of the 0 RC model is the worst. This model is unable to model the voltage dynamic behavior accurately, and this shows when looking at the residual plot. The 0RC EECM has the highest residual RMSE of 1.916 % and also the highest maximum error, the residual spiking to a maximum of 9.0101% at some time steps.
The 1RC EECM is greatly improved over the 0RC EECM, as can be seen in Figure 6.21. It has a lower RMSE of 0.60% and a much lower maximum error, with peaks only reaching the error of 2.34 %. The better accuracy of this model can be attributed to the 1RC branch being able to accurately model voltage dynamic behavior and, therefore, producing more accurate results modeling the voltage after large current changes.
The 2RC EECM is again an improvement over the 1RC model. The maximum error for the 2RC model only peaks at 1.87% and is therefore lower than the maximum error found with the 1 and 2RC models. The RMSE of the 2RC model is higher than that of the 1RC model at 0.6529 %. This is due to the fact that between 1000 seconds and 2000 the 1RC model has almost no residual error and the 2RC has a slight error between 0 and 1%. The difference in RMSE however is almost negligible and, therefore, the 2RC model is deemed only marginally more accurate as it produces less maximum error at large current changes.
The 3RC model is not an improvement of the 2RC model. The maximum error is higher at 2.18% and the RMSE is also higher at 1.52%. The reason for the higher RMSE can be attributed to the fact that the voltage simulated before any current is drawn from the battery is overestimated. As no current is drawn from the battery until 500 seconds, the SoC does not change until that point. This means that the accuracy of the lookup table entries of the EECM parameters at this high SoC level have a very strong influence on the RMSE as they are used to model the voltage over a large amount of simulation time. The reason that the maximum error is higher could be due to the fact that with 3RC branches the parameter estimator software is over fitting the data. The parameter estimator is essentially applying a curve fitting algorithm (non-linear regression). With the increase in RC branches the amount of model parameters increases, and it could be the case that this amount of parameters is too much considering the PCCT data. This is especially true since the sample rate of the PCCT data was only 0.5 seconds. Preferably, the sample rate would have been higher at at least 0.1 seconds to better see the voltage dynamics and to have more data to perform the regression. With the higher sample rate, the 3RC model parameters might not have over-fitted the data and could have produced more accurate model results.

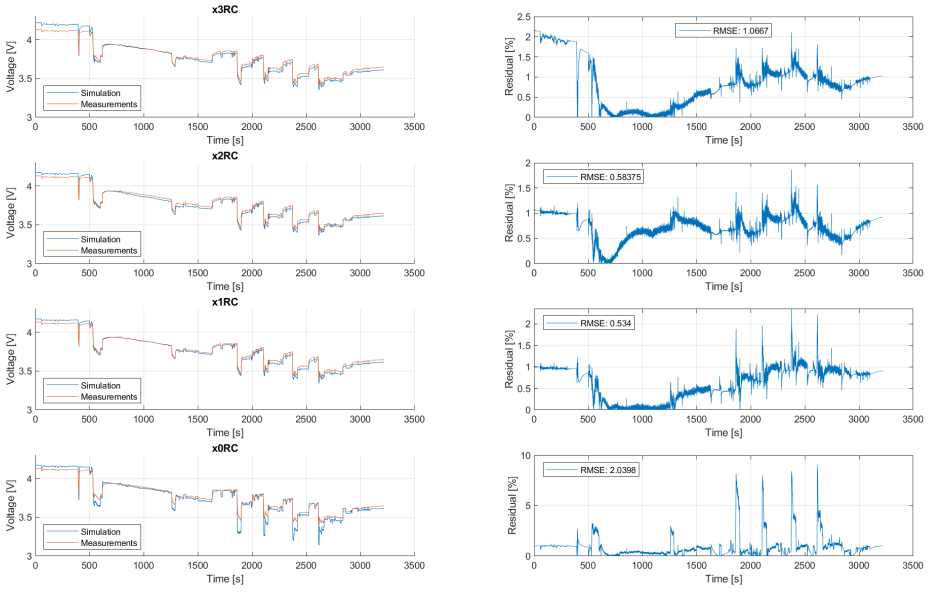

Figure 6.21: A comparison between the voltage modelling accuracy of various xRC models

In Table 6.1 an overview of the maximum error and RMSE for the various xRC models is provided. As can be seen, the 2RC EECM produces the most accurate results when compared to the test data of this test flight. The

3RC was expected to be more accurate than the 2RC model, but due to the reasons explained in this section, this was not the case. The decision was made to use the 2RC EECM model as the main EECM electrical model for the remainder of this thesis work. This is due to, next to having the best accuracy, the 2RC EECM being computationally less expensive to use since there are fewer electrical circuit elements to model and therefore the computational time will be reduced when compared to a 3RC EECM.

Table 6.1: An overview of the various xRC EECM and the RMSE and Maximum Error

EECM	**RMSE [%]**	**Max Error [%]**
0RC	2.0398	9.01
1RC	0.534	2.3389
2RC	0.5837	1.856
3RC	1.0667	2.1750

6.4. Thermal Model: Validation & Cooling Strategies Comparison

This section will validate the thermal model developed and at the same time provide a comparison between the effectiveness of the three thermal management strategies of ribbon, cold plate and air cooling. The reason why three thermal management strategies are analyzed is because the internal layout of the Pipistrel battery pack was unknown, and hence multiple cooling options needed to be considered. It was already clear that the battery pack is liquid cooled (section 2.3) and not air cooled. However, the air cooling case is added as a hypothetical variant in order to compare the effectiveness of the various cooling strategies. The effectiveness is based on the weight of the BTMS, the maximum temperature of the pack during the simulation, and the amount of heat that is rejected to the coolant. All of this will be presented in subsection 6.4.1. subsection 6.4.1 will be followed by three subsections that highlight the sensitivity of each of the three BTMS to their own geometric parameterization as described in subsection 2.3.3. This can be found in subsection 6.4.2, subsection 6.4.3, and subsection 6.4.4.

6.4.1. Validation & Strategy comparison

The validation presented in this section is based on two sets of test flight data. The first is flight 030. This is the same flight profile as that used in subsection 6.3.3. An overview of altitude, airspeed, coolant temperature and ambient temperature logged during flight can be seen in Figure 6.22. Like the cell temperature, the coolant temperature had a temperature resolution of 1 $^{\circ}C$. This is very coarse and caused some fluctuations at a number of time steps as seen in the figure. As the inlet coolant temperature is prescribed to the thermal model, these fluctuations caused numerical modeling errors. For this reason, the measured coolant temperature profile was smoothend using two linear lines to interpolate the coolant temperature. The simplification can be seen as the orange line in the coolant temperature plot in the figure. For additional clarity, the altitude and airspeed during the flight is also provided in the top two graphs in the figure.

The second test flight data set used to validate the model is FLT091. This was a flight conducted in Aruba. This flight test was included since it allows for the investigation of the model under higher ambient temperature conditions. An overview of flight conditions and measured coolant and ambient temperatures can be seen in Figure 6.23. Again, the altitude and airspeed during the flight is provided in the two top graphs in the figure.

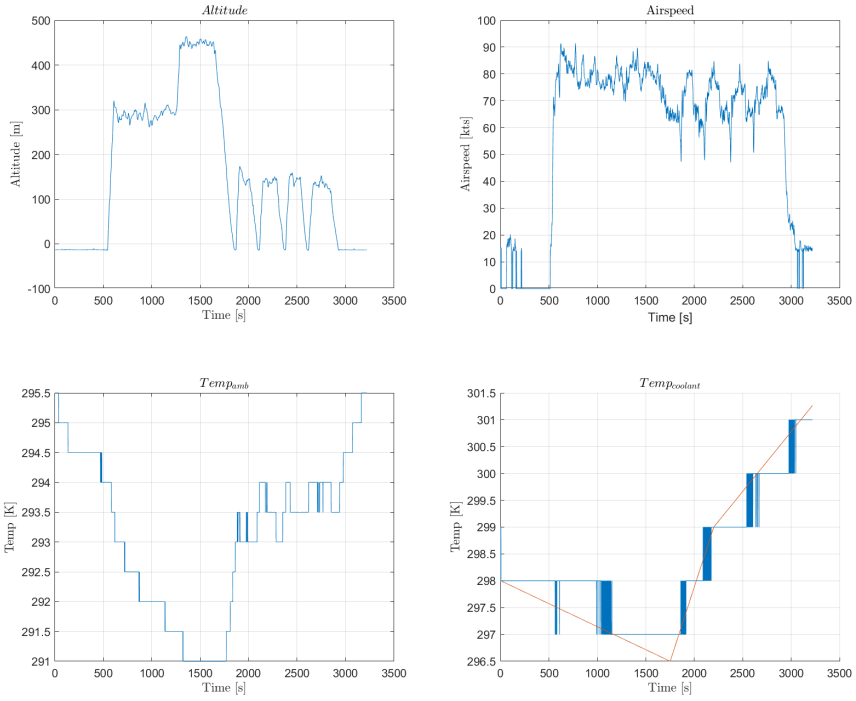

Figure 6.22: An overview of the flight conditions for FLT030

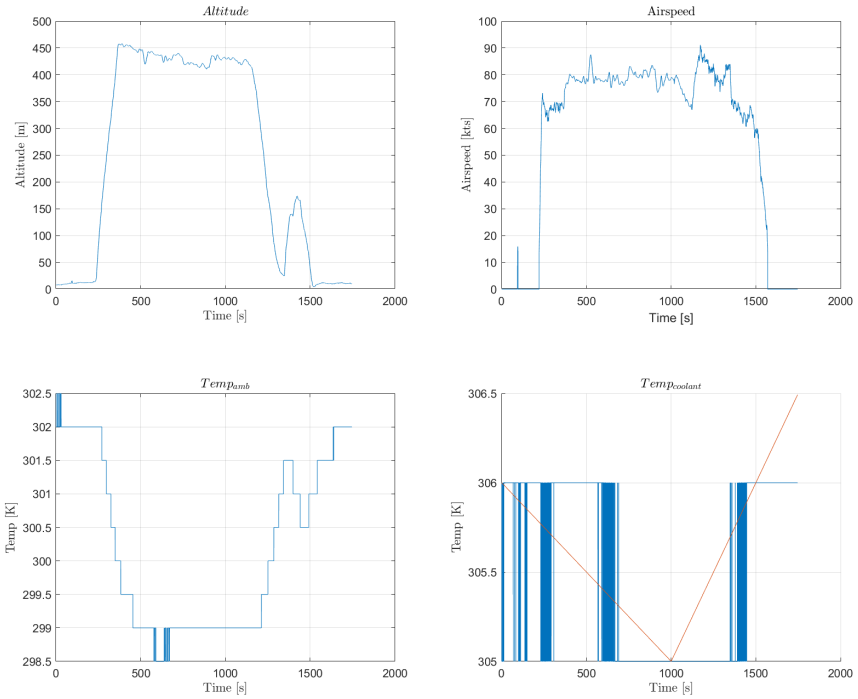

Figure 6.23: An overview of the flight conditions for FLT091

For FLT030, the resulting thermal calculation plot can be seen in Figure 6.24. From the figure it can be concluded that the correlation between the measured maximum cell temperature validation data and the calculated maximum cell temperature is good, as it follows the same trend and magnitude as the validation data for the cooling solutions of the ribbon and the cold plate. As expected, the performance of the air cooling solution is worse than that of the ribbon and cold plate cooling solutions, as can be seen by the higher simulated temperature. The thermal parameters such as the thermal resistances of each cooling strategy can be seen in Table 6.2. These thermal resistances are calculated with the procedure described in subsection 4.3.3.

Table 6.2: Thermal model calculated parameters

BTMS	$R_{coolant}$	R_{amb}	$\dot{m}_{coolant}$	**Mass**	**Power**
Ribbon	0.0033	13.03	0.048 kg/s	3.161 kg	10 W
Cold	0.0219	12.95	0.051 kg/s	3.7013	10 W
Air	0	24.56	0.0059 kg/s	-	50 W

The worse performance of the air cooling strategy can be explained by looking at the heat flux plot in Figure 6.24. For the air cooling strategy, the heat flux to the ambient and the coolant is lower than that of the cooling of the ribbon and cold plate. This is because for the air-cooling method, it is assumed that the left and right sides of the battery do not participate in the heat convection to the ambient environment because they are perpendicular to the air channel directions. In addition to the heat flux to the ambient being lower, the heat flux to the coolant is also lower for the first 1750 seconds of this simulation. This can be attributed to the fact that the mass flow rate of the air used as the coolant is much lower than the mass flow rate of the liquid coolant, as well as the specific heat capacity of the air, as can be seen in Table 6.2.
It can also be noted that for the liquid cooled cases the heat flux to the coolant becomes negative after 1750 seconds. The heat rejection is also negative before 500 seconds but since no current was drawn from the battery during this time period this was expected. The behavior after 1750 seconds was initially not expected. However, when looking at the validation data, it can still be explained. The heat flux becomes negative because the temperature of the coolant becomes greater than that of the battery cells, and thus the coolant does not cool but heats up the cells. When looking at the validation data, the coolant temperature also be-

comes greater than the cell temperature. The reason why this coolant temperature becomes greater than the cell temperature is difficult to determine. After 1750 seconds, the aircraft starts to perform the four landing attempts. It could be that because of the lower airspeeds, lower altitude, higher ambient temperature, and possible higher angle of attack, the mass flow through the heat exchanger that cools the coolant reduces, and thus less heat is rejected from the coolant to the environment causing the coolant to heat up. During landing attempts, there are small periods of time in which the altitude is zero and the aircraft has touched down. During these periods no power and thus current is being drawn from the battery and thus no additional heat is being generated, but the heat is still transported from the battery pack to the compartment as the battery pack temperature is still higher than that of the battery compartment. The lower heat rejection of the coolant via the heat exchanger and the battery cells not generating heat from small periods of time could cause the cell temperatures to become lower than the actual coolant cooling the battery pack.
From Figure 6.24 it can be seen that in general the heat flux to the ambient conditions is greater than that to the coolant. This has two reasons. The first reason is that, even though the thermal resistance to ambient conditions is much higher than to the coolant, as seen in Table 6.2, the temperature difference between the cell and the coolant rarely exceeds 1 degree, whereas the temperature difference between ambient conditions and the cell temperature is much higher. The second reason is that the heat flux to the coolant is calculated by the increase in temperature of the coolant itself. This temperature increase was modeled with a thermal liquid pipe element from Simscape [50]. This pipe element determines the amount of heat transported by advection/convection by the coolant. The thermal resistance provided is calculated as the thermal resistance to the pipe wall and therefore cannot be compared one-by-one with the thermal resistance to the ambient conditions. There is additional thermal resistance coming from the advection/convection in the pipe element which is determined dynamically inside the model.

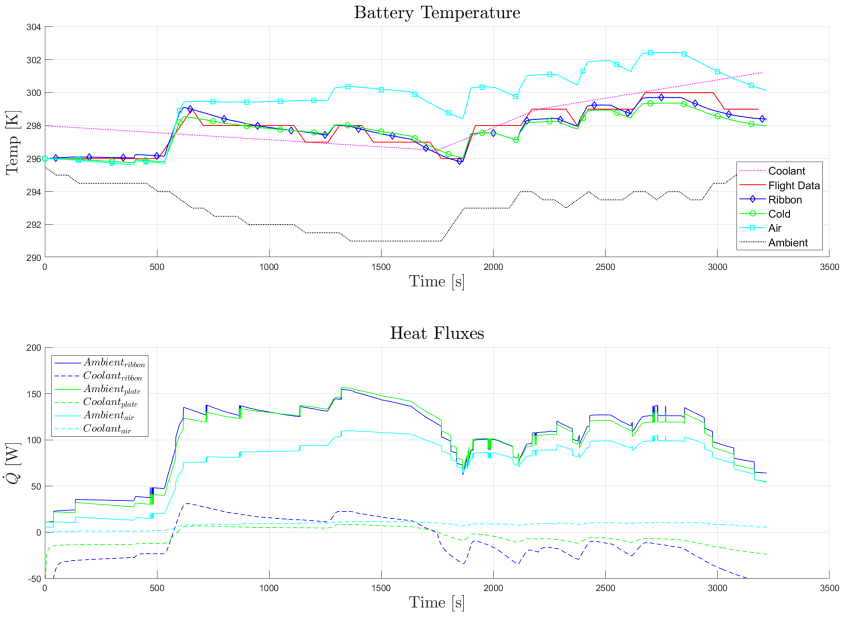

Figure 6.24: The thermal calculations plot for FLT030; Top figure maximum cell temperature bottom figure heat rejections

In Figure 6.25 another validation using flight data from FLT091 (Aruba) can be seen. Again, the simulation data correlate well with the validation flight data. The cold plate options perform slightly better than the ribbon cooling option. The air cooled model performs significantly worse than both liquid cooling options. Like for the FLT030 the heat flux from cell to coolant becomes negative after 1200 seconds. This can be attributed to the same reasons as provided for FLT030. The decrease in altitude and the increase in ambient temperature caused the coolant to be able to reject less heat to the ambient conditions through the heat exchanger. Additional work could be performed to analyze and confirm this explanation further by making a model that can model the heat rejection of the coolant through the heat exchanger based on flight conditions.
From both Figure 6.24 and Figure 6.25 it can be concluded that the correlation between the validation data and the simulated temperature is good and therefore the developed thermal model can be considered vali-

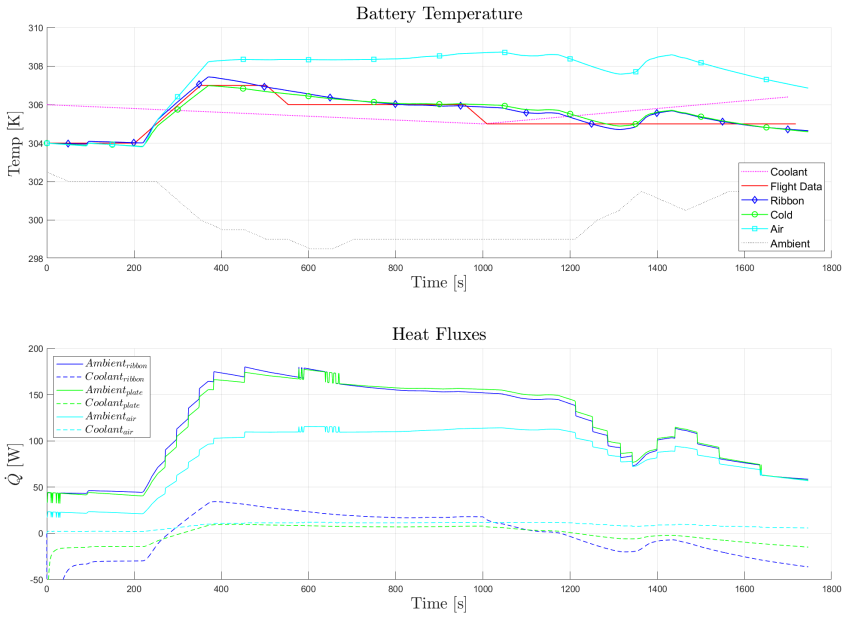

Figure 6.25: The thermal calculations plot for FLT091; Top figure maximum cell temperature bottom figure heat rejections

dated.
When comparing the performance of the three cooling strategies, cold plate cooling was the most effective with the lowest maximum temperature, as can be seen in Table 6.3. However, the cold plate cooling option is almost 0.5 kg heavier, and the difference in maximum temperature is only 0.5 K, so when comparing the cooling methods in terms of performance per unit of mass the ribbon cooling method performs better. The masses of both the ribbon and cold plate cooling solutions are calculated by calculating the volume of the geometry as described in subsection 4.3.3 and multiplying this by the material density. The air cooling method is much lighter because it does not require plates or ribbons to guide the coolant past the battery cells. However, the maximum temperature, and thus the cooling performance of this option is worse than that of the liquid cooling options. The air cooling solution does, however, require a fan but, as the goal of this thesis is not to size this fan, nothing meaningful can be said about its weight.

Table 6.3: A Comparison of the thermal model performance parameters

BTMS	Mass	Power	Max Temp FLT 030	Max Temp FLT 091
Ribbon	3.16 kg	10 W	299.71 K	307.44 K
Cold	3.70 kg	10 W	299.36 K	306.98 K
Air	-	50 W	302.45 K	308.73 K

6.4.2. Ribbon Cooling Sensitivity Analysis

This subsection will show the sensitivity of the ribbon cooling solution to its own geometric parameters. The sensitivity of battery temperature to the ribbon, thickness, angle, factor, and width will be investigated. A schematic of these geometric parameters and their definitions can be found in Figure 4.12 and Figure 4.11 in subsubsection 2.3.3.1. For the simulation, the current profile from FLT030 will be used again and a comparison between the temperature evolution of time will be shown. The results of this analysis can be seen in Figure 6.26.

From Figure 6.26 it can be concluded that the ribbon cooling model is insensitive to the thickness of the ribbon and the width of the ribbon. It can be seen that with a change in ribbon thickness there is almost no change in the simulated temperature. This is because the thickness of the ribbon is much smaller than the area of the ribbon in contact with the cell. This means that the thermal resistance to the coolant will remain small compared to the thermal resistance due to the heat advection/convection in the pipe element even when the thickness of the ribbon is increased to 1.2 mm. The insensitivity to the ribbon width can be explained by looking at the Reynolds number and the mass flow. When the width of the ribbon increases, the hydraulic diameter of the pipe element increases. The relation between the hydraulic diameter and the convective heat transfer coefficient of the fluid is complex and explained by [49]. In general, the hydraulic diameter influences the Reynolds number and Darcy friction factor of the flow, which in turn influences the Nusselt number through the Gnielinski correlation [5]. From the sensitivity analysis performed it can be concluded that for these changes in ribbon width the heat transfer properties of the fluid hardly change, and therefore it is insensitive to the ribbon width.

Figure 6.26 also shows that the model is quite sensitive to the ribbon factor and ribbon angle. The reason for this is the opposite of what happened with the ribbon thickness. Both the ribbon factor and ribbon angle increase the amount of area of the battery cell covered by the ribbon. This area change lowers the thermal resistance of the cell to the coolant but as was already explained for the ribbon thickness the thermal resitance of the cell to coolant is much smaller than that due to the advection/convection in the pipe element. With a larger ribbon factor and larger ribbon angle there is simply more area in the ribbon past which heat convection can take place and the the ribbon becomes better at cooling. Another secondary effect that happens is that due to the additional height and length (angle) of the ribbon it will have more thermal mass. This additional thermal mass will cause the thermal node of the ribbon to remain at a lower temperature longer. This lower temperature increases the heat flux between the ribbon node and the cell node as this is directly proportional to the temperature difference. This lower ribbon node temperature does however cause the wall temperature of the pipe element to be lower and therefor the heat flux to the coolant reduces. The additional ribbon mass could be interpreted as addition thermal mass of the cell node itself and a higher thermal cell mass will give a lower temperature.

6.4.3. Cold Plate Cooling Sensitivity Analysis

This subsection will show the sensitivity of the cold plate cooling solution to its own geometric parameters. The sensitivity of battery temperature to the number of channels on the cold plate, the diameter of the channel, and the thickness of the plate will be investigated. A schematic and definitions of these geometric parameters can be seen in Figure 4.17 in subsubsection 2.3.3.2. For the simulation, the current profile from FLT030 will be used again. The results of the analysis can be seen in Figure 6.27.

From Figure 6.27 it can be seen that the cold plate cooling model is slightly sensitive to channel diameter. The temperature peaks decrease with an increase in the channel diameter. Similarly to the ribbon width the relation between the channel diameter (hydraulic diameter) is complex and non-linear and is described in [49]. The main reason for the better heat transport properties with a larger diameter is that as a result of the larger diameter the amount of surface area exposed to the fluid increases, which in turn increases the available area for heat advection/convection.

The number of channels can be seen to have no effect on the simulated temperature. This is due to the partitioning of the cold plate not changing between the channel number simulations. This means that the number of nodes and thus modeled pipe elements does not change between the different number of channel simulations. That means that for this type of simulation, changing the number of channels actually does not have an effect. In reality, increasing the number of coolant channels in the cold plate would increase the amount of surface area available for heat transport and should, therefore, lead to lower temperatures. However, more channels would mean that the flow velocity in each channel would decrease leading to a decrease in Reynolds number, which could lead to a decrease in convective heat transfer coefficient and thus heat transport. A detailed investigation into heat transfer in a pipe is recommended to investigate this process

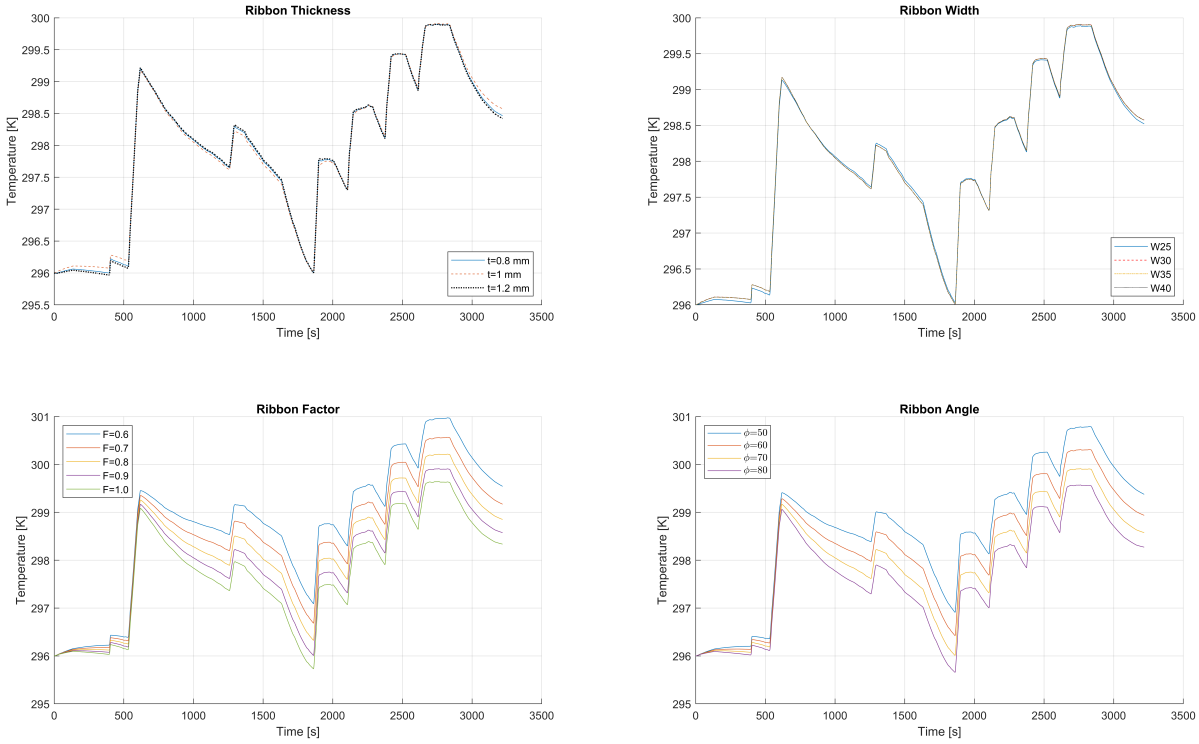

Figure 6.26: The sensitivity analysis of maximum cell temperature of the ribbon cooling to its geometric parameters

in detail.
In Figure 6.27, it can be concluded that increasing the thickness of the plate causes the simulated temperature to be slightly lower. Initially, it is expected that increasing the thickness of the cold plate would increase the thermal resistance from the cell to the coolant and thus increase the simulation temperature. However, increasing the thickness of the plate increases the thermal mass of the thermal node of the cold plate. This means that the cold plate remains at a lower temperature when the heat load remains the same. This lower temperature allows for a larger heat flux to the coolant, which causes a lower simulated battery temperature.

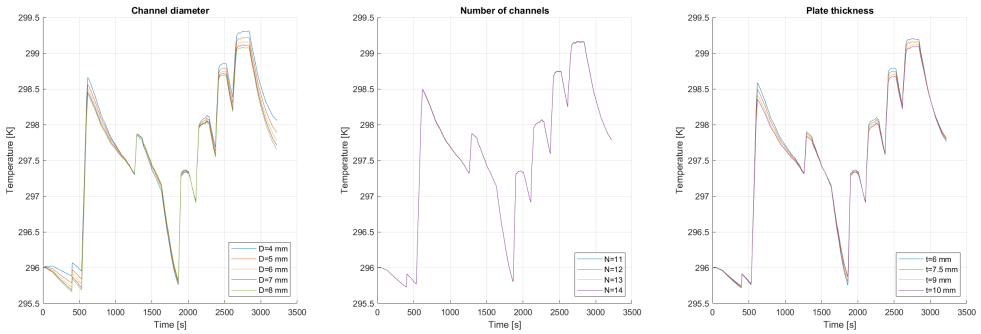

Figure 6.27: The sensitivity analysis of the cold plate cooling to its geometric parameters

6.4.4. Aircooling Sensitivity Analysis

This subsection will show the sensitivity of the air cooling solution to its own geometric parameters. The effect of the size of the intercell gaps through which air flows will be investigated. The results of this analysis can be seen in Figure 6.28. It can be seen that the intercell gap has a very strong influence on the simulated temperature of the air cooling solution. It can be seen in the figure that with an increase in the intercell gap, the simulated temperature decreases. With an increase in inter cell gap the air coolant mass flow rate increases for a fixed pressure ratio. The pressure ratio of the fan is fixed as the electrical power it receives is fixed. The increase in mass flow due to a larger intercell gap with a fixed pressure ratio can be explained with Poiseuille's law [29]. Poiseuille's law states that for a fixed pressure difference an increase in pipe diameter causes a significant increase in flow rate. As the fan power does not change between each simulation, the exit pressure after the fan is a fixed value. The exit pressure after the pipe is also fixed at the ambient pressure. This means that the pressure difference between the inlet and exit of the pipe is fixed. The assumption does have to be made that the fan blowing the air is always able to provide the necessary pressure difference and that there is no limit on the amount of mass flow available. With the fixed pressure difference and Pouiseuille's law, it can be concluded that increasing the inter-cell gap will increase the hydraulic diameter of the pipe, and thus increase the flow rate of air. The increase in air flow rate was confirmed by looking at the air coolant mass flow rate in the simulation data. This mass flow rate is reported in Table 6.4 and the trend of increasing the mass flow rate with increasing inter-cell gap can be seen. The increase in mass flow rate means that more heat can be transported away by cooling air, which in turn will result in a lower cell temperature, as seen in Figure 6.28. It should be noted though that an increase of intercell gap also results in a larger battery pack volume, which is not considered here.

Table 6.4: The mass flow rate of the air coolant

Intercell Gap [mm]	Mass flow rate [kg/s]
0.5	0.0005
1.0	0.0042
1.5	0.0076
2.0	0.0109
2.5	0.0159
3.0	0.0216

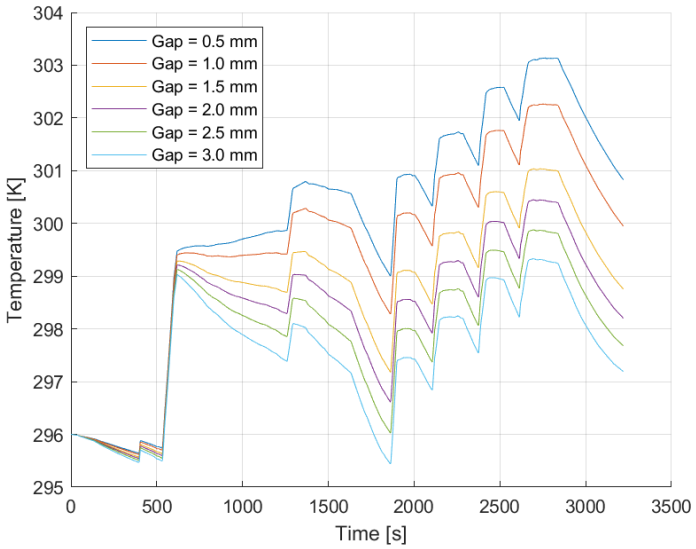

Figure 6.28: The sensitivity analysis of the cold plate cooling to its geometric parameters

6.5. Nodal Convergence Analysis

This section will show the results of the nodal convergence analysis. Similarly to the determination of the number of RC pairs in the EECM, see subsection 6.3.4, one can also determine the necessary number of thermal nodes. This analysis investigated whether the simulated battery cell temperature solution converges to one solution if the number of thermal nodes is increased. The results of the analysis can be seen in Figure 6.29. For this analysis, the current profile from FLT030 was again used. The convergence criterion used was the maximum simulated battery temperature using the FLT030 current profile.

From Figure 6.29 it can be concluded that the maximum simulated battery temperature converges to one solution when the number of thermal nodes increases. During the actual flight (t > 500s) The difference in maximum temperature between the model with 56 nodes and 288 nodes is much smaller than the difference between 32 and 56 nodes, meaning the solution converges to one solution with an increase in number of nodes. This is also clear from the first plot in Figure 6.29. This plot shows the percentage difference when changing the number of nodes in the model from one amount to the next. It can be seen that there is a large percentage change when going from 4 nodes to 8 but this percentage differences decrease each time a change to a model with more nodes is made meaning the solution is converging.

The addition of more nodes does provide a more accurate (converged) solution but comes at the cost of much larger simulation times. In the bottom plot of Figure 6.29 the simulation time versus the number of nodes is plotted. It can be seen that the simulation time of 288 nodes is three times as long as that of 32 nodes, even though the temperate difference is only very small at 0.0199 K. This means that careful consideration must be made when deciding on the amount of nodes to be used in the model, as using an excessive amount of thermal nodes could only provide a small increase in simulation accuracy, but a very large increase in simulation time. In the end the decision was made to use a model with 20 nodes for the validation and operational analysis.

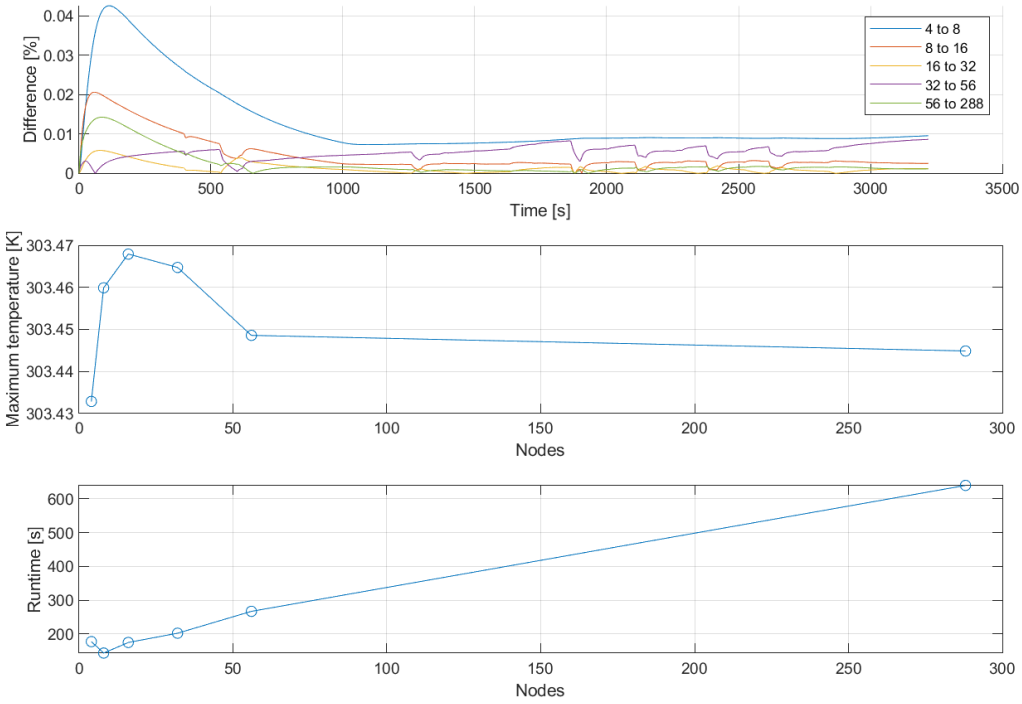

Figure 6.29: The results of the nodal convergence analysis of the thermal model

6.6. Operational Analysis

This subsection will present two types of operational analysis performed with the developed model. First, a cold weather analysis will be performed in subsection 6.6.1. For this analysis, an investigation of what would happen to the battery performance when performing a flight in cold weather is performed. For this analysis, the FLT030 flight data was again used, but all temperatures had been lowered by 20 K. A comparison will be presented between the battery performance when preconditioned to 293 K and when not preconditioned. Second, an investigation of the battery thermal behavior during charging will be performed. This investigation will be presented in subsection 6.6.2.

6.6.1. Cold Weather Operations

This subsection will show how the thermal model of the battery can be used to perform battery performance and thermal analysis under cold weather conditions. For this analysis, the flight data from FLT030 flight is again used. All FLT030 temperature measurements are reduced by 20 K, placing the temperatures just above the lower limit of the temperature operating window of the Pipistrel battery of 273 K [68]. For cold weather operations, two types of analysis will be performed. For the first analysis, the initial battery temperature is equal to the lowered measurement temperature. For the second analysis, preheating of the battery is applied. This means that before the flight the battery is pre-heated to 20 $^{\circ}C$.

Figure 6.30 shows the results of the two cold weather analysis. From the figure it can be immediately seen that the battery temperature of the preheated battery is much higher than that of the non preheated battery. The difference in temperature between the pre-heated and non preheated battery packs remains constant at around 8 K throughout the simulation. The not preheating of the battery and thus lower battery temperature has an effect on the terminal voltage of the battery pack. As could be seen in Figure 6.10, a lower cell temperature provided a lower output voltage at the same current. This effect can also be seen in the voltage plot in Figure 6.30. The lower output voltage means that the amount of electrical power available will be lower as it is the product of the battery voltage times the battery current. During the flight, however, the power required does not change as the aircraft does not descent or lose any speed. In order to still meet the aircrafts power requirements with the lower output voltage, the amount of current drawn from the battery should increase which in turn means that more charge is being drawn from the battery pack.

The amount of extra charge drawn from the battery due to the lack of preheating of the battery can be calculated by the following procedure. First, two simulations are run; one with preheating and one without pre-heating using the default current profile. From the preheated simulation the required power is calculated by multiplying the output voltage by the current. With this required power known, a new current profile can be calculated by dividing the required power by the simulated voltage to find the current. This new found current will be higher than the initial current profile. A new simulation is now run with this new current profile. The output voltage of this simulation will be lower than that of the previous non-preheated simulation, as the output voltage of a battery decreases when more current is drawn from the battery. The entire procedure therefore has to be repeated a number of times. Therefore, a number of iterations are necessary until the new found current profile converges to a solution. One final simulation can then be performed with the final current profile to find the difference in SoC between a preconditioned and non preconditioned battery.

The results of the iterative analysis can be seen in Figure 6.31. The iterative calculations required 3 iterations to converge to a solution. From the SoC plot in Figure 6.31 it can be seen that the difference in simulated SoC for preheated and non-preheated batteries is small. The difference in the final SoC level was found to only be 1.3%. This difference is small, especially compared to the amount of energy it would take to heat the battery pack to 293 K. When considering a total of 288 battery cells in a battery module with a mass of 50 grams and a Cp of 1050 J/kgK, a total mount of 302.4 kJ of heat would be needed to heat them up by 20 degrees. The amount of energy wasted because the battery is not preheated is only 5.4 kJ. Therefore, it would not be efficient to use the batteries own electrical energy to preheat the battery. The difference in SoC is expected to be greater when the ambient temperature is below zero, as the behavior of the lithium ion battery cell becomes more non-linear at sub-zero temperatures [40]. However, since the PCCT was not conducted at temperatures below zero, the EECM model is not applicable in this temperature range. Additional PCCT data would be needed to expand the EECM model to perform an investigation at subzero temperatures. Preheating of the battery when the aircraft is still connected to the charger is recommended, as it not only increases the amount of energy available in the battery. However, as seen in Figure 6.30, the battery temperature comes very close to the operating limit of 273 K when not preheated, while for the preheated case it remains far from this limit. By preheating the battery it should, therefore, remain in a safe temperature operating window even when the outside air temperatures are below the safe operating window.

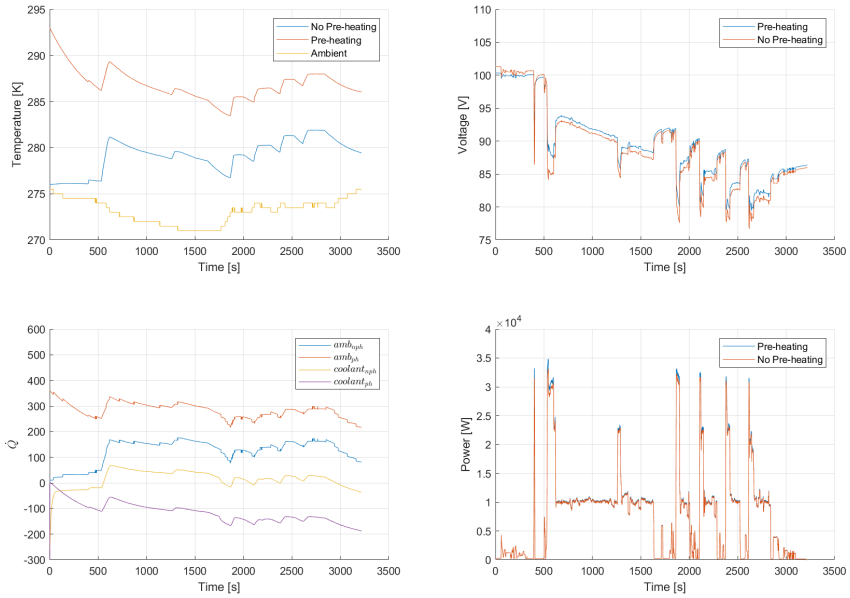

Figure 6.30: A comparison between the battery temperature, heat flux, output voltage (of 1 of the 4 vertical modules) and power for a precondition and non preconditioned battery pack

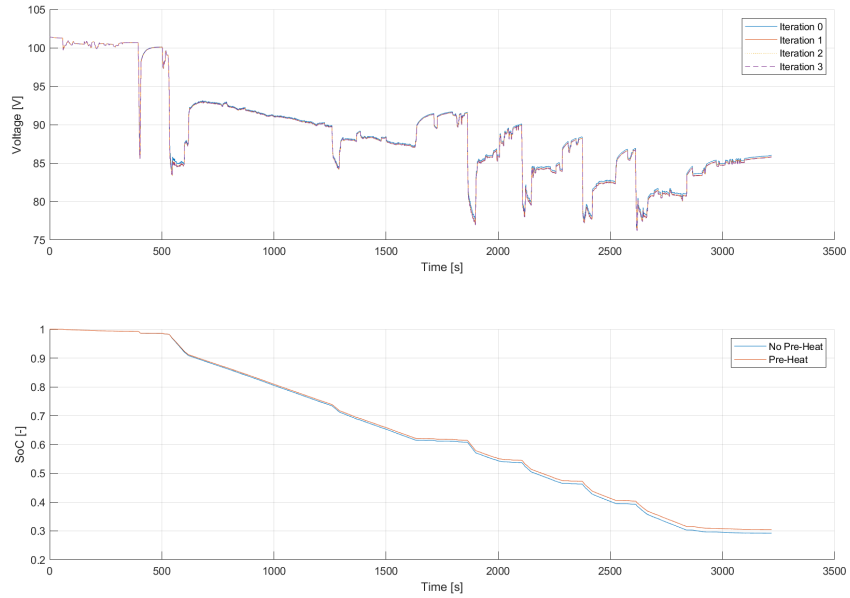

Figure 6.31: A comparison between the current iteration calculations for the non preconditioned battery pack

6.6.2. Charging Operations

This subsection investigates the thermal behavior of the battery pack during charging. For this analysis, the assumption is made that the EECM parameters do not experience current directionality. The EECM parameters of the battery pack are the same for a positive (charge) current as for a negative (discharge) current. The results of the analysis on a battery module can be seen in Figure 6.32. From the figure it can immediately be seen that the simulated voltage is higher than the measured voltage by a few volts. This difference can be attributed to the fact that the EECM parameters were not estimated for positive currents but used the circuit parameters for negative current.
Similarly to the thermal model validation in subsection 6.4.1 the temperature resolution of the measurement data is only 1 degree, therefore, the conclusions that can be drawn from the comparison with these data are limited. However, in Figure 6.32 it can be seen that the simulated battery temperature correlates well with the measured battery temperature. It can also be concluded that the temperature increase during charging is very limited. This can be attributed to the charging current only having a maximum of 20A equaling around 0.5C. This is a low C-rate, so it is expected to have limited battery cell heating. Fast charging is expected to be applied to future electric aircraft. Fast charging is already being applied in electric cars where the C rate can reach 4C [26]. Larger C rates would significantly increase the amount of heat produced by the battery pack as it scales with the square of the current. At a time of 750 seconds, a couple of drops in current can be seen. These drops in the current profile are likely due to sensor errors.

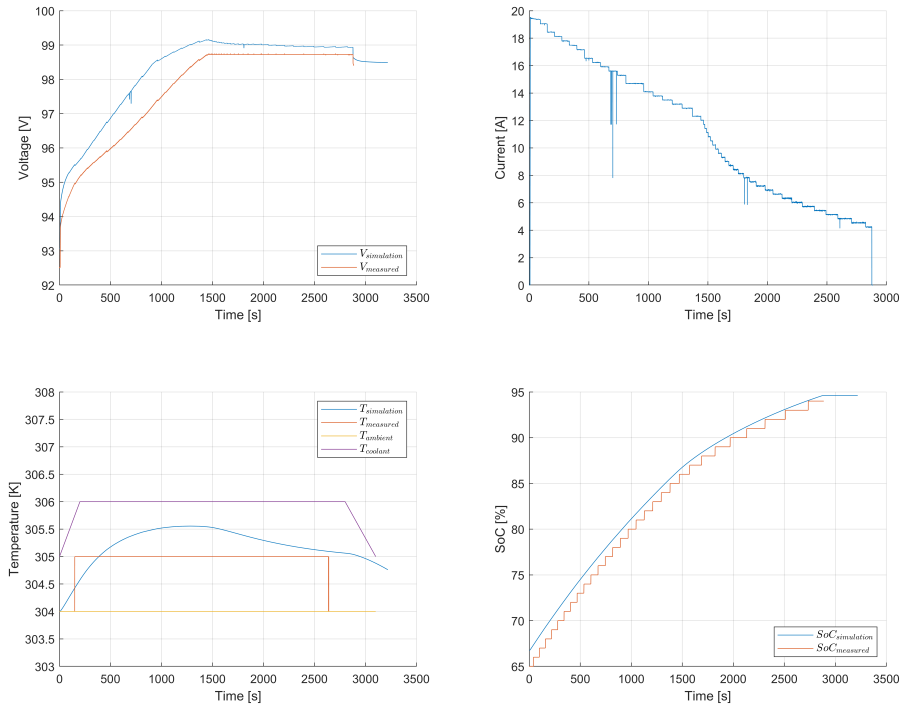

Figure 6.32: The charging operations plot for FLT091

6.7. Scale Up Calculations

This section will describe the potential to scale the developed battery electro-thermal model to larger aircraft classes. With this scale-up calculation, the developed thermal modeling methodology will be applied to a different use case. The use case that will be considered for this calculation is the Eviation Alice [76]. The Eviation Alice is a 9 passenger fully battery electric aircraft (under development) with a claimed range of 450 kilometers. An image of the aircraft can be seen in Figure 6.33. First, a calculation on the energy and power requirements will be presented in subsection 6.7.1 followed by the size of the battery pack in subsection 6.7.2. Finally, this session will be concluded with a thermal simulation of the battery pack for a typical mission of the E-viation Alice in subsection 6.7.3.

Figure 6.33: An image of the E-viation Alice Aircraft [76]

6.7.1. Energy & Power Requirements

This subsection will show the calculation of the energy and power requirements of the battery pack of the E-viation Alice. This calculation procedure is based on the procedure presented in [67] which questions the claimed performance of the aircraft. [67] presents the range calculation with realistic assumptions on the technical parameters required to calculate the mission range. This calculation procedure was implemented in Matlab and executed with the parameters listed in Table 6.5.

The Alice is powered by two Mangi650 electric motors producing a maximum power peak power of 640 Kw each [67]. For this calculation, it is assumed that each electric motor will have its own independent battery pack. The amount of power that the battery pack needs to deliver can be calculated with Equation 6.1. The assumed power train performance parameters are listed in Table 6.6.

$$P_{battery} = \frac{P_{aircraft}}{\eta_{prop} \cdot \eta_{motor} \cdot \eta_{inverter}} \tag{6.1}$$

Table 6.5: The aircraft performance parameters used in the Eviation Alice power calculation

Parameter	Value	Unit
Wing span	19.2	[m]
Wing area	28.9	[m2]
Wing loading (W/S)	259	[kg/m2]
M_{TOW}	7491	[kg]
$\frac{OEW}{M_{TOW}}$	0.5	[-]
M_{pay}	1135	[kg]
C_{d_0}	0.029	[-]
e	0.83	[-]
ρ_{cruise}	0.904	[kg/m3]

Table 6.6: The powertrain performance parameters used in the Eviation Alice power calculation

Parameter	Value	Unit
P_{max}	640	[Kw]
η_{prop}	0.82	[-]
η_{motor}	0.94	[-]
$\eta_{inverter}$	0.98	[-]
GED	230	[Wh/kg]

With the known performance parameters of the aircraft and the power train, the power profile of the aircraft and the range of a typical flight can be calculated using the method from [67]. The resulting power profile from this calculation can be seen in Figure 6.34, where each of the two battery packs has an energy content

of 305 kWh. With the found power profile, a new range can be calculated. This newly calculated range now becomes only 133 kilometers. This is only a third of the range promised by the manufacturer. The calculated range could be increased by increasing the GED of the pack or the fraction of $\frac{OEW}{M_{TOW}}$, but since the goal of this thesis is not to redesign the aircraft but to perform simulations on the thermal behavior of the battery pack, no changes to the technical parameters will be made and the range will remain the same as is at 133 kilometers. The next section, subsection 6.7.2, will show how the power profile can be used to size the battery pack.

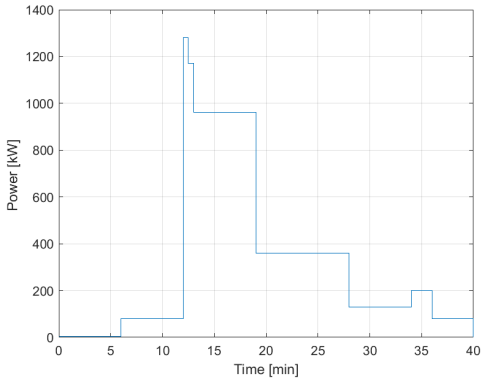

Figure 6.34: The calculated power profile of the E-viation Alice for a typical mission

6.7.2. Battery Sizing

With the power profile known, as seen in Figure 6.34 the battery cell configuration can be calculated. For this calculation, the assumption is made that the battery will have an 800 Volt architecture to be able to deliver the 650 kW of power to each electric motor without excessive current flow. The number of parallel and series cells can be calculated with the method described in subsection 4.2.3 For this calculation, Samsung INR1865033G battery cells will be used again, as no other cell specification is currently available.

From the calculation, it was found that the battery pack should have 220 cells in series and 120 cells in parallel to meet the 800 volt and capacity requirements. The exact stacking arrangements of the battery pack in the Alice are unknown, and therefore a stacking arrangement of the battery cells to make a battery pack is assumed. The assumed stacking arrangement resulting can be seen in Figure 6.35. The stack arrangement was chosen so that two of these battery packs could fit inside the fuselage of the aircraft. In the aircraft, the battery pack is placed inside the underbelly. For this reason, the decision was made to use only two vertical cell layers to allow the battery pack to be easily fitted in the aircraft. With the aircraft having a total length of 17.4 meters, two of these battery packs should fit end to end inside the underbelly of the aircraft's fuselage.

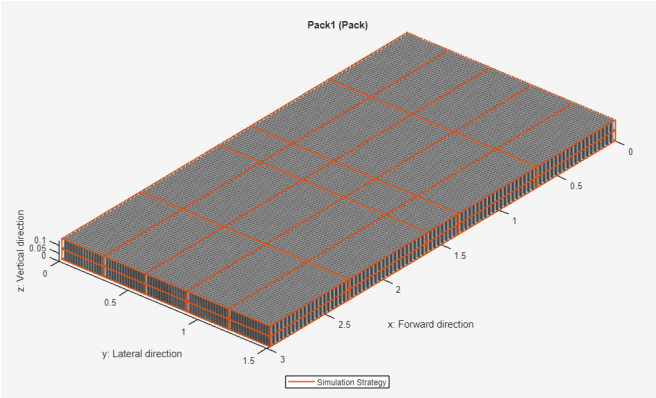

Figure 6.35: The cell stacking arrangement for the battery pack of the E-viation Alice

6.7.3. Thermal Analysis

This subsection will show the results of the thermal analysis performed on the larger battery pack. In the upper left-hand figure in Figure 6.36 the voltage of the battery pack versus time is presented. It can be noted that initially the voltage is higher than the assumed 800 Volt architecture at 925 volts. This is due to the fact that a nominal voltage of 800 Volt of the battery pack was assumed and used to size the battery pack. At higher SoC the battery cells have a higher voltage and thus the battery pack voltage at high SoC is higher than 800 Volts. In the upper right corner, the power profile used in the simulation can be seen. This is the power profile for one motor. To find the total power required by the aircraft this number needs to be multiplied by the number of engines. The way this power profile was derived is presented in subsection 6.7.1. The lower right-hand corner of Figure 6.36 shows the flight altitude used during the simulation.
The most interesting plot in Figure 6.36 is the temperature plot in the lower left corner. In this plot, the temperature of the battery pack, the ambient temperature, and the coolant are plotted. The ambient temperature is calculated using the flight altitude and the ISA standard atmosphere. The coolant temperature is assumed to follow the same trend as the ambient temperature as it is cooled by a ram air heat exchanger.
What can be seen in Figure 6.36 is that initially the temperature of the battery pack starts to increase as the take-off phase of the flight starts. As the altitude of the aircraft increases, the ambient temperature starts to decrease. This decrease in ambient temperature causes the battery pack to loose more heat to the environment. At some point, this heat loss becomes greater than the heat produced inside the battery pack, causing the battery pack to cool down. The increase in heat flux to the environment can be clearly seen in Figure 6.37. From the figure it can be seen that the heat flux to the environment is maximum at around 1200 s. This is also the time when the cruise phase of the flights starts, so the ambient temperature is at its lowest temperature and the battery pack is still relatively hot. This gives the highest temperature difference between the battery pack and the ambient atmosphere, resulting in the largest heat flux. It should be noted here that the calculations were performed with perfect thermal conduction between the battery ambient environment (the compartment) and the outside air.

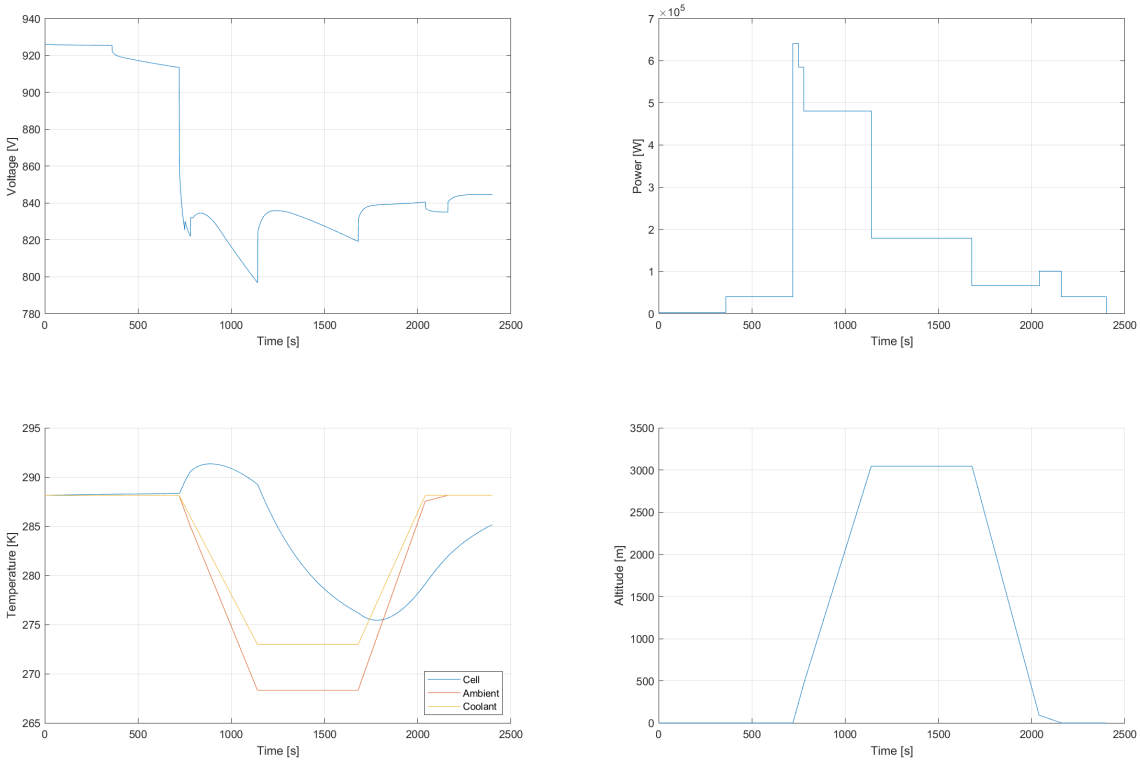

Figure 6.36: The thermal analysis plot of the scaled up battery pack

From Figure 6.36 it can be seen that the minimum battery pack temperature reached is 275 K. This puts the battery pack temperature very close to its operational limit of 273 K. If the flight altitude had been higher or the flight had been longer, this operational limit would have been exceeded. To prevent the battery pack from exceeding this lower temperature operational limit, it would be advised to provide better thermal insulation for the battery pack. When the battery pack is better thermally insulated or when the aircraft skin surrounding the battery compartments has low thermal conductivity (like composite materials), the heat flux to ambient conditions would be reduced, and thus the battery would be less affected by the low ambient temperature conditions. A different solution would be to add a heater to the BTMS coolant loop and heat up the coolant and pump this hot fluid around the battery pack in order to heat the battery pack back up.

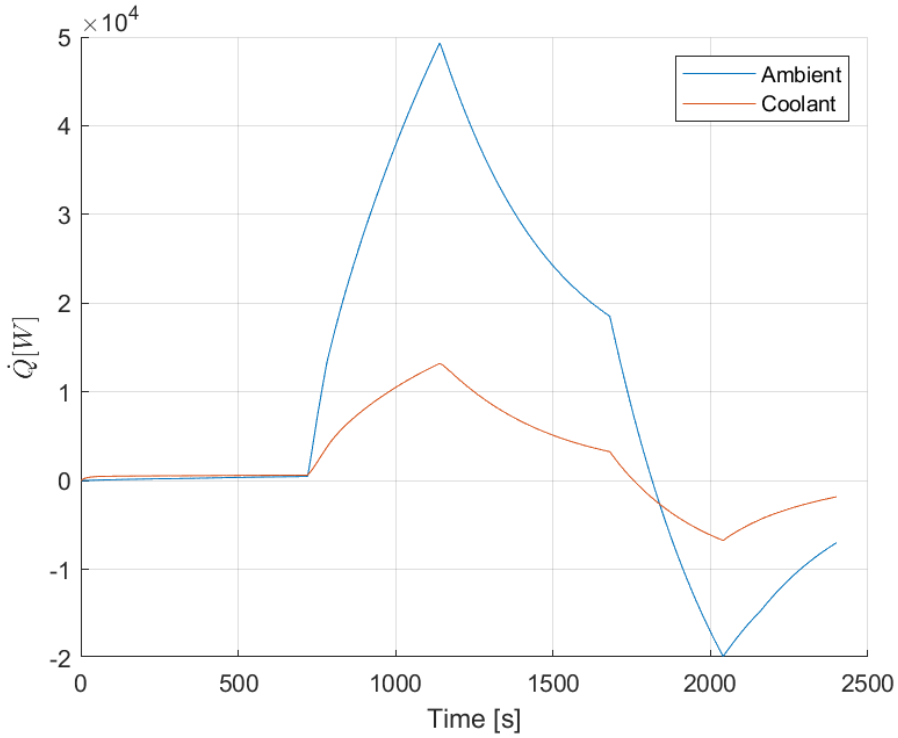

Figure 6.37: The heat fluxes from the battery pack to the ambient and coolant

7

Conclusions

Due to the rapid development of lithium ion batteries in recent years the possibility of battery electric flight has become a reality. With the introduction of lithium-ion battery packs as the main form of energy storage, new design challenges and operational constraints arise. One of the biggest challenges in using lithium ion batteries as an energy source is the careful thermal management of these battery packs.
In this study a combined electronic equivalent circuit and lumped parameter thermal network model was developed to evaluate the performance and thermal behavior of such a lithium ion battery pack considering three thermal management solutions for general aviation aircraft. The thermal management solutions considered in this study are two liquid cooling options in the form of ribbon and cold plate cooling and an air cooling solution. From the combined electronic equivalent circuit model and lumped parameter thermal network model a number of conclusions can be drawn. These conclusions are listed below.

- **SBQ-1:** When the thermal resistances, to the coolant and ambient nodes coming from the heat transfer by convection and conduction, are calculated correctly, the lumped parameter thermal network model is able to simulate the battery pack temperature correctly.
- **SBQ-2:** When a parameter estimation with pulsed current characterization data is performed for a specific lithium ion battery cell, the electronic equivalent circuit model of this cell with estimated parameters is able to simulate the voltage behaviour of the battery cell accurately. The addition of more than two RC-branches to the electronic equivalent circuit model did not significantly increase the models accuracy.
- **SBQ-3:** The battery pack temperature is very sensitive to the outside air of battery compartment conditions. This partly due to the assumed pack housing materials: aluminium. Furthermore the battery compartment walls (e.g. aircraft skin) were not modelled. Furthermore, when operating in low-ambient temperature conditions, preheating the battery pack when not connected to a charger is energy-inefficient.
- **SBQ-3 & SBQ-4:** Of the three thermal management strategies considered, the ribbon cooling solution was the most effective in terms of maximum temperature compared to weight. The air cooling solution was the least effective, as it had the highest maximum pack temperature. The ribbon cooling solution was sensitive to the geometric parameters of the ribbon angle and ribbon factor. Both a higher ribbon factor and the ribbon angle decreased the maximum pack temperature but increased the weight of the system. The cold plate cooling solution was sensitive to the diameter of the cooling channel and the thickness of the plate. A larger channel diameter and larger plate thickness decreased the maximum pack temperature. The air cooling solution was sensitive to the intercell gap. A larger intercell gap decreased the maximum pack temperature as it allowed for a greater mass flow for the same pressure difference.
- **SBQ-1 & SBQ-5:** When the number of nodes in the lumped parameter thermal network model is increased incrementally, after a certain number of nodes this increase has a negligible effect on the calculated maximum cell temperature. From 32 convergence of the simulated maximum pack temperature

is achieved. The difference in simulated maximum pack temperature when the number of nodes is increased is small compared to the increase in simulation time. Therefor, a careful trade-off between simulation time and nodal accuracy must be made considering the required accuracy level.

- The developed combined electronic equivalent circuit model and lumped parameter thermal network model is scale able to other (e.g) larger aircraft applications, which shows that the model can be used during the conceptual or preliminary design phase of battery electric aircraft.

8

Recommendations for Future Work

The work performed in this thesis, despite providing several meaningful insights into the thermal modeling of lithium-ion battery packs for general aviation aircraft, still has room for a number of possible improvements. The current thesis only considers the SoC and battery cell temperature as inputs for the electronic equivalent circuit model. Effects such as C-rate and battery age (SoH) are also known to affect the voltage behavior of lithium ion battery cells and therefore the electronic equivalent circuit model could be improved by including these parameters by transforming the lookup tables from 2D to 4D by including C-rate and battery age (State of Health) and so include the effect of these variables on the EECM parameters. Furthermore, the parameters of the electronic equivalent circuit model in this work were considered to be the same for positive and negative currents (charge/discharge). The voltage behavior of a lithium-ion battery can be different depending on the direction of the current. The electronic equivalent circuit model, therefore, could be further improved by creating two look-up tables considering different current directions. All possible improvements listed to improve the electronic equivalent circuit model would require additional pulsed-current characterization tests under these conditions.

The developed lumped parameter thermal network modeling could be improved by including a heat exchanger model into the coolant thermal loop. In the current thesis work, the coolant temperature is defined as an input and therefore must be assumed and defined for the entire simulation duration. When a heat exchanger model would be included inside the battery model, the heat exchange between the coolant and the ram air could be modeled on the basis of flight conditions such as air speed and altitude. This would allow the model to require only the initial coolant temperature, as the coolant temperature could then be simulated starting from this initial temperature. This would significantly improve the applicability of the thermal model as the ambiguity of predefining a coolant temperature profile for the entire flight duration would be eliminated.

Furthermore, this thesis work did not investigate the effect of radiative heat transfer inside the battery pack. In this thesis, the effect of radiative heat transfer was assumed to be small. An investigation into the validity of this assumption could be useful. In addition to considering radiative heat transfer, a more detailed investigation into the thermal resistances of the lumped parameter thermal model could be conducted. In the current work, the assumption is made that the thermal resistances from cell to coolant and from cell to ambient are constant for every cell. However, in reality, cells closer to the battery pack enclosure walls are expected to have a lower thermal resistance to ambient conditions than cells in the middle of the battery pack because the thermal path for the outer cells is much shorter. A new lumped parameter thermal network model could be developed where the thermal resistances for the cells on the pack boundaries could be defined differently than those of the cells contained in the middle of the battery pack. This would also allow different calculation procedures for the ambient thermal resistance for different locations inside the battery pack. This could be supplemented by performing an in-depth analysis on the heat transfer mechanisms inside a pipe to better understand how the heat flow from cell to coolant is modeled.

A

Appendix A

A.1. Panasonic NCR18650-PF

A.1.1. Drive Cycle Validation

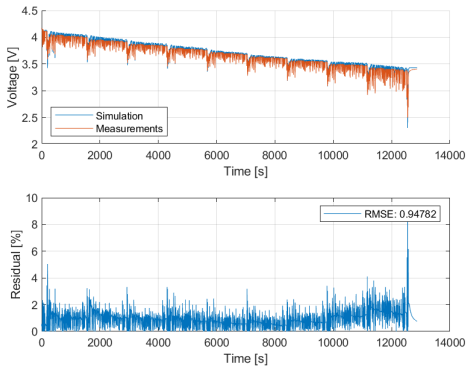

Figure A.1: A comparison between the experiment data [39] and the simulated voltage at a UDDS drive cycle profile at 10 degrees Celsius

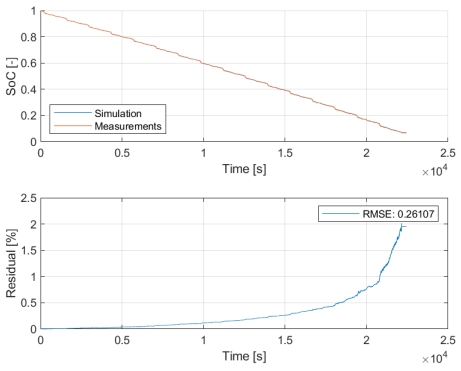

Figure A.2: A comparison between the experiment data [39] and the simulated SoC at a UDDS drive cycle profile at 25 degrees Celsius

A.2. Samsung INR18650-33G

A.2.1. Pulsed Current Characterization

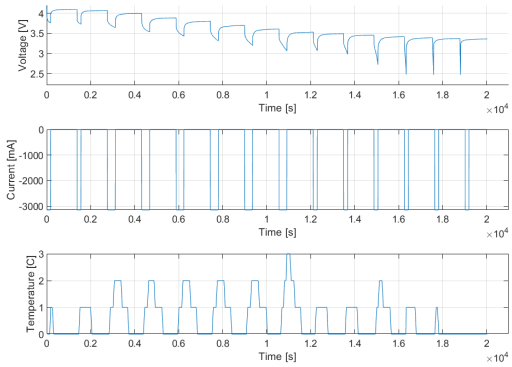

Figure A.3: The results of the PCCT on the Samsung INR18650-33G Cell at 0 degrees Celsius

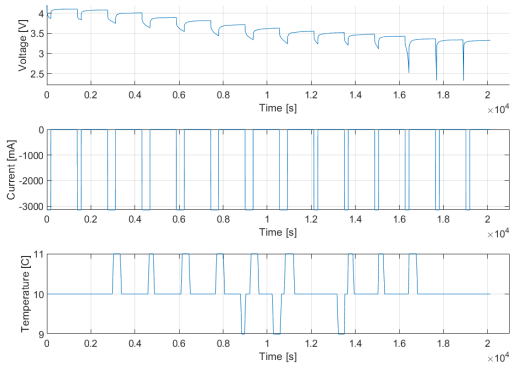

Figure A.4: The results of the PCCT on the Samsung INR18650-33G Cell at 10 degrees Celsius

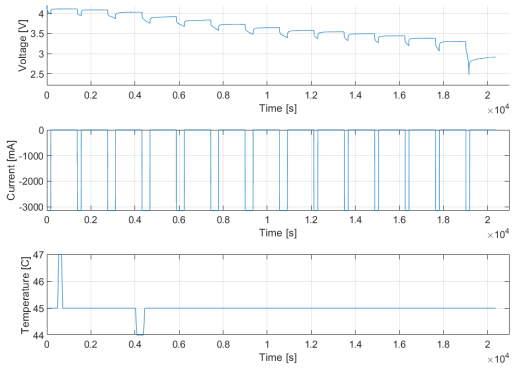

Figure A.5: The results of the PCCT on the Samsung INR18650-33G Cell at 45 degrees Celsius

A.2.2. Entropic Coefficients

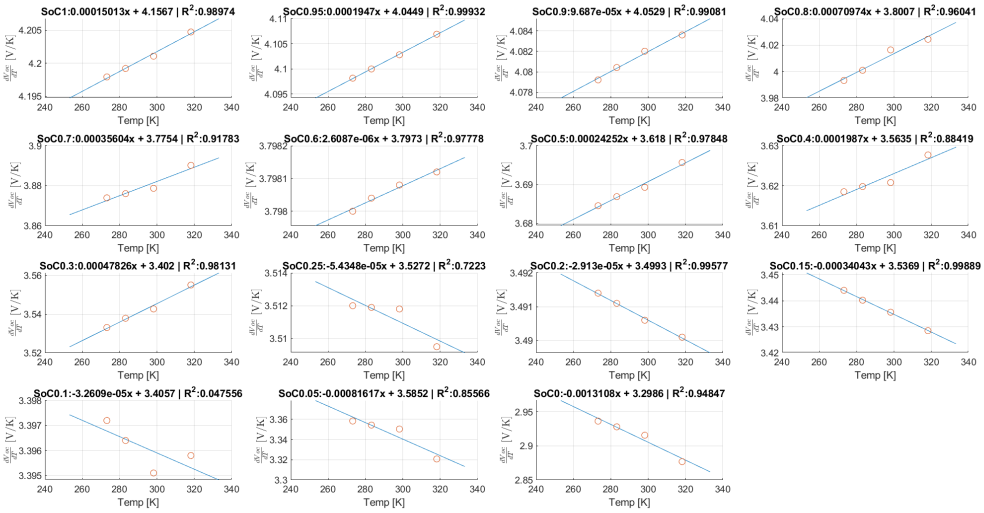

Figure A.6: A plot containing all linear regression plots on the measurement data to obtain the entropic coefficients

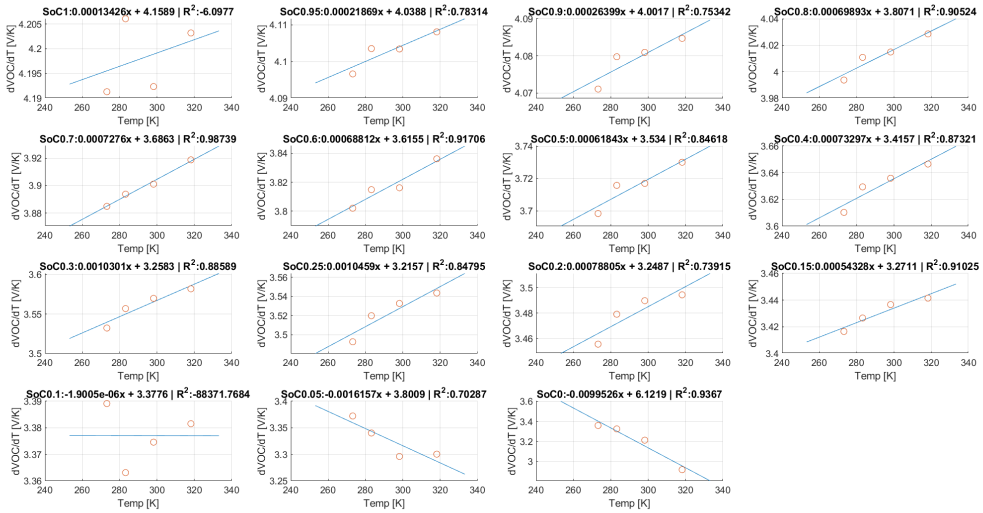

Figure A.7: A plot containing all linear regression plots on the PCCT data to obtain the entropic coefficients

A.2.3. Parameter Plots

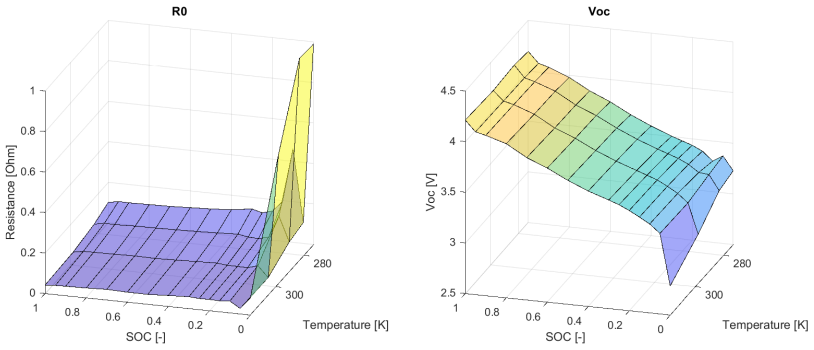

Figure A.8: Paramter estimation results for the Samsung INR18650-33G battery cell 0RC EECM

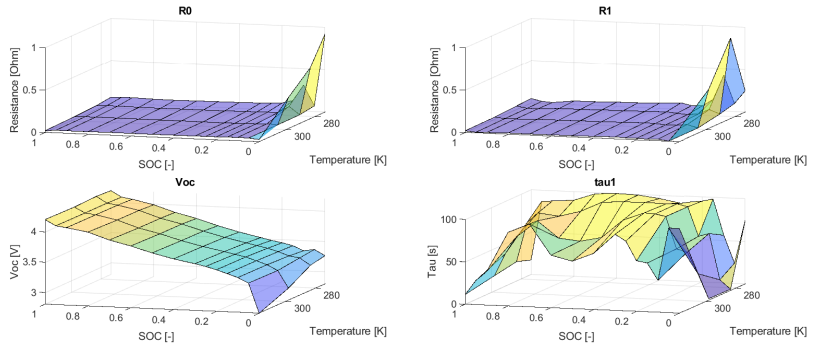

Figure A.9: Paramter estimation results for the Samsung INR18650-33G battery cell 1RC EECM

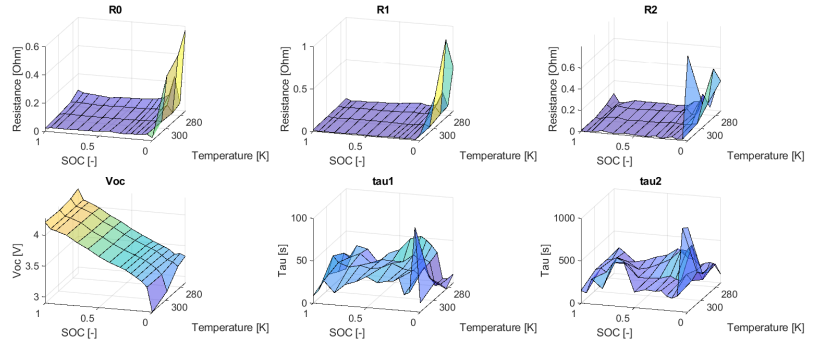

Figure A.10: Paramter estimation results for the Samsung INR18650-33G battery cell 2RC EECM

A.2.4. Continuous Current Verification

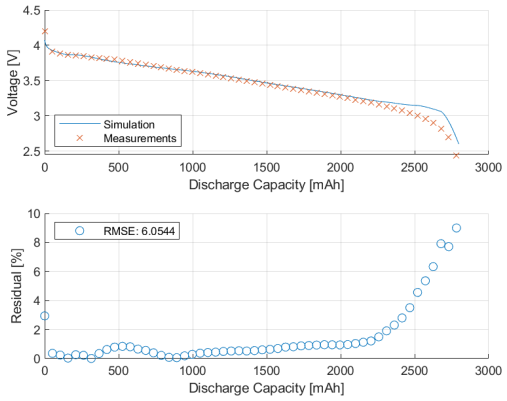

Figure A.11: A comparison between the CDCT data and the simulated voltage at a continuous discharge current of 1C at 10 degrees Celsius

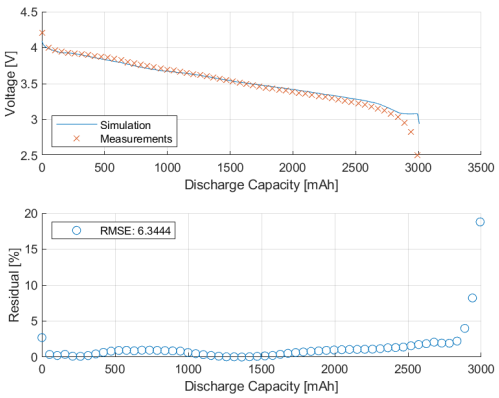

Figure A.12: A comparison between the CDCT data and the simulated voltage at a continuous discharge current of 1C at 25 degrees Celsius

Bibliography

[1] J. Asenbauer, T. Eisenmann, M. Kuenzel, A. Kazzazi, Z. Chen, and D. Bresser. The success story of graphite as a lithium-ion anode material – fundamentals, remaining challenges, and recent developments including silicon (oxide) composites. *Sustainable Energy & Fuels*, 4(11):5387–5416, 2020. doi: 10.1039/d0se00175a. URL https://doi.org/10.1039/d0se00175a.

[2] K&K Associates. *Thermal Network Modeling Handbook*. K&K Associates, Westminster, CO, 97 edition, June 2000.

[3] T.S. Bakker. Literature study battery pack thermal modelling for the preliminary deisgn phase of electric aircraft. Technical report, Delft University of Technology, 2024.

[4] S. Barcellona and L. Piegari. Effect of current on cycle aging of lithium ion batteries. *Journal of Energy Storage*, 29:101310, June 2020. ISSN 2352-152X. doi: 10.1016/j.est.2020.101310. URL http://dx.doi.org/10.1016/j.est.2020.101310.

[5] T.L. Bergman, A.S Lavine, F.P. Incropera, and D.P DeWitt. *Fundamentals of heat and mass transfer 7E*. John Wiley & Sons, June 2011.

[6] P. Bertorelli. Pipistrel Velis Electro: Certified Electric - Aviation Consumer — aviationconsumer.com. https://www.aviationconsumer.com/aircraftreviews/pipistrel-velis-electro-certified-electric/, 2022. [Accessed 03-10-2023].

[7] S. Bhowmick. 6 Most Important Lithium-Ion Battery Chemistries — electronicsforu.com. https://www.electronicsforu.com/technology-trends/six-most-important-lithium-ion-battery-chemistries#:~:text=Lithium%20manganese%20oxide%20(LMO)%20batteries,of%20100%20to%20150Wh%2Fkg., 2023. [Accessed 13-09-2023].

[8] G.E. Blomgren. The development and future of lithium ion batteries. *Journal of The Electrochemical Society*, 164(1):A5019A5025, December 2016. ISSN 1945-7111. doi: 10.1149/2.0251701jes. URL http://dx.doi.org/10.1149/2.0251701jes.

[9] Bosch. PAD2 electric coolant pump — bosch-mobility.com. https://www.bosch-mobility.com/en/solutions/pumps/electrical-coolant-pump-pad2/, 2024. [Accessed 02-04-2024].

[10] CATL. CATL launches condensed battery with an energy density of up to 500 Wh/kg, enables electrification of passenger aircrafts — catl.com. https://www.catl.com/en/news/6015.html#:~:text=at%20Auto%20Shanghai.-,With%20an%20energy%20density%20of%20up%20to%20500%20Wh%2Fkg,a%20short%20period%20of%20time., 2023. [Accessed 08-09-2023].

[11] C.C Chan, E.W.C Lo, and S. Weixiang. The available capacity computation model based on artificial neural network for lead–acid batteries in electric vehicles. *Journal of Power Sources*, 87(1-2):201–204, April 2000. doi: 10.1016/s0378-7753(99)00502-9. URL https://doi.org/10.1016/s0378-7753(99)00502-9.

[12] M. Chen and G.A. Rincon-Mora. Accurate electrical battery model capable of predicting runtime and i-v performance. *IEEE Transactions on Energy Conversion*, 21(2):504–511, June 2006. doi: 10.1109/tec.2006.874229. URL https://doi.org/10.1109/tec.2006.874229.

[13] Y. Chen, Y. Kang, Y. Zhao, L. Wang, J. Liu, Y. Li, Z. Liang, X. He, X. Li, N. Tavajohi, and B. Li. A review of lithium-ion battery safety concerns: The issues, strategies, and testing standards. *Journal of Energy Chemistry*, 59:83–99, August 2021. doi: 10.1016/j.jechem.2020.10.017. URL https://doi.org/10.1016/j.jechem.2020.10.017.

[14] M. Clarke and J.J Alonso. Lithiumion battery modeling for aerospace applications. *Journal of Aircraft*, 58(6):13231335, November 2021. ISSN 1533-3868. doi: 10.2514/1.c036209. URL http://dx.doi.org/10.2514/1.C036209.

[15] European Commission. Batteries europe wg5 application and integration: Mobile, roadmap on mobile applications of batteries. Technical report, European Technology and Innovation Platform on Batteries, 2021.

[16] Z. Cui, W. Hu, G. Zhang, Z. Zhang, and Z. Chen. An extended kalman filter based soc estimation method for li-ion battery. *Energy Reports*, 8:8187, August 2022. ISSN 2352-4847. doi: 10.1016/j.egyr.2022.02.116. URL http://dx.doi.org/10.1016/j.egyr.2022.02.116.

[17] M. Doyle, T.F. Fuller, and J. Newman. Modeling of galvanostatic charge and discharge of the lithium/polymer/insertion cell. *Journal of The Electrochemical Society*, 140(6):1526–1533, June 1993. doi: 10.1149/1.2221597. URL https://doi.org/10.1149/1.2221597.

[18] M. Dürr, A. Cruden, S. Gair, and J.R. McDonald. Dynamic model of a lead acid battery for use in a domestic fuel cell system. *Journal of Power Sources*, 161(2):1400–1411, October 2006. doi: 10.1016/j.jpowsour.2005.12.075. URL https://doi.org/10.1016/j.jpowsour.2005.12.075.

[19] ECGA. Graphite in batteries. $https://ecga.net/wp-content/uploads/2023/02/Graphite-in-batteries_Infosheet_final.pdf$, 2023. Accessed: 21-9-2023.

[20] Cadex Electronics. *Cadex C7000 Series Battery Analyzer User's Manual*. Cadex, 2001.

[21] EngineeringToolbox. Convective Heat Transfer — engineeringtoolbox.com. https://www.engineeringtoolbox.com/convective-heat-transfer-d_430.html. [Accessed 26-04-2024].

[22] Epa. Dynamometer Drive Schedules | US EPA — epa.gov. https://www.epa.gov/vehicle-and-fuel-emissions-testing/dynamometer-drive-schedules, 2023. [Accessed 16-04-2024].

[23] EPEC. Battery Comparison of Energy Density - Cylindrical and Prismatic Cells — epectec.com. https://www.epectec.com/batteries/cell-comparison.html, 2023. [Accessed 06-09-2023].

[24] Fenix. The Ultimate Guide to the 18650 Battery — fenixlighting.com. https://www.fenixlighting.com/blogs/news/the-ultimate-guide-to-the-18650-battery#:~:text=The%2018650%20battery%20has%20a,recharged%20hundreds%20of%20times%20over., 2021. [Accessed 08-01-2024].

[25] FlashBattery. Lithium batteries type: which chemistry should be used? — flashbattery.tech. https://www.flashbattery.tech/en/types-of-lithium-batteries-which-chemistry-use/#:~:text=Batteries%20with%20NCA%20chemistry%20are,250%2D300%20Wh%2FKg., 2023. [Accessed 13-09-2023].

[26] Z. Gao, H. Xie, X. Yang, W. Niu, S. Li, and S. Chen. The dilemma of c-rate and cycle life for lithium-ion batteries under low temperature fast charging. *Batteries*, 8(11):234, November 2022. ISSN 2313-0105. doi: 10.3390/batteries8110234. URL http://dx.doi.org/10.3390/batteries8110234.

[27] F. Geifes, C. Bolsinger, P. Mielcarek, and K.P. Birke. Determination of the entropic heat coefficient in a simple electro-thermal lithium-ion cell model with pulse relaxation measurements and least squares algorithm. *Journal of Power Sources*, 419:148154, April 2019. ISSN 0378-7753. doi: 10.1016/j.jpowsour.2019.02.072. URL http://dx.doi.org/10.1016/j.jpowsour.2019.02.072.

[28] M. Ghiji, V. Novozhilov, K. Moinuddin, P. Joseph, I. Burch, B. Suendermann, and G. Gamble. A review of lithium-ion battery fire suppression. *Energies*, 13(19):5117, October 2020. doi: 10.3390/en13195117. URL https://doi.org/10.3390/en13195117.

[29] K. Guo. Pipe Flow vs Pressure - Relationship & Calculate Tools — sino-inst.com. https://sino-inst.com/pipe-flow-vs-pressure-relationship-calculate/, 2021. [Accessed 29-04-2024].

[30] L. Han, M.L. Lehmann, J. Zhu, T. Liu, Z. Zhou, X. Tang, C.Heish, A.P. Sokolov, P. Cao, X.C. Chen, and T. Saito. Recent developments and challenges in hybrid solid electrolytes for lithium-ion batteries. *Frontiers in Energy Research*, 8, September 2020. doi: 10.3389/fenrg.2020.00202. URL https://doi.org/10.3389/fenrg.2020.00202.

[31] H. He, R. Xiong, H. Guo, and S. Li. Comparison study on the battery models used for the energy management of batteries in electric vehicles. *Energy Conversion and Management*, 64:113–121, December 2012. doi: 10.1016/j.enconman.2012.04.014. URL https://doi.org/10.1016/j.enconman.2012.04.014.

[32] T. Huria, M. Ceraolo, J. Gazzarri, and R. Jackey. High fidelity electrical model with thermal dependence for characterization and simulation of high power lithium battery cells. In *2012 IEEE International Electric Vehicle Conference*. IEEE, March 2012. doi: 10.1109/ievc.2012.6183271. URL http://dx.doi.org/10.1109/IEVC.2012.6183271.

[33] A.A. Hussein and I. Batarseh. An overview of generic battery models. In *2011 IEEE Power and Energy Society General Meeting*. IEEE, July 2011. doi: 10.1109/pes.2011.6039674. URL https://doi.org/10.1109/pes.2011.6039674.

[34] Law Insider. Liquid Electrolyte Definition | Law Insider — lawinsider.com. https://www.lawinsider.com/dictionary/liquid-electrolyte, 2020. [Accessed 19-09-2023].

[35] R. Jackey, M. Saginaw, P. Sanghvi, J. Gazzarri, T. Huria, and M. Ceraolo. Battery model parameter estimation using a layered technique: An example using a lithium iron phosphate cell. In *SAE Technical Paper Series*, ANNUAL. SAE International, April 2013. doi: 10.4271/2013-01-1547. URL http://dx.doi.org/10.4271/2013-01-1547.

[36] K. Jalkanen, T. Aho, and K. Vuorilehto. Entropy change effects on the thermal behavior of a lifepo 4 /graphite lithium-ion cell at different states of charge. *Journal of Power Sources*, 243:354360, December 2013. ISSN 0378-7753. doi: 10.1016/j.jpowsour.2013.05.199. URL http://dx.doi.org/10.1016/j.jpowsour.2013.05.199.

[37] W. Junping, C. Quanshi, and C. Binggang. Support vector machine based battery model for electric vehicles. *Energy Conversion and Management*, 47(7-8):858–864, May 2006. doi: 10.1016/j.enconman.2005.06.013. URL https://doi.org/10.1016/j.enconman.2005.06.013.

[38] P. Keil, S.F. Schuster, J. Wilhelm, J. Travi, A. Hauser, R.C. Karl, and A. Jossen. Calendar aging of lithium-ion batteries: I. impact of the graphite anode on capacity fade. *Journal of The Electrochemical Society*, 163 (9):A1872A1880, 2016. ISSN 1945-7111. doi: 10.1149/2.0411609jes. URL http://dx.doi.org/10.1149/2.0411609jes.

[39] P. Kollmeyer. Panasonic 18650pf li-ion battery data, 2018. URL https://data.mendeley.com/datasets/wykht8y7tg/1.

[40] P. Kollmeyer, A. Hackl, and A. Emadi. Li-ion battery model performance for automotive drive cycles with current pulse and eis parameterization. In *2017 IEEE Transportation Electrification Conference and Expo (ITEC)*. IEEE, June 2017. doi: 10.1109/itec.2017.7993319. URL http://dx.doi.org/10.1109/ITEC.2017.7993319.

[41] A. König, L. Nicoletti, D. Schröder, S. Wolff, A. Waclaw, and M. Lienkamp. An overview of parameter and cost for battery electric vehicles. *World Electric Vehicle Journal*, 12(1):21, February 2021. ISSN 2032-6653. doi: 10.3390/wevj12010021. URL http://dx.doi.org/10.3390/wevj12010021.

[42] H. Kühnelt, F. Mastropierro, N. Zhang, S. Toghyani, and U. Krewer. Are batteries fit for hybrid-electric regional aircraft? *Journal of Physics: Conference Series*, 2526(1):012026, June 2023. doi: 10.1088/1742-6596/2526/1/012026. URL https://doi.org/10.1088/1742-6596/2526/1/012026.

[43] M.T. Lawder, B. Suthar, P.W.C. Northrop, S. De, C.M. Hoff, O. Leitermann, M.L. Crow, S. Santhanagopalan, and V.R. Subramanian. Battery energy storage system (BESS) and battery management system (BMS) for grid-scale applications. *Proceedings of the IEEE*, 102(6):1014–1030, June 2014. doi: 10.1109/jproc.2014.2317451. URL https://doi.org/10.1109/jproc.2014.2317451.

[44] Litech. SAMSUNG INR18650-33G 3150mAh 9.75A Li-ion Battery Cell - LiTech Power Co.,Ltd — litechpower.com. https://www.litechpower.com/product-detail/batterycellSAMSUNG-INR18650-33G_3150mAh.html, 2023. [Accessed 16-04-2024].

[45] Z. Liu, W. Huang, K. Wang, J. Xie, and H. He. Selfdischarge voltage drop estimation method based on improved gaussian process regression. *Energy Technology*, 10, 06 2022. doi: 10.1002/ente.202200402.

[46] A. Loges, S. Herberger, P. Seegert, and T. Wetzel. A study on specific heat capacities of li-ion cell components and their influence on thermal management. *Journal of Power Sources*, 336:341350, December 2016. ISSN 0378-7753. doi: 10.1016/j.jpowsour.2016.10.049. URL http://dx.doi.org/10.1016/j.jpowsour.2016.10.049.

[47] Lygte. Test of Samsung INR18650-33G 3150mAh (Blue) — lygte-info.dk. https://lygte-info.dk/review/batteries2012/Samsung%20INR18650-33G%203150mAh%20(Blue)%20UK.html, 2021. [Accessed 06-01-2024].

[48] S. Ma, M. Jiang, P. Tao, C. Song, J. Wu, J. Wang, T. Deng, and W. Shang. Temperature effect and thermal impact in lithium-ion batteries: A review. *Progress in Natural Science: Materials International*, 28(6): 653666, December 2018. ISSN 1002-0071. doi: 10.1016/j.pnsc.2018.11.002. URL http://dx.doi.org/10.1016/j.pnsc.2018.11.002.

[49] Mathworks. Rigid conduit for fluid flow in thermal liquid systems - MATLAB - MathWorks Benelux — nl.mathworks.com. https://nl.mathworks.com/help/simscape/ref/pipetl.html, 2013. [Accessed 11-04-2024].

[50] MathWorks. Closed conduit that transports fluid between thermal liquid components - MATLAB - MathWorks Benelux — nl.mathworks.com. https://nl.mathworks.com/help/hydro/ref/pipetl.html, 2022. [Accessed 25-04-2024].

[51] MathWorks. Parameter Estimation — nl.mathworks.com. https://nl.mathworks.com/discovery/parameter-estimation.html, 2022. [Accessed 03-06-2024].

[52] Mathworks. Solve nonlinear least-squares (nonlinear data-fitting) problems - MATLAB lsqnonlin - MathWorks Benelux — nl.mathworks.com. https://nl.mathworks.com/help/optim/ug/lsqnonlin.html, 2024. [Accessed 15-04-2024].

[53] Mathworks. How the Software Formulates Parameter Estimation as an Optimization Problem - MATLAB & Simulink - MathWorks Benelux — nl.mathworks.com. https://nl.mathworks.com/help/sldo/ug/optimization-problem-formulation-for-parameter-estimation.html, 2024. [Accessed 15-04-2024].

[54] A. Mauger and C. M. Julien. Critical review on lithium-ion batteries: are they safe? sustainable? *Ionics*, 23(8):1933–1947, June 2017. doi: 10.1007/s11581-017-2177-8. URL https://doi.org/10.1007/s11581-017-2177-8.

[55] M.V. Morganti, S. Longo, M. Tirovic, C. Blaise, and G. Forostovsky. Multi-scale, electro-thermal model of nmc battery cell. *IEEE Transactions on Vehicular Technology*, 68(11):1059410606, November 2019. ISSN 1939-9359. doi: 10.1109/tvt.2019.2943052. URL http://dx.doi.org/10.1109/TVT.2019.2943052.

[56] M. Nagelsmit. Pipistrel Velis Electro - Royal Netherlands Aerospace Centre — nlr.nl. https://www.nlr.nl/aandachtsgebieden/strategische-themas-2022-2025/thema-duurzame-luchtvaart/pipistrel/, 2018. [Accessed 28-03-2024].

[57] A. Najafi and M. Masih-Tehrani. Hybrid adaptive battery parameter estimation approach for equivalent circuit model toolbox. *SoftwareX*, 24:101534, December 2023. ISSN 2352-7110. doi: 10.1016/j.softx.2023.101534. URL http://dx.doi.org/10.1016/j.softx.2023.101534.

[58] N. Nielsen. What is "capacitive effect" in terms of battery research? — physics.stackexchange.com. https://physics.stackexchange.com/questions/781909/what-is-capacitive-effect-in-terms-of-battery-research, 2023. [Accessed 02-01-2024].

[59] Nigel. Specific Heat Capacity of Lithium Ion Cells - Battery Design — batterydesign.net. https://www.batterydesign.net/specific-heat-capacity-of-lithium-ion-cells/#:~:text=For%20the%20main%20lithium%20ion,)%20%3D%201040%20J%2Fkg., 2022. [Accessed 16-02-2024].

[60] D. Novak. Design of li-ion battery pack emulator. September 2015. https://www.google.com/url?sa=t&rct=j&q=&esrc=s&source=web&cd=&ved=2ahUKEwiBrMOH58-BAxXXM-wKHZg-KvcQFnoECBIQAQ&url=https

[61] P.U. Nzereogu, A.D. Omah, F.I. Ezema, E.I. Iwuoha, and A.C. Nwanya. Anode materials for lithium-ion batteries: A review. *Applied Surface Science Advances*, 9:100233, June 2022. doi: 10.1016/j.apsadv.2022.100233. URL https://doi.org/10.1016/j.apsadv.2022.100233.

[62] Panasonic. actec.dk. https://actec.dk/media/documents/70FC46554038.pdf, 2016. [Accessed 06-01-2024].

[63] Pipistrel. Velis Electro - Pipistrel — pipistrel-aircraft.com. https://www.pipistrel-aircraft.com/products/velis-electro/, 2024. [Accessed 02-04-2024].

[64] R.I. Pushparaj, A.R. Kumar, and G. Xu. Enhancing safety in lithium-ion batteries with additive-based liquid electrolytes: A critical review. *Journal of Energy Storage*, 72:108493, November 2023. ISSN 2352-152X. doi: 10.1016/j.est.2023.108493. URL http://dx.doi.org/10.1016/j.est.2023.108493.

[65] R. Rao, S. Vrudhula, and D.N. Rakhmatov. Battery modeling for energy-aware system design. *Computer*, 36(12):77–87, December 2003. doi: 10.1109/mc.2003.1250886. URL https://doi.org/10.1109/mc.2003.1250886.

[66] E. Redondo-Iglesias, P. Venet, and S. Pelissier. Calendar and cycling ageing combination of batteries in electric vehicles. *Microelectronics Reliability*, 8890:12121215, September 2018. ISSN 0026-2714. doi: 10.1016/j.microrel.2018.06.113. URL http://dx.doi.org/10.1016/j.microrel.2018.06.113.

[67] F. Russo. Eviation alice analysis of aircraft performance and comparison with official claims. https://www.linkedin.com/posts/fabio-russo-51375a33_eviation-alice-performances-analysis-activity-6939894154856431616-wKZ2, 2023. Accessed: 02-05-2024.

[68] Pipistrel Vertical Solutions. *Pilot's Operating Handbook Velis Electro*. Pipistrel Vertical Solutions, Vipavask Cesta 2 Adjovscina, Slovenia, 2nd edition, February 2022.

[69] R.R. Thakkar. Electrical equivalent circuit models of lithium-ion battery. In *Management and Applications of Energy Storage Devices*. IntechOpen, March 2022. doi: 10.5772/intechopen.99851. URL https://doi.org/10.5772/intechopen.99851.

[70] T. Tiele. A Guide to Electrical Wire Sizes — thespruce.com. https://www.thespruce.com/electrical-wire-sizes-1152851, 2022. [Accessed 08-01-2024].

[71] M.K. Tran, A. DaCosta, A. Mevawalla, S. Panchal, and M. Fowler. Comparative study of equivalent circuit models performance in four common lithium-ion batteries: LFP, NMC, LMO, NCA. *Batteries*, 7(3):51, July 2021. doi: 10.3390/batteries7030051. URL https://doi.org/10.3390/batteries7030051.

[72] Michigan State Unviersity. RC Circuits — web.pa.msu.edu. https://web.pa.msu.edu/courses/1997spring/phy232/lectures/kirchoff/rc.html#:~:text=The%20voltage%20across%20the%20capacitor,contiuously%20flow%20through%20a%20capacitor., 2012. [Accessed 03-04-2024].

[73] R. Wang, W. Cui, F. Chu, and F. Wu. Lithium metal anodes: Present and future. *Journal of Energy Chemistry*, 48:145–159, sep 2020. doi: 10.1016/j.jechem.2019.12.024. URL https://doi.org/10.1016%2Fj.jechem.2019.12.024.

[74] S. Wang. Entropy and heat generation of lithium cells/batteries. *Chinese Physics B*, 25(1):010509, January 2016. ISSN 1674-1056. doi: 10.1088/1674-1056/25/1/010509. URL http://dx.doi.org/10.1088/1674-1056/25/1/010509.

[75] S. Wang. *Battery System Modelling*. Elsevier, 2021. ISBN 9780323904728. doi: 10.1016/c2020-0-03232-9. URL http://dx.doi.org/10.1016/C2020-0-03232-9.

[76] Wikipedia. Eviation Alice - Wikipedia — en.wikipedia.org. https://en.wikipedia.org/wiki/Eviation_Alice#cite_note-AvWeek26feb2018-6, 2022. [Accessed 03-10-2023].

[77] Wikipedia. Self-discharge - Wikipedia — en.wikipedia.org. https://en.wikipedia.org/wiki/Self-discharge, 2022. [Accessed 05-01-2024].

[78] Wikipedia. Electrical resistivity and conductivity - Wikipedia — en.wikipedia.org. https://en.wikipedia.org/wiki/Electrical_resistivity_and_conductivity, 2023. [Accessed 08-01-2024].

[79] Wikipedia. Lithium iron phosphate battery - Wikipedia — en.wikipedia.org. https://en.wikipedia.org/wiki/Lithium_iron_phosphate_battery, 2023. [Accessed 03-10-2023].

[80] Wikipedia. Lumped-element model - Wikipedia — en.wikipedia.org. https://en.wikipedia.org/wiki/Lumped-element_model, 2023. [Accessed 16-02-2024].

[81] Wikipedia. Thermal conductance and resistance - Wikipedia — en.wikipedia.org. https://en.wikipedia.org/wiki/Thermal_conductance_and_resistance, 2024. [Accessed 08-04-2024].

[82] T. Tanaka Y. Inui, S. Hirayama. Detailed estimation method of heat generation during charge/discharge in lithiumion battery using equivalent circuit. *Electronics and Communications in Japan*, 102(12):314, December 2019. ISSN 1942-9541. doi: 10.1002/ecj.12221. URL http://dx.doi.org/10.1002/ecj.12221.

[83] Z. Yang, Q. Huang, S. Li, and J. Mao. High-temperature effect on electrochemical performance of li4ti5o12 based anode material for li-ion batteries. *Journal of Alloys and Compounds*, 753:192202, July 2018. ISSN 0925-8388. doi: 10.1016/j.jallcom.2018.04.105. URL http://dx.doi.org/10.1016/j.jallcom.2018.04.105.

[84] T. Yin, L. Jia, X. Li, L. Zheng, and Z. Dai. Effect of high-rate cycle aging and over-discharge on ncm811 (lini0.8co0.1mn0.1o2) batteries. *Energies*, 15(8):2862, April 2022. ISSN 1996-1073. doi: 10.3390/en15082862. URL http://dx.doi.org/10.3390/en15082862.

[85] A. Yoshino. *Development of the Lithium-Ion Battery and Recent Technological Trends*, page 120. Elsevier, 2014. doi: 10.1016/b978-0-444-59513-3.00001-7. URL http://dx.doi.org/10.1016/B978-0-444-59513-3.00001-7.

[86] D.G. Cahill Z. Cheng, X. Ji. Battery absorbs heat during charging uncovered by ultra-sensitive thermometry. *Journal of Power Sources*, 518:230762, January 2022. ISSN 0378-7753. doi: 10.1016/j.jpowsour.2021.230762. URL http://dx.doi.org/10.1016/j.jpowsour.2021.230762.

[87] C. Zhang, K. Li, S. Mcloone, and Z. Yang. Battery modelling methods for electric vehicles - a review. In *2014 European Control Conference (ECC)*. IEEE, June 2014. doi: 10.1109/ecc.2014.6862541. URL https://doi.org/10.1109/ecc.2014.6862541.

[88] K. Zhang, K. Yu, Y. Liu, and Y. Zhao. Effect of surface oxidation on emissivity properties of pure aluminum in the near infrared region. *Materials Research Express*, 4:086501, 08 2017. doi: 10.1088/2053-1591/aa7fc9.

[89] R. Zhang, B. Xia, B. Li, L. Cao, Y. Lai, W. Zheng, H. Wang, W. Wang, and M. Wang. A study on the open circuit voltage and state of charge characterization of high capacity lithium-ion battery under different temperature. *Energies*, 11(9):2408, September 2018. ISSN 1996-1073. doi: 10.3390/en11092408. URL http://dx.doi.org/10.3390/en11092408.

[90] Q. Zhao, S. Stalin, C. Zhao, and L.A. Archer. Designing solid-state electrolytes for safe, energy-dense batteries. *Nature Reviews Materials*, 5(3):229–252, February 2020. doi: 10.1038/s41578-019-0165-5. URL https://doi.org/10.1038/s41578-019-0165-5.

[91] J. Zhu, H. Zhang, G. Wu, S. Zhu, and W. Liu. Thermal performance of cylindrical battery module with both axial and radial thermal paths: Numerical simulation and thermal resistance network analysis. *Journal of Energy Storage*, 49:104197, May 2022. ISSN 2352-152X. doi: 10.1016/j.est.2022.104197. URL http://dx.doi.org/10.1016/j.est.2022.104197.

[92] J. Zhu, H. Zhang, G. Wu, S. Zhu, and W. Liu. Thermal performance of cylindrical battery module with both axial and radial thermal paths: Numerical simulation and thermal resistance network analysis. *Journal of Energy Storage*, 49:104197, May 2022. ISSN 2352-152X. doi: 10.1016/j.est.2022.104197. URL http://dx.doi.org/10.1016/j.est.2022.104197.

[93] Zitara. What is Hysteresis in Batteries? | Zitara Glossary — zitara.com. https://www.zitara.com/glossary/terms/hysteresis#:~:text=Hysteresis%20is%20a%20phenomenon%20where,discharging%20to%20the%20same%20SoC., 2024. [Accessed 04-04-2024].